Electron transport through low-dimensional carbon-based systems

Von der Fakultät für Mathematik und Physik
der Gottfried Wilhelm Leibniz Universität Hannover
zur Erlangung des Grades

Doktor der Naturwissenschaften
Dr. rer. nat.

genehmigte Dissertation

von

M. Sc. Diana Slawig

2021

Referent: Prof. Dr. Herbert Pfnür (Leibniz Universität Hannover, Germany)
Korreferent: Prof. Dr. Christoph Tegenkamp (Technische Universität Chemnitz, Germany)
Korreferent: Prof. Dr. Franz Renz (Leibniz Universität Hannover, Germany)

Tag der Promotion: 01. 09. 2021

Abstract

Carbon-based materials in all their facets yield an extremely large area of electronic applications. Its quasi-unlimited availability, wide ranging tuneability and scalability make them a potent rival to the currently dominant silicon technology providing the possibility to overcome its limitations. This thesis addresses fundamental understanding of electronic transport processes in three selected systems. Graphene is well know for its exceptional electronic character and chemical stability. Here an approach on utilizing graphene as a sensor to molecular specimen of high sensitivity is presented. By adsorbing atomic hydrogen, the inert character of graphene is broken and even smallest amounts of hydrogenation is found to increase the resistance by orders of magnitude. The framework of Anderson localization describes the electron transport in hydrogenated graphene, showing a clear correlation between the localization lengths, the mean free path and the coverage. Upon hydrogenation the band transport of graphene is substituted by variable range hopping. Activation energies for this activated transport were found to range from $26\,\text{meV}$ to $48\,\text{meV}$. Those values do not refer to the band gap observed in hydrogenated graphene around the Dirac point and exclude an ordinary band insulator. Furthermore, PbPc molecules were adsorbed to pristine and hydrogenated graphene. While the molecules show no influence on the electronic properties of pristine samples, they significantly interact with the chemisorbed H atoms. Density functional theory shows a barrier-less reaction between the H atoms and the PbPc molecules with an energy gain up to $2.8\,\text{eV}$. This annihilation process is very efficient and restores the transport properties of pristine graphene.

Contrary to the two-dimensional graphene carbon can also be arranged in one-dimensional fibers and tubes. Extended compound materials of these fibers are heavily discussed in energy storage technology. The electronic transport properties are investigated by means of four-point probe microscopy. A major influence on the conductivity of this materials is the degree of ordering inside the structures. Pristine and templated carbon nanofibers were analyzed and a strong relation of their internal structure and the resistance is found. Improved crystal quality lowers the resistivity of the single fibers as well as pf the compound material. The compounds were investigated by probe distances in the range of the building blocks as well as at significantly larger scales. The latter allows the system to be treated as two-dimensional and isotropic. The measurements combined with simulations yield a description of the conduction tensor as a combination of band conduction inside the microscopic building blocks and hopping conduction across the fibers.

As an ultimate miniaturization of conductive carbon materials, spin selective chiral molecules are heavily investigated. Here measurements of single polyalanine molecules by means of mechanically controllable breakjunctions are presented. Transport dominated by tunneling mechanisms has been found by investigating molecules of different length. For lengths between $2.6\,\text{nm}$ and $5.4\,\text{nm}$, conductance values ranging from $0.007\,\text{G}_0$ to $0.01\,\text{G}_0$ were determined, with a reduction factor of $\beta = 3.5\,\text{nm}^{-1}$. Symmetric IV characteristics indicate a interdigitation process of the molecules in between the gold contacts. A ratcheting model is proposed to explain the transport properties in regard to the geometrical configuration of the molecules.

Keywords: electronic transport, sensors, carbon-based materials, graphene, biomolecules

Acronyms

0D	zero-dimensional
1D	one-dimensional
2D	two-dimensional
3D	three-dimensional
2pp	two-point probe
4pp	four-point probe
ARPES	angle-resolved photoemission spectroscopy
Au	gold
CISS	chiral induced spin selectivity
CNF	carbon nanofiber
CNT	carbon nanotube
Cr	chromium
CVD	chemical vapour deposition
DFT	density functional theory
EBL	electron beam lithography
HOMO	highest occupied molecular orbital
HOPG	highly oriented pyrolytic graphite
LED	light emitting diode
LUMO	lowest unoccupied molecular orbital
MCBJ	mechanically controllable break junction
MIT	metal-insulator transition
MLG	monolayer graphene
MMA	methylmethaacrylate
PA	polyalanine
PAN	polyacrylonitrile
PbPc	lead phtalocyanine
PMMA	polymethylmethaacrylate
QFMLG	quasi-freestanding monolayer graphene
RIE	reactive ion etching
SAM	self assembled monolayer
SEM	scanning electron microscope
SiC	silicon carbide
SOC	spin orbit coupling

SPALEED	spot profile analysis low energy electron diffraction
STM	scanning tunnelling microscope
STS	scanning tunnelling spectroscopy
TEM	transmission electron microscopy
UHV	ultra-high vacuum
VRH	variable range hopping
XPS	x-ray photoelectron spectroscopy

Contents

Part I

Introduction and Physical Background

Chapter **1**

Introduction

In modern times, electronics have become an essential part of most things around us, e.g. cars, phones or watches. This is only possible because of silicon-based integrated circuits, which have large impact on the society in the last decades [1]. The demand for larger computation capacity, cheaper electronic memory and faster, more powerful processors is still growing. It drives the miniaturization of single electronic components which are today hitting the physical limits.

The immense knowledge made it the fundamental material in integrated electronics for more than six decades. Mostly because of the astonishing control over the processing of the material, like e.g. doping, which determine the material properties. With the upcoming $2\,nm$ technology, as announced by IBM [2], established for transistor devices, the scaling possibility for silicon-based devices reaches a breaking point. It is the limit of miniaturization of silicon-based electronics as already predicted at the end of the last century [3–5]. As technology gets more and more complex and expensive, it drives the search for alternative materials and concepts which offer further scaling opportunities.

Three main paths open up to overcome the limitations of silicon-based electronics: more efficient architecture and packaging, new models of computation, and new material and device concepts [6]. In the scope of this thesis, the third path is investigated focusing on carbon as promising candidate for future electronics. Carbon materials show an incredible diversity in terms of dimensionality and structure, including diamond, graphite, graphene, buckyballs, amorphous carbons, nanotubes and -fibers [7–9]. This variety can be extended even further by adding hydrogen, which leads to a wide range of organics. The huge diversity sparks off a huge variance of electronic properties, some of them even being unique [10–13]. Nanomaterials carry properties like a large surface area, high flexibility and usually good electronic conductivity compared to bulk materials [14–17]. This puts nanostructures like tube, rods, sheets and fibers into the focus of research. By combining these advantages, carbon nanomaterials have shown to be promising candidates for advanced electronic applications like batteries, transistors, ligh emitting diodes (LEDs), sensors and solar cells [18–24].

In any case, fundamental understanding of the materials properties is crucial for the possi-

ble development of new concepts, improving miniaturization, heat dissipation and operating speed. For example, the field of sensor development aims for miniaturized devices while maximizing the sensitivity, which is often limited by reaction barriers or grain boundaries in mircoscopic solid-state devices. The signal in these sensors usually originates from oxidizing or reducing adsorbed gases and the concomitant change of carrier concentration. A promising candidate for this application is graphene, a two-dimensional (2D) sheet of carbon. It shows extraordinary electronic properties, including outstandingly high conductance values and mobilities around $10^5 \, \mathrm{cm^2 \, V^{-1} \, s^{-1}}$ at room temperature [13, 25, 26], resulting in an extremely low noise material and qualifying it for highly sensitive sensor applications. It was shown, that even the attachment or detachment of a single gas molecule changes the carrier concentration, inducing a step-like change of conductance [27]. This leads to the ultimate sensitivity of graphene-based sensors, which are able to detect individual gas molecules. Despite this promising prospects, the inert character of graphene requires functionalization in order to exploit a broad range of applications [28, 29]. One aim of the first experimental part of thesis is to analyze the functionalization of graphene by hydrogen adsorption and the interaction between this surface and physisorbed molecules.

Besides the interesting applications of graphene at nanoscale, it also offers novel opportunities for macroscopic usage [30, 31]. Graphene reveals a conductivity of up to $100 \, \mathrm{MS \, m^{-1}}$ [13, 25, 26] compared to approx. $60 \, \mathrm{MS \, m^{-1}}$ [32] in copper, which is todays number one conductor track material. Furthermore, it outperforms copper in terms of thermal conductivity, density and abundance on earth [31, 33, 34]. To fabricate macroscopic graphene-based materials, usually compounds filtered from a graphene powder dispersion are used [35]. This leads to lower conductivity compared to single graphene layers but can still reach up to $80 \, \mathrm{MS \, m^{-1}}$ with optimized production parameters, like doping and graphene flake size [36, 37]. This indicates the possibiliy of enormous efficiency improvements. Additionally a switch from copper to carbon could allow a massive reduction of weight and volume. To be able to fully exploit all the possible advantages, the detailed understanding of the interplay between the mesoscopic properties of the individual building blocks and the transport behavior of the macroscopic material is essentially. One approach for a complete description of the conductivity is presented in this thesis.

Another form of carbon-based conductors are carbon nanofibers (CNFs), whose application diversity ranges from lightweight construction purposes and composite reinforcements, sensor applications and electrochemical capacitors to opto- and nanoelectronics [38–40]. The reasons for this wide range are high stiffness and tensile strength combined with a large chemical resistance and low thermal expansion. Their high electrical conductivity and high surface to volume ratio qualifies them for both mechanical and electronic applications. External conditions like stress, strain or gaseous environments can distinctly influence the conductance of CNFs, especially qualifying them as candidates for sensor applications as well [40]. Again, a high electric conductivity is the key parameter for optimizing the components for these applications. One method to tune the electronic properties, is the use of other carbon-based nanostructures for optimization of the graphitic structure of the material [41–43]. In this thesis, the correlation between the structural properties and the electronic transport of pristine and carbon nanotube (CNT)-templated CNFs was investigated with the aim to maximize the conductivity.

Towards ultimate miniaturization, the path leads to molecules as buildings blocks. Especially

DNA and the group of chiral molecules gained a lot of interest within the last years due to their spinfiltering properties [44–46]. This so-called chiral induced spin selectivity (CISS) effect allows the construction of extremely small electronic components overcoming the limitations of magnetic-based memory technologies and paves the way for the production of inexpensive, high density memory devices [47–50]. The electron transport through single chiral molecules is examined in this thesis, highlighting its geometric configuration as an important factor.

The realization of all these future applications is linked to a deep understanding of the physical background behind the conductance in low dimensions. Fundamental research is needed to smooth the path into the next generation of electronic devices, superseding the dominance of silicon technology.

Structure of this thesis

Part I of this thesis continues, after this introduction, with an overview over the fundamental physical concepts in Chpt. 2, including the general concepts of low-dimensional transport and a comparison between diffusive and ballistic transport. The determination of the resistivity of a material is highlighted with regard to confinement, anisotropy and inhomogenities. Localization effects, which start to play a role in low-dimensional disordered systems, are explained before section is concluded by an overview of electron transport through molecules.

Part II presents and discusses the experimental methods and results of this work. Starting with a description of the used measurement setups and techniques in Chpt. 3. These are namely the four-point probe scanning tunneling microscope and mechanically controllable breakjunctions.

Analysis of adsorption processes of atomic and molecular species to graphene is investigated in Chpt. 4. Hydrogen adsorption to graphene is investigated, before combining this functionalized surface with PbPc molecules.

Chpt. 5 focuses on the electronic transport through low-dimensional carbon-based compound materials. The effect of templating with low-dimensional carbons to the conductivity properties of CNF is analyzed followed by mixed experimental and simulation approaches for determining the complete conductivity tensor of a compound material.

The last experimental chapter, Chpt. 6. deals with electron transport through single chiral molecules, analyzing the dominant transport mechanism and presenting a model to include geometrical configurations.

Part III summarizes and concludes the findings of the former chapters and gives an outlook to possible further investigations.

<div style="text-align: right;">

Chapter 2

</div>

Electrical transport in low dimensions

This chapter describes the basic concepts in physics this thesis is based on. In the first part, Sec. 2.1, the general concepts of electron transport in low dimensions are explained, including the definition of length scales, transport regimes and a description of diffusive and ballistic transport. Sec. 2.2 describes the determination of the resistivity for different materials, confined, anisotropic and inhomogenious systems. Sec. 2.3 introduces the concept of Anderson localization in various dimensions and the variable range hopping transport mechanism. Lastly, electronic transport through molecules is outlined in Sec. 2.4.

2.1 General concepts of low-dimensional transport

2.1.1 Characteristic length scales

The electrical transport in low dimensions is characterized by different distinctive length parameters that give information about which physical effects predominate. One of the most fundamental parameters to determine the transport regime is the electronic mean free path λ_e. It describes the distance an electron can move in between two scattering events. These scattering processes can be either elastic or inelastic, depending on whether energy is transferred or not. Elastic scattering, e.g., on impurities, causes a change of momentum of the charge carrier, while inelastic scattering, e.g, electron-electron scattering, changes both momentum and energy. Although there are two different mean free paths for elastic λ_{el} and inelastic λ_{in} scattering, they are usually combined.

The phase coherence length λ_Φ gives the distance for which the quantum coherence is preserved. This quantity is relevant, because elastic as well as inelastic, events can induce a randomization of the phase. Another fundamental value in any metallic system is the Fermi wavelength $\lambda_F = 2\pi/k_F$ which is associated with the Fermi wavenumber k_F.

There are three main transport regimes: diffusive, semi-ballistic and ballistic transport.

For example in graphene, the Fermi wavelength is determined by the electron density n by $\lambda_F = 2\sqrt{\pi/n}$. For the example of epitaxial monolayer graphene on SiC substrates
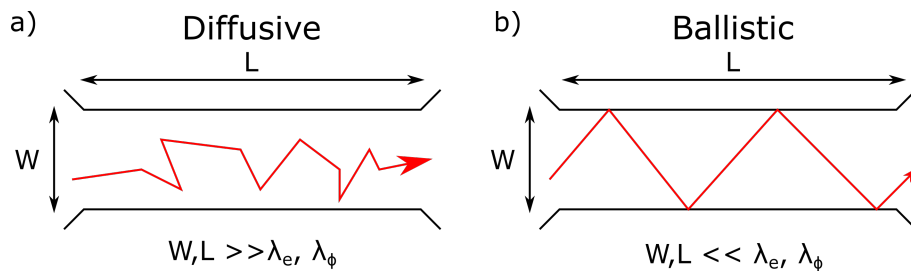
Figure 2.1: Schematic illustrations of the diffusive (a) and ballistic (b) transport regimes. The electron trajectories are marked in red.

(n $= 1.2 \times 10^{13}\,\mathrm{cm}^{-2}$), the Fermi wavelength is in the range of $10\,\mathrm{nm}$. Based on those values, two main electron transport regimes can be defined.

As a model for a nanoelectronic material, a conductor with the length L and width W in between to ideal contacts is assumed. In this setup the physical dimensions limit the current flow through the system due to the finite characteristic lengths λ_e and λ_Φ. For a macroscopic conductor, the dimensions are significantly larger than the mean free path and the phase coherence length, $W, L \gg \lambda_e, \lambda_\Phi$. A large number of scattering events occur in between the contacts as schematically pictured in Fig. 2.1 a). This transport regime is called diffusive and can be described by the Drude-Sommerfeld model as explained in Sec. 2.1.2.

If the mean free path and the coherence length are large compared to the physical dimensions, $W, L \ll \lambda_e, \lambda_\Phi$, the ballistic transport regime is entered. The only scattering events that occur, are reflections from the physical boundaries of the conductor, as schematically depicted in Fig. 2.1 b). This transport regime can be explained by the Landauer formalism as shown in Sec. 2.1.3, There are two ways to reach the ballistic regime, either by increasing the mean free path or by extreme narrowing of the conductors.

2.1.2 Diffusive transport

A voltage gradient in between two electrodes leads to an electric field E which acts as a driving force for electrons within the electronic system. The relation in between the current density J and the electric field E is described by Ohm´s law

$$J = \sigma E \tag{2.1.1}$$

where σ is the material-specific electrical conductivity.

Already in 1900, P. Drude proposed a model to describe diffusive electron transport based on kinetic gas theory [51]. This model was later extended and corrected by A. Sommerfeld [52] who described the electrons as a fermionic gas.

To determine the conductivity within this framework, the current density can be expressed as a function of the average electron velocity $<\mathrm{v}> = \hbar \mathrm{k}/\mathrm{m_e}$, where m_e is the electron mass and k its momentum. The current density is given by the electron density n, the electron charge e and the average velocity $<v>$:

$$J = en <v> = \frac{en\hbar}{m_e} <k> . \tag{2.1.2}$$

The average momentum distribution $<k>$ vanishes for thermal equilibrium, $<k>_0 = 0$ and no current flows. To obtain a finite current flow, the electron momentum distribution needs to deviate from equilibrium. For this case the current density can be written as:

$$J = \frac{en\hbar}{m_e}[<k> - <k>_0] = \frac{en\hbar}{m_e}\delta k. \tag{2.1.3}$$

External forces like electric fields and scattering events change the momentum distribution. If only steady-state conditions ($\frac{d<k>}{dt} = 0$) are considered the expression for the momentum distribution can be written as

$$\delta k = \frac{e\tau}{\hbar}, \tag{2.1.4}$$

where τ describes the average time in between to scattering events. To determine the conductivity σ, Ohms law can now be used

$$J = \frac{ne^2\tau}{m_e}E = ne\mu E = \sigma E. \tag{2.1.5}$$

In this case, μ describes the electron mobility. This leads to the definition of the conductivity

$$\sigma = \frac{ne^2\tau}{m_e} = \frac{ne^2\lambda_e}{m_e v_F}. \tag{2.1.6}$$

The mean free path λ_e as defined in Sec. 2.1.1 is used for this definition.
Within this transport model, the Fermi velocity $v_F = \hbar k_F/m_e$ is used rather than the average drift velocity v_D. This is due to the fact, that only electrons with energies in a small range of $k_B T$, where k_B is the Boltzmann factor and T the temperature, around the Fermi energy E_F partake in transport.
Under equilibrium conditions, all states within the Fermi sphere with the radius k_F are occupied. External electric fields cause a shift of δk, as schematically depicted in Fig. 2.2 a). Only the states close to $(\pm k_F + \delta k)$ can be redistributed whereas the states deeper inside the Fermi sphere stay occupied as long as shifts δk remain small compared to k_F.
For moderate field intensities this shift δk is vanishingly small compared to k_F, which means only a very small amount of the present electrons contribute to electronic transport. The shift in the momentum distribution can be visualized by the definition of quasi Fermi levels, as depicted in Fig. 2.2. For electrons moving in the direction of the external electric field, and the accompanying force eE, a quasi Fermi level of F^+ is defined and another quasi Fermi level F^- for electrons moving in the opposite direction. All states below F^- are filled and carry no current. In the energy range between the two quasi Fermi energies F^+ and F^- states with $-k_F$ are empty while the states with k_F are full. The electrons in these states are the ones carrying the current [54].

2.1.3 Ballistic transport

If the mean free path of the electrons is larger than the physical dimensions of the conductor, the ballistic transport regime is entered. Again, a conductor between to ideal contacts. Ideal contact here mean that no electrons are reflected while entering or leaving the reservoirs, is used as a model for the following considerations. The model is depicted in Fig. 2.3 a).
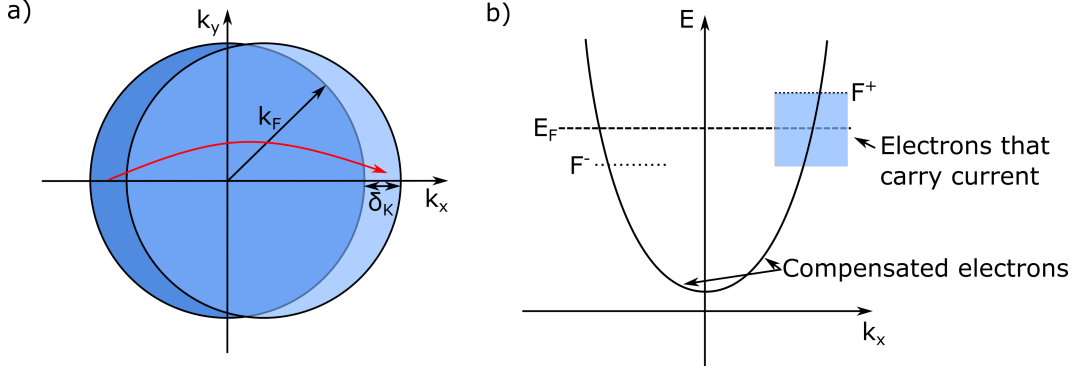
Figure 2.2: a) Fermi spheres in equilibrium and the effect of an electric field. The equilibrium distribution is shifted by δk. The redistribution of states is indicated by the red arrow. Adapted from [53]. b) Dispersion relation E(k) with quasi Fermi levels arising from the external electric field. Electrons that contribute to the current are marked in blue. Adapted from [54].

Due to the reduced dimensions of the conductor $W, L \ll \lambda_e$ the dispersion relation only consists of a few modes. An applied bias voltage causes a splitting of the quasi Fermi levels $\mu^l - \mu^r > 0$, as schematically shown in Fig. 2.3 b). In consequence, the $+k$ $(-k)$ states are only populated from electrons origination from the left (right) electrode respectively. An electron coming from the left contact populates a $+k$ state in the conductor and exits into the right contact without reflection. The same is true for an electron originating from the right contact for a $-k$ state.

The quasi Fermi levels for $+k$ and $-k$ states inside the contacts are almost equal due to the high subband density. In the conductor where only few subbands are present. An external voltage results in a splitting of the quasi Fermi levels. This system now features $-k$ $(+k)$ quasi Fermi level that are equal to the Fermi levels of the adjacent contacts. This effect is shown in Fig. 2.3 c).

Based on this consideration, the current through a one dimensional conductor is given by the summation of the currents carried by the right and left moving state

$$I = I^l - I^r = -\frac{e}{L} \sum_l \frac{\hbar(k^- - k^+)}{m_e}. \tag{2.1.7}$$

By converting the sum into an integral

$$\sum_k \rightarrow 2\frac{L}{2\pi} \int dk, \tag{2.1.8}$$

the current is given by

$$I = \frac{2e}{h} \int_0^\infty (f_+(E) - f_-(E))M(E)dE = \frac{2e}{h}M(\mu^l - \mu^r). \tag{2.1.9}$$

The additional factor 2 arises from the spin degree of freedom and f_+ and f_- represent the Fermi-Dirac distribution function of the left and right moving states. M denotes the number
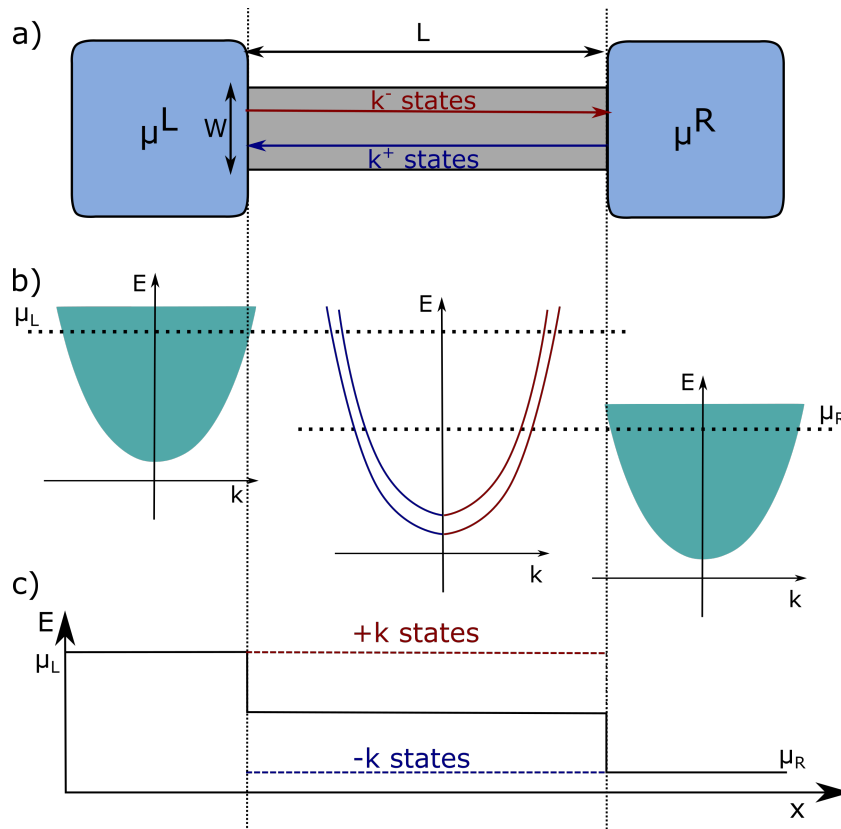
Figure 2.3: a) Illustration of a narrow conductor in between to ideal contacts. b) Electron dispersion in the ballistic wire and the contacts. Within the contacts, the electron dispersion appears continuous because of the high subband density. The narrow wire includes only a few subbands. c) Variation of the quasi Fermi levels along the wire and the contacts. Adapted from [53].

of modes within the conductor and is now assumed to be constant in the energy range of $\mu^l < E < \mu^r$. The conductance can now be calculated by

$$G = \frac{I}{V} = \frac{2e}{h} M \frac{(\mu^l - \mu^r)}{V} = \frac{2e}{h} M \frac{eV}{V} = \frac{2e^2}{h} M \qquad (2.1.10)$$

From this equation it is obvious that the conductance of ballistic wires is quantized and increases with the number of modes present in the conductor. The value $2e^2/h \approx 77.5 \ \mu S$ is referred to as the quantum of conductance G_0.

This result shows, that the current is only dependent on the applied voltage and not on the dispersion of electrons. In experiments, the measured resistance of a ballistic system originates only from the interface between conductor and contact [54]. So far, ideal contacts are assumed, which means that the probability of injection and exit of an electron into and out of the active region is 1. If any kind of scattering is included, the transmission is decreased ($T<1$). Taking this transmission probability for the n-th mode T_n into account, the Landauer fomula is deduced

$$G = 2\frac{e^2}{h} \sum_{n=1}^{M} T_n. \qquad (2.1.11)$$

A generalization of the Landauer formalism to multi-probe systems was developed by M. Büttiker, allowing to determine every current and corresponding resistance in a multi-terminal device [55–57].

2.2 Determination of the material resistivity

The resistivity is a tensor describing the direction dependent components of the electron conductance in a specific material. The most fundamental view on this tensor ρ, is defined as the ratio of an external electric field E and current density J through the material.

$$\rho = \frac{E}{J} \qquad (2.2.1)$$

This simple relation is valid only for isotropic samples in the diffusive transport regime and gets more complex if those conditions are not met. The specific resistivity of a material can be deduced from the resistance. This is very advantageous as the latter can be determined by experiment. To extract the resistivity from a measured resistance value, the geometry and the overall set-up has to be very well known. This prerequisites makes the extraction of the conductivity tensor extremely challenging. The relation of resistance and resistivity for different material systems will be explained in the following.
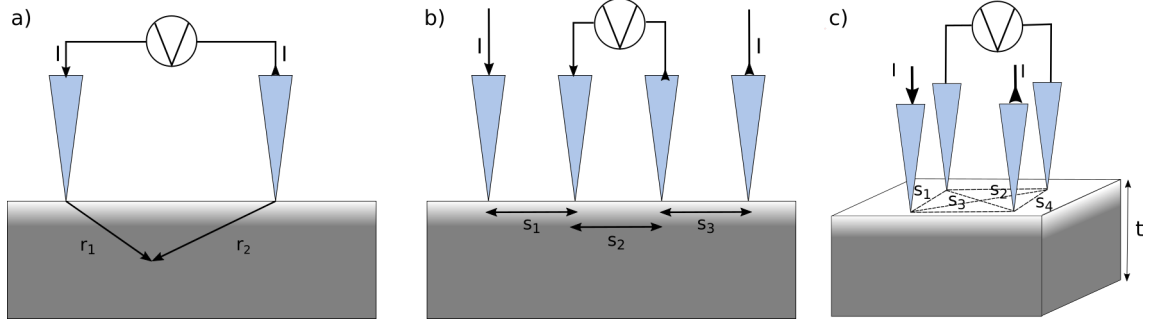
Figure 2.4: a) Schematic representation of a) a 2pp and b) an in line 4pp setup and c)a 4pp square setup for the calculation of the resistance

2.2.1 2-point and 4-point measurements

Two-point probe (2pp) setups are the most simple and intuitive way to measure the resistance of a conductor, the setup is schematically shown in Fig. 2.4 a). Current injection and voltage probing takes place at the same time using the same two probes. This leads to a total Resistance of

$$R_{2pp} = R_{sample} + R_1 + R_2, \tag{2.2.2}$$

which consists of the sample resistance R_{sample} and the resistance of the probes $R_i(i = \{1, 2\})$. The resistance of the probes includes the contact resistance $R_{C,i}$ and the lead resistance $R_{l,i}$. As R_l is usually by far the smallest component of the circuit it can be neglected in most experiments. In experimental use, each contacting process causes a slightly different contact resistance. The need to exactly determine the probes resistances, makes it rather challenging to achieve the extraction of R_{sample} in practical use of this measurement geometry.

A possibility to overcome this limitation is using a four-point probe (4pp) geometry. Two examples for such geometries are shown in Fig. 2.4 b) and c). In the linear case shown in Fig. 2.4 b), the two outer probes serve as current injectors while the voltage is measured in between the two inner probes. The current flowing to the inner probes can be estimated to be zero, due to the high impedance of the voltmeter. Thus, the probe resistance can be neglected and the complete voltage drops over R_{sample}, which means R$_{4pp}$ = R$_{sample}$. This method is only valid if the resistance of the probes can be considered to be orders of magnitude smaller than the input resistance. For metallic samples this is usually the case, anyway for semi-conducting surfaces non-ohmic contacts may occur, resulting in comparatively by high contact resistances up to several MΩ.

2.2.2 Resistivity of confined systems

The resistivity in a 4pp-measurement can be calculated assuming a uniform and infinite sample [58]. The current density J = I/2πr$_1^2$ and the corresponding electric field impinged by a single tip spreads spherically into the sample and is described for a distance r_1 from the tip by

$$E_{r_1} = \rho J = \frac{\rho I}{2\pi r_1^2} = \frac{dV}{dr}. \tag{2.2.3}$$
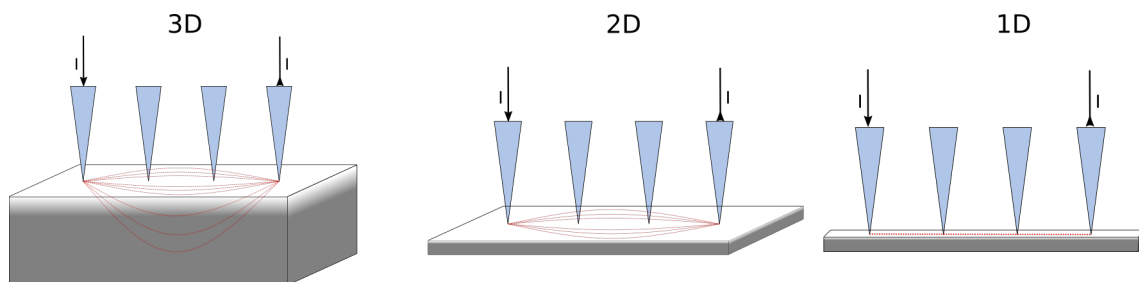
Figure 2.5: Schematic illustration of the current flow in 3D, 2D and 1D

Integration of this relation leads to the potential at a point P

$$\int_0^V dV = -\frac{\rho I}{2\pi} \int_0^{r_1} dr \frac{1}{r^2} \Rightarrow V(P) = \frac{I\rho}{2\pi r_1}. \tag{2.2.4}$$

The voltage drop is given by the difference of potential between two probes

$$V(P) = \frac{I\rho}{2\pi r_1} - \frac{I\rho}{2\pi r_2} = \frac{I\rho}{2\pi}(\frac{1}{r_1} - \frac{1}{r_2}). \tag{2.2.5}$$

This relation can easily be extended to 4 probes in a configuration as shown in Fig. 2.4 b), where the voltage drop is measured between the inner probes. The result for a 4P in line array is then:

$$V = V_1 - V_2 = \frac{I\rho}{2\pi} \left[\left(\frac{1}{s_1} - \frac{1}{s_2 + s_3} \right) - \left(\frac{1}{s_1 + s_2} - \frac{1}{s_3} \right) \right]. \tag{2.2.6}$$

In the case of equidistant probe spacing $s_1 = s_2 = s_3$, as shown in Fig. 2.4 b), this relation simplifies to

$$\rho_{3D}^{line} = 2\pi s \frac{V}{I}. \tag{2.2.7}$$

Things get more complicated if anisotropy or finite sample sizes comes into play. Finite samples require the use of correction factors for finite sample thickness, probes in the proximity of a single sample edge and samples of a finite lateral dimension. These factors were extensively evaluated for two-dimensional (2D) systems by many studies and several mathematical approaches [58–62].

The ratio between the sample thickness t and the probe spacing s determines the dimensionality of the electron transport. This effect is described by the correction factor $F_1(t/s)$ which is determined by

$$F_1 = \frac{ln2}{ln\{[sinh(t/s)]/[sinh(t/2s)]\}}. \tag{2.2.8}$$

When the thickness t of the sample is big compared to the probe spacing, $t/s > 4$, it can be considered of infinite thickness. If one dimension is confined, a semi-infinite 2D system is realized, leading to $t/s << 1$. In this case F_1 becomes unity and the expression for an infinite 2D sheet is determined to

$$\rho_{2D}^{line} = \frac{\pi}{ln2} \frac{V}{I}. \tag{2.2.9}$$

Table 2.1: Bulk resistivity ρ and sheet resistance R_s calculation for linear and square tip arrangements for samples of different dimensions

Sample shape	colinear arrangement	square arrangement
3D bulk	$2\pi s \frac{V}{I}$	$\frac{2\pi s}{2-\sqrt{2}} \frac{V}{I}$
2D sheet	$\frac{\pi}{\ln 2} \frac{V}{I}$	$\frac{2\pi}{\ln 2} \frac{V}{I}$
1D wire	$\frac{\Sigma}{s} \frac{V}{I}$	$-$

In the case of a 2D system, the resistance is no longer dependent on the tip distance. The resistivity can be assumed to be constant for a homogeneous and finitely thick sample, thus the bulk resistivity is often replaced by the so-called sheet resistance R_s, which can be described by

$$R_s = \frac{\rho}{t}. \tag{2.2.10}$$

Although the sheet resistance is measured in Ω, it is often denoted by $\Omega/\square$ to make it distinguishable from the resistance.

Further confinement leads to 1D systems, e.g. atomic wires or carbon nano fibers. The current density is constant in the one-dimensional (1D) case and independent from the electrode distance s. For a circular wire with a radius a much smaller than the probe spacing, the system gets quasi-1D and the current density is calculated to $J = I/(\pi a^2)$. The resistance is known to be proportional to the probe spacing and the relation between measured resistance and resistivity is given by

$$\rho_{1D} = \frac{\Sigma}{s} \frac{V}{I}. \tag{2.2.11}$$

where $\Sigma = \pi a^2$ is the wire section. The sheet resistance of a semi-infinite 2D system and the resistivity of a 1D wire, can still be determined exactly from the measured resistance. These kind of low-dimensional materials can be characterized using modern measurement technologies, achieving the low probe distances needed in this case. For the presented isotropic systems, the resistivity is simplified to being a scalar value instead of a tensor. The dimensionality of the measured electron transport is, of course dependent, on the physical dimensions of the sample and the position of the probes in relation to it.

In experiments, the four probes are often arranged in a square setup as shown in Fig. 2.4 c). This geometry has the advantage, that the required area is significantly smaller. The maximum probe spacing is reduced from 3s to $\sqrt{2}$s. The corresponding calculation for the bulk resistivity ρ and the sheet resistance R_s can be derived from the preciding considerations with $s_1 = s_4 = s$ and $s_2 = s_3 = \sqrt{2}$s. Table 2.1 gives a summary of the relations described so far.

From this relation it gets clear that the sheet resistance is independent from the probe spacing $R_{2D} \propto$ const., while it decreases in the 3D case with $R_{3D} \propto 1/s$. In a 1D system the resistance increases linear with the probe spacing, $R_{1D} \propto s$. The dimensionality is crucial for the scaling behavior of the resistance, therefore, a precise controlled probe spacing in experiment grants access to the system dimensionality.

Table 2.2: Electrical resistance $R_x = V_x/I_x$ for anisotropic 3D and 2D samples and in-line and square probe arrangement

Sample shape	4p in-line	4p square
3D bulk	$\frac{1}{2\pi s_x}\sqrt{\rho_y \rho_z}$	$\frac{\sqrt{\rho_x \rho_z}}{\pi s}[1 - (1 + \frac{\rho_x}{\rho_y})^{-\frac{1}{2}}]$
2D sheet	$\frac{\ln 2}{\pi t}\sqrt{\rho_x \rho_y}$	$\frac{\sqrt{\rho_x \rho_y}}{2\pi t}\ln(1 + \frac{\rho_x}{\rho_y})$

2.2.3 Anisotropy

Anisotropy describes the angle dependent electron transport through a material, resulting in a resistivity tensor rather than a scalar. Remembering the initial description of the resistivity from Eq. 2.2.1, Ohm's Law can be rewritten to

$$\begin{pmatrix} E_1 \\ E_2 \\ E_3 \end{pmatrix} = \begin{pmatrix} \rho_{11} & \rho_{12} & \rho_{13} \\ \rho_{21} & \rho_{22} & \rho_{23} \\ \rho_{31} & \rho_{32} & \rho_{33} \end{pmatrix} \begin{pmatrix} J_1 \\ J_2 \\ J_3 \end{pmatrix} \tag{2.2.12}$$

where E_i and J_i are the electric field and the current density along the i-th direction. The problem occurring in experiments is, to disentangle the single components from each other and fully determine the resistivity tensor. The experimentally measured resistance is no longer proportional to the resistivity, as the I/V ratio in an anisotropic sample measured along an arbitrary axis depends on more than one resistivity component.

The problem of measuring and decoupling of the resistivity tensor components was first solved by Wascher based on an idea of van der Pauw [63, 64] who suggested a transformation of the anisotropic cube with dimensions l onto an isotropic parallelepiped of the dimensions l' using

$$l_i' = \sqrt{\frac{\rho_i}{\rho}}l, \tag{2.2.13}$$

where $\rho = \sqrt[3]{\rho_x \times \rho_y \times \rho_z}$ and $i = \{x, y, z\}$. An in-line geometry on an anisotropic semi-infinite 3D sample is assumed, with the corresponding resistivities ρ_x, ρ_y, ρ_z along the x-,y-, and z-axis, respectively. Assuming the 4 probes aligned on the x-axis of the anisotropic solid with a probe distance s_x. The probes are still aligned after the x'-axis transformation with a distance $s_x' = \sqrt{\rho_x/\rho}$, according to Eq. 2.2.13. V_x and I_x are preserved during the transformation and the resistivity for isotropic samples is, given by 2.2.7 as:

$$\rho = 2\pi\sqrt{\frac{\rho_x}{\rho}}s_x\frac{V_x}{I_x}. \tag{2.2.14}$$

The resistance along the x-axis $R_x = V_x/I_x$ allows to rearrange this relation to be:

$$R_x = \frac{1}{2\pi s_x}\sqrt{\rho_y \rho_z}. \tag{2.2.15}$$

The case of 2 dimensional samples can be solved by a similar approach. An overview of the determined formulas for in-line and square configurations are given in Table 2.2. While in the 3D cases the resistance still decreases with increasing probe distances, it remains constant in

the case of an infinte 2D sheet. To gain information about the anisotropy, either the probes need to be rotated or the current/voltage probes have to be exchanged. Rotation of the probe array by 90° leads to the measurement of $R_y = V_y/I_y$. The anisotropy value R_x/R_y is easily obtained, if the probes are assumed to be aligned at the x- and y-axis. It is obvious, that a square arrangement of probes is more sensitive to anisotropy compared to the linear geometry. In case of anisotropic 2D systems, the determination of anisotropy via the two components ρ_x and ρ_y is only possible using the square arrangement.

Anyhow, if the contacts are not perfectly aligned along the main axis, the evaluation of data gets more complicated. If the 4PP array is rotated by an arbitary angle Θ with respect to the two othogonal main axis, the equation for resistivity changes to:

$$R(\rho_x, \rho_y, \Theta) = \frac{\sqrt{\rho_x \rho_y}}{2\pi t} ln \sqrt{\frac{(1 + \frac{\rho_y}{\rho_x})^2 - 4cos^2\Theta sin^2\Theta(1 - \frac{\rho_y}{\rho_x})^2}{(sin^2\Theta + \frac{\rho_y}{\rho_x}cos^2\Theta)^2}}. \tag{2.2.16}$$

The highest anisotropy is naturally seen for two orthogonal contact configurations. For systems with an extremely high anisotropy, i. e. $\rho_x/\rho_y > 20$, negative resistance appears due to a deformation of the electrostatic potential.

2.2.4 Inhomogenities

The discussion in the previous sections is only true for homogeneous samples. The determination of the conductivity tensor for an inhomogeneous material is still even more complex and cannot be accessed from the experimental side only. In modern technology, large scale fabrication of materials, build up from microscale elements can lead to inhomogenities in the sample. To characterize the homogeneity, mapping approaches can be used, including the characterization via fixed or movable contacts and terahertz time-domain spectroscopy [65]. For inhomogeneous, anisotropic materials, the dimensionality cannot simply be determined by resistivity measurements with different probe distance. Furthermore, the anisotropy cannot reliably be measured by a rotational square measurements.

An alternative is given by simulating the correlating microscopic and macroscopic properties of materials. For example, 1D building blocks such as carbon nano fibers were used to model the properties of 3D macroscopic samples [66–68]. Very recently, simulations based of resistor networks were established to model system made up from 2D building blocks [36, 37, 69]. Based on this simulation approach, anisotropic materials can be analyzed. Through these simulations the possibility of detangling the conductivity components is provided.

2.3 Localization

Localization describes a limitation of the propagation of waves due to scattering in disordered systems. The effect can be divided in weak and strong localization. If the distance between scatterers in an array is longer that the phase relaxation length, the resistance of this array increases linearly with its length, following Ohm's law.

Anderson showed, that electrons can be localized by a random potential, suppressing diffusion even though classical particles would be delocalized [70]. The fundamental basis of

localization, is the multiple interference of wave components, which are scattered by random scattering centers.

The particles become localized if the disorder is sufficiently strong. The envelope of the wave function decay exponentially from a point r_0 in space:

$$|\Psi(r)| \propto exp(|r - r_0|/\xi). \tag{2.3.1}$$

where ξ describes the localization length. Electrons are scattered after an average time of τ when propagating in a random potential $V(r)$.

2.3.1 Anderson localization

The Anderson localization is a transition, tuned by a control parameter like the particle wave frequency, the particle energy or the disorder strength. At positions where the random potential forms a deep well, localized orbitals exist. Because of the different energies of the orbitals, the overlap and admixture is small. Orbitals close in energy are spatially apart, so the overlap is exponentially small. Based an these assumptions, the electron wave functions are expected to be exponentially localized in strongly disordered systems. In the special case of one dimensional systems, all states are localized, independent of how weak the disorder is [71].

Moving towards three dimensions, particles within a system are delocalized for weak disorder. Localized and extended states cannot coexist, because any perturbation would induce hybridization and therefore delocalization. Localized and extended states of a certain energy can be assumed to be spatially separated. With increasing disorder, a sharp transition from delocalized to localized states occurs, at a critical disorder strength ν_c or energy. Ioffe and Regel introduced a qualitative criterion for when the Anderson transition is expected in three-dimensional (3D) systems [72]. As the main free path λ_e is reduced by increasing disorder, its value gets smaller than the Fermi wavelength of the particle. This is when the Anderson transition occurs.

$$\lambda_e < \lambda_F. \tag{2.3.2}$$

The relevant mean free path in this consideration belongs to the momentum transfer. With a fixed disorder strength and varying energy a similar transition can be observed. The corresponding, critical energy, separating the localized from delocalized states is called mobility edge [73, 74]. At zero temperature, the energy dependent electron mobility vanishes on the localized site and increases continuously with energy separation in the delocalized phase.

2.3.2 Transition in 1, 2 and 3 dimensions

A d-dimensional cube of length L is assumed to have a dimensionless conductance g in units of the quantum of conductance, $g = \frac{G}{e^2/\hbar}$. In strongly disordered systems, all states are expected to be localized with an average localization length ξ. This means, that $g(L)$ is exponentially decreasing with increasing L

$$g(L) \propto e^{-L/\xi} \tag{2.3.3}$$

Abrahams et al. [75] defined $\beta(g)$

$$\frac{dlng}{dlnL} = \beta(g) \tag{2.3.4}$$

as a function of g only, which is not dependent on the disorder and can be calculated within the limits of strong and weak disorder. For strong disorder β is determined to

$$\beta(g) \propto ln(g/g_c) < 0, \tag{2.3.5}$$

and does not depend on the dimensionality.
Within the conditions of weak disorder, where the conductance behavior is ohmic,

$$g \propto L^{d-2} \tag{2.3.6}$$

holds true. This means β is given by

$$\beta(g) = d - 2 \tag{2.3.7}$$

The question whether the system is localized or delocalized is answered by integrating the equation from a starting point L_0 with known conductance. Depending on whether β along the integration path is positive or negative, the conductance will vanish or become infinite for L.
In three dimensions (d = 3) both cases $\beta(g) > 0$ and $\beta(g) < 0$ exist for large and small g, respectively. A point exist where β vanishes, this marks the separation in between localized and delocalized states. In one dimension, β is always negative, indicating only localized states exist in the system. In two dimensions, $\beta \to 0$ for g $\to \infty$. To determine whether β is positive or negative for large g, scale dependent corrections need to be applied to the results based on the Drude model. With addition of a correction factor β is determined by [75]

$$\beta(g) = (d-2) - \frac{a}{g}, \tag{2.3.8}$$

where a = $2/\pi$. This means $\beta(g) < 0$ for all g, indicating all states are localized.

2.3.3 Temperature dependence and variable range hopping

The particle energy, and therefore the temperature, is one of the key parameters driving the Anderson localization. In a degenerate electron gas, the metal-insulator transition (MIT) occurs if the Fermi energy E_F moves across the critical energy, or mobility edge, E_c [76]. Analog to the consideration of the conductivity, the conduction will be ohmic if $E_F > E_c$. In the case of $E_F < E_c$ the states become localized. The conductance of a localized system decreases with decreasing temperature. At high temperatures, transport occurs via excitation to the mobility edge, the conductance is given by:

$$\sigma = \sigma_0 e^{-(E_c-E_F)/k_B T} \tag{2.3.9}$$

At low temperatures transport via variable-range hopping from one localized state to the other is expected. Neglecting electron-electron interactions, the conductivity follows [77]

$$\sigma \propto e^{-(T_0/T)^{\frac{1}{4}}}, \tag{2.3.10}$$

in the three-dimensional case and can be generalized to d dimensions

$$\sigma \propto e^{-(T_0/T)^{1/(d+1)}}.$$ (2.3.11)

Where T_0 is correlated with the localization length ξ and the density of states at the Fermi energy $D(E_F)$ as follows

$$T_0(\xi) \approx 14(\xi\, 2k_D(E_F))^{-1},$$ (2.3.12)

where k_B denotes the Boltzmann factor [74, 77]. Subsequently, Ambegoakar et al. derived the same behavior as shown in Eq. 2.3.11 by the percolation method [78].

2.4 Transport through molecules

A molecular junction consists of a molecule, acting as a wire, in between two electric contacts. The most simple approach to describe the electron transport through such a system is based on the Landauer theory described in Sec. 2.1.3. It is assumed that incoming electrons are scattered at the metal molecule interfaces and along the molecular wire itself. The scattering processes does not necessarily have to be inelastic. Elastic scattering as well will prevent the electrons from passing through the junction.

This fundamental viewpoint suggests the resistance of the junction arises from scattering. This coherent conductance is suitable for the characterization of most short molecular wires, particularly at low temperatures. Under those conditions the conductance g(E,V) is given, based on the Landauer theory by

$$g(E,V) = \frac{2e^2}{h} \sum_{i,j} T_{i,j}(E,V)$$ (2.4.1)

The prefactor equals the quantum of conductance and $T_{i,j}$ describes the probability of a carrier passing through the molecule from the left electrode in transverse mode i to be transmitted into the right electrode in transverse mode j.

Coherent as well as incoherent transport is observed in molecules and will be explained in more detail in the following sections 2.4.1 and 2.4.2. In complex biomolecules, an overlap between both mechanism is observed leading to an intermediate regime, as described in Sec. 2.4.3.

2.4.1 Coherent transport: tunneling

Coherent transport means, the phase information of the wave function associated with the propagating electron is preserved and inelastic interactions only take place inside the electrodes. In the most simple case, the transport mechanism is described by quantum mechanical tunneling through a potential barrier. The barrier in this case originates from the molecule inside the junction.

A potential barrier with the height V_0 and the width L is assumed. From a classical point of view, a particle will be reflected when E < V_0 and transmitted when E > V_0.

Within the framework of quantum mechanics, determination of the the electrons wave function is needed, therefore three regimes are defined as depicted in Fig. 2.6. The wave functions in each of these regions and their first derivatives are matched at the boundaries (x = 0 and
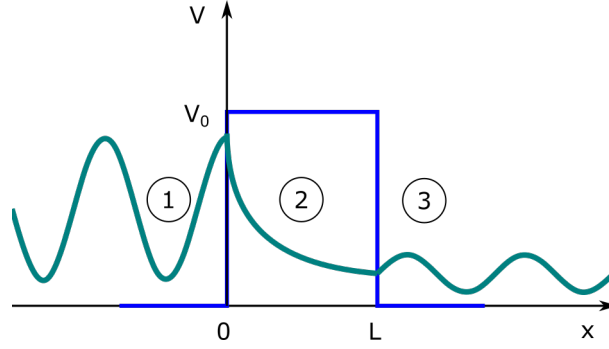
Figure 2.6: Tunneling through a potential barrier (blue). Three regions are indicated by numbers that are considered indivudially. The wave function of an electron in each of the regions is indicated in cyan.

x = L), this is schematically shown in Fig. 2.6. The effective mass is assumed to be constant over the whole range and the solutions of the Schrödinger equations in the three regions are of the form

$$\psi_1 = a_1 exp(ik_1 x + b_1 e^{-ik_1 x})$$
$$\psi_2 = a_2 exp(ik_2 x + b_1 e^{-ik_2 x}) \tag{2.4.2}$$
$$\psi_3 = a_3 exp(ik_1 x),$$

where the wave vector in the regimes x < 0 and x > L is, identical ($k_1 = k_3$) because V(x) = 0 in both cases. *a* and *b* describe the amplitude of a wave moving in positive or negative direction along the x-axis respectively. The wave vectors are determined to

$$k_1 = \sqrt{\frac{2mE}{\hbar^2}}$$
$$k_2 = \sqrt{\frac{m(E - V_0)}{\hbar^2}} \tag{2.4.3}$$

Using the first derivative and the continuity of the wave function of the position x = 0 and x = L and solving these equations, the expression for the energy dependent transmission coefficient for E < V_0 is derived:

$$T = \frac{4E(V_0 - E)}{4E(V_0 - E) + V_0^2}. \tag{2.4.4}$$

The transmission is exponentially dependent on the barrier width. Based on Eq. 2.4.2 and Eq. 2.4.4 this decay is given by

$$T \propto exp(-2k_2 L) = exp(-2L\sqrt{2m_e(V_0 - E)}/\hbar). \tag{2.4.5}$$

Keeping in mind, that the conduction is determined from the transmission, this consideration explains the exponential decay of conductance within tunnel barriers of all kinds with the electrode distance, as described by

$$G(L) = Aeyp(-\beta L) \tag{2.4.6}$$

where L is the length of the molecules and A is a prefactor determining the order of magnitude of the conductance. This is of course also true for molecular junctions where tunneling is the dominant transport mechanism. The attenuation factor β depends on the particular molecule and is quite independent of the anchoring. Typical values for β for conjugated molecules range from $0.2\,\text{Å}^{-1}$ to $0.4\,\text{Å}^{-1}$, while the value is even higher for aromatic compounds, ranging from $0.8\,\text{Å}^{-1}$ to $1.2\,\text{Å}^{-1}$ [79–86].

To describe the I-V characteristics of system where tunneling is the dominant transport mechanism, the energy and voltage dependent transmission probability is required. To describe the effect of an external voltage to the barrier, a linear drop in the potential within the barrier region is assumed. Simmons derived a formula for the I-V curves of a barrier of arbitrary shape in 1963 [87]. At zero temperature the current through a rectangular barrier can be written as:

$$I = \frac{e}{2\pi g \alpha^2 L^2} \overline{V_0} e^{(-A\sqrt{V_0})} - (\overline{V_0} + eV)e^{-A\sqrt{V_0 + eV}}, \qquad (2.4.7)$$

where $\overline{V_0}$ is the average barrier height relative to the negative electrode and

$$A = \frac{2\alpha L}{\hbar}\sqrt{2m_e}. \qquad (2.4.8)$$

In this case α is a dimensionless correction factor. Depending on the bias regime, this formula can be further simplified. It is worth paying attention to the fact, that this transport mechanism is rather insensitive to temperature.

When considering molecular junctions, not only a double barrier needs to be passed, but also the energetic position of the highest occupied molecular orbital (HOMO) and lowest unoccupied molecular orbital (LUMO) with respect to the Fermi energies of the electrodes plays a role. These effects are not taken into account by the Simmons model.

Depending on the interaction in between the molecule and the electrodes, charge flow, rearrangements and geometric reorganization occurs. The transmission within the molecules and the corresponding phase coherence starts to influence the transport. Hybridization of the molecular orbitals and the metallic states induce a finite broadening, which is dependent on the coupling strength. This causes the molecular states to have a finite lifetime. In the most simple case, one molecular orbital - either HOMO or LUMO depending on the molecular structure - dominates the electron transfer in a certain voltage range. This scenario can be described by a single level resonant tunneling model.

It is assumed, that the contributing molecular orbital has an energy of $\epsilon_0(V)$. An external bias voltage shifts the level with respect to the Fermi energies of the contacts, which are set to 0 within this consideration. The key parameters in this model are the scattering rates in between the molecular bridge and the contacts. $\Gamma_{L,R}$ for the left and right contact respectively, describe the coupling strength and have dimensions of energy. They determine the lifetime or broadening of the molecular level. The chemical bond in between the electrodes and the molecules were found to have a significant effect on the electron transport through molecules, allowing tailoring of electronic properties by chemical modification of specific groups and compounds [82, 89–98].

The energy and voltage dependent transmission coefficient can be determined via the Breit-Wigner-Formula [99]. This is a valid assumption for noble metals like gold, showing a rather
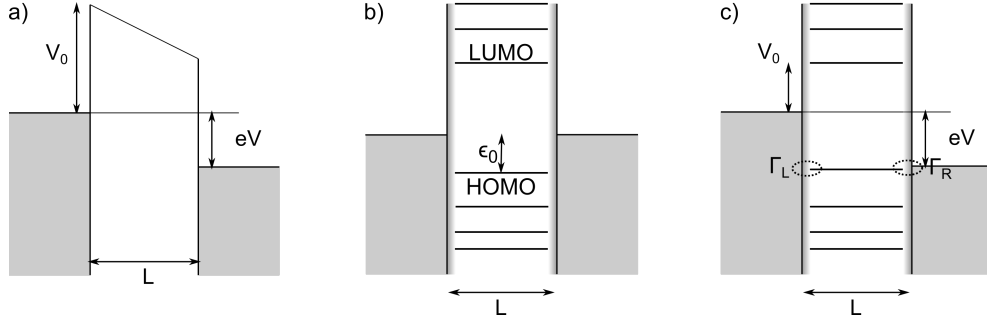
Figure 2.7: a) Schematic representation of a tunneling junction as explained by the Simmons model. b) and c) Coherent tunneling through a molecular junction without (b)) and with (c)) applied bias voltage. Adapted from [88].

flat density of states around the Fermi energy.

$$T(E,V) = \frac{4\Gamma_L \Gamma_R}{[E - \epsilon_0(V)]^2 + [\Gamma_L + \Gamma_R]^2} \tag{2.4.9}$$

Now, the current can be calculated following the Landauer approach [100]:

$$I(V) = \frac{2e}{h} \int_{-\infty}^{\infty} T(E,V) \left[f(E - eV/2) - f(E + eV/2) \right] dE. \tag{2.4.10}$$

The temperature dependence of coherent transport is deduced by the energy dependence of the transmission which is usually not very pronounced. Based on the former assumption the temperature dependent conductance in the linear regime is given by

$$G(T) = \left(\frac{2e^2}{h}\right) \frac{1}{4k_b T} \int_{-\infty}^{\infty} \left[\frac{4\Gamma_L \Gamma_R}{(E - \epsilon_0)^2 + \Gamma^2} \right] \frac{1}{cosh(\beta E/2)} dE, \tag{2.4.11}$$

where $\beta = 1/k_B T$. If an off-resonant situation is considered ($|\epsilon_0| > \Gamma, k_B T$) the conductance remains completely temperature independent.

2.4.2 Incoherent transport: hopping

With increasing length of the molecular bridge it becomes more probable, that the tunneling traversal time gets larger than the time scales associated with inelastic interactions. In the regime, where coherence is completely lost, the electrons tunnel sequentially from one segment of the molecule to the other. This is designated as hopping transport.

This transport regime can be described by a model of a molecular bridge with N states with the ascribed transfer rate $k_{i,j}$ in between the states i and j. For simplicity, all states are assumed to have the same energy, which differs from the Fermi energy of the metallic electrodes by ΔE. The value ΔE is the injection energy which, in this model, acts as an activation energy. This situation is depicted in Fig. 2.8.

The current between the two molecular sites i and $i{+}1$ is determined by the occupations P_i and P_{i+1} of those two sites. The current itself is conserved and it gets irrelevant where it
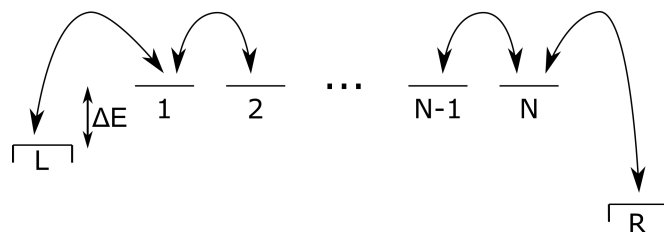
Figure 2.8: Schematic representation of the hopping transport model. N sites are connected via the transfer rates $k_{i,i+1}$. The left and the right states, marked with L and R, correspond to the electrodes. Adapted from [88].

is evaluated. It can be determined to [101–103]

$$I_j = e(k_{i+1,i}P_i - k_{i,i+1}P_{i+1}), \tag{2.4.12}$$

For simplification the transfer rates in between the internal bridge sites are assumed to be equal: $k_{i,i+1} = k$. The transfer rates to the left and right electrodes are designated as k_L and k_R, respectively. Furthermore a stationary situation is assumed, which means $dP_j/dt = 0$. The occupancy of the electrodes is determined by the Fermi functions, $P_0 = f_L$ and $P_{N+1} = f_R$.

Combining all these assumptions and keeping in mind, the tunneling is incoherent, classical kinetic equations can be used and simplified to show the charge current is given by [88]

$$I = e \frac{e^{-\Delta E/k_B T}}{[1/k_L + 1/k_R + (N-1)/k]} e^{eV/k_B T}(f_L - f_R). \tag{2.4.13}$$

Based on this, the linear conductance is determined to

$$G = \frac{e^2}{k_B T} \frac{e^{-\Delta E/k_B T}}{[1/k_L + 1/k_R + (N-1)/k]}. \tag{2.4.14}$$

From Eq. 2.4.14 two crucial signatures of hopping conductance can be determined. First the conductance decays linearly with the number of segments within the molecular bridge, and therefore with the molecular length. If the activation process is ignored, a simple combination of resistors in series is adopted, leading to a simple explanation for the linear relation.

The second signature is the exponential dependence of the conductance on the temperature. In the presented model, this is due to the process taking place at the metal molecule interface, but in general it can be located anywhere within the junction.

Within the framework of this simplified model, the main signatures of hopping conductance can be explained, but no quantitative predictions can be generated, especially the transition from coherent to incoherent transport is ignored by this simple model.

2.4.3 The intermediate regime: biomolecules

Biomolecules reveal a large number of parameters that can be utilized for functionalization e.g., the secondary structure, sequencing of subunits, polarization, dipole moments, chirality, oxidation potential or hydrogen bonding [85]. This flexibility and large variety makes

understanding of the electron transfer through this systems a complex problem, that is not resolved completely until today [104, 105].

When analyzing the electron transfer through biomolecules regarding length dependence, coherent tunneling transport is the most common mechanism through short molecules while incoherent hopping is dominant for long molecules. This two borderline cases are too simple to generate a general transport model for biomolecules. In systems were the molecular length can be tailored, like DNA and polypeptides, the two different mechanisms, explained before, were observed in the same molecules for long and short sequences.

In between those two limiting cases, the coexistence of both mechanisms were proposed by several studies investigating the transport properties of DNA [106]. This is in line with the earlier propagated model of superexchange. There the carriers are assumed to only virtually reside on the intermediate bridge units instead of incoherent hopping transfer in between distant redox centers [85, 107–110].

Additionally, within solid state junctions the molecules are exposed to large electric fields, which may induce a Stark effect and renormalize the molecular orbitals, as exemplarily showed on 15mer polyalanine [111]. For peptides correlated transport phenomena might also be of importance. A recent study reported that, two-step electron transfer is faster than single step reactions [109].

In summary, the detailed description of electron transport through biomolecules is still puzzling. Unresolved questions are e.g. the transition from a conducting to a insulating state upon mechanical stretching in OPE3 molecules [112] or the exact mechanism behind the chiral induced spin selectivity (CISS) effect that will be explained in more detail in Sec. 6.1.1.

Part II

Experimental results

Experimental methods

In this Chapter, the experimental measurement methods are explained. The surface transport investigations analyzing adsorbates on graphene (Chpt. 4) and the characterization of carbon-based compound materials (Chpt. 5) are performed by means of four-point probe (4pp)-scanning tunnelling microscope (STM) combined with scanning electron microscope (SEM). A description of the overall system, is presented in Sec. 3.1.1 followed by a detailed explanation of the measurement setup in Sec. 3.1.2.

Transport measurements through single molecules were performed using mechanically controllable break junction (MCBJ). The sample fabrication is presented in Sec. 3.2.1, followed by a description of the instrumentation and measurement principle Sec. 3.2.2.

3.1 The 4pp-STM/SEM

Establishing an electric contact in between a macroscopic measurement device and a nanoscopic system is technically very challenging. The used 4pp-STM/SEM system is designed by and purchased from Omicron Nanotechnology GmbH. The setup is explained in more detail in the following.

3.1.1 UHV chamber and overall setup

Since transport measurements on nanostructures are very sensitive to contamination, the transport investigations are performed under ultra-high vacuum (UHV) conditions at a base pressure of 3×10^{-10} mbar. The system is divided in two main parts: An analyzing chamber, consisting of the 4pp-STM and a SEM, and a preparation chamber which allows the in-situ manipulation of samples. An overview over the chamber is schematically shown in Fig. 3.1 a). Sample and tips can be transferred into the system via load locks without breaking the vacuum conditions.

The preparation chambers manipulator allows sample heating either via a backside filament or direct current as well as liquid nitrogen cooling. Up to three evaporators can be used for
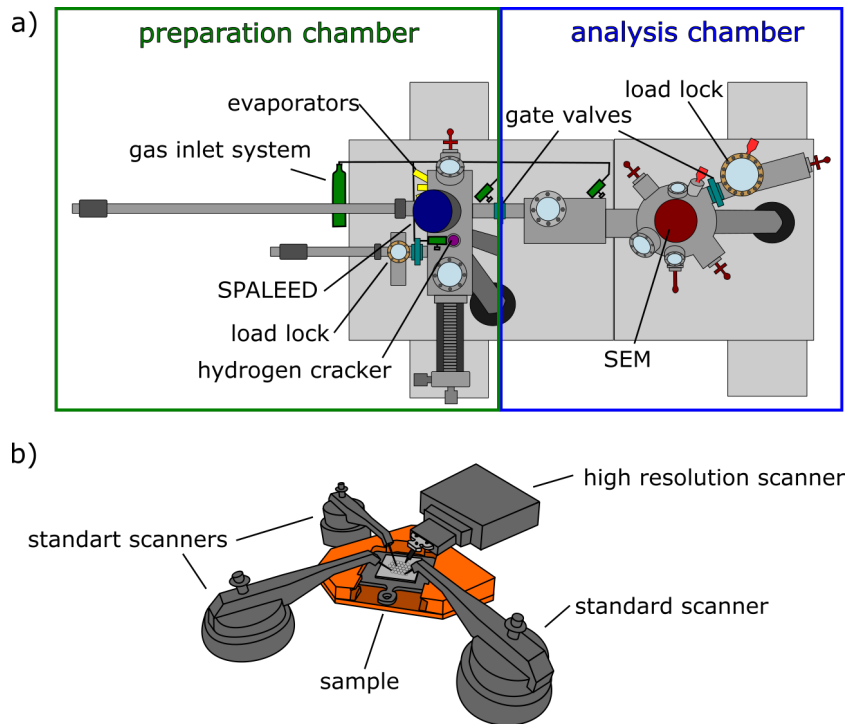
Figure 3.1: a) Schematic picture of the UHV setup. The system is divided into a preparation and an analysis chamber. The preparation chamber features several evaporators, a hydrogen cracker and a SPALEED for structural analysis. The STM itself and the SEM are located in the analysis chamber. A gas inlet system allows the exposure of samples to determined partial pressures of different gases. Samples and tips can be transferred to the UHV vie the load locks.b) Schematic representation of the multi-tip STM consisting of three standard and one high resolution scanner. Fig. b) adapted form [113].

direct thin film deposition. A gas inlet system combined with a hydrogen cracker can provide both atomic and molecular gases, like hydrogen, CO and O_2.

Structural analysis can be performed using the spot profile analysis low energy electron diffraction (SPALEED) system mounted to the preparation chamber. The diffraction pattern allows conclusion regarding the crystallographic structure and properties. Unless declared otherwise all used samples were degassed for at least 4 h at a temperatures of 450 °C.

Electrical transport measurements are performed in the analysis chamber which consists of the multi-tip STM and a high resolution SEM. The sample can be heated and cooled during the measurement. Cooling with liquid nitrogen or helium leads to an minimum sample temperature of 80 K or 25 K respectively.

The separation of the two parts allows sample preparation at elevated pressure without compromising the pressure within the measurement system itself.

3.1.2 The 4pp-STM measurement setup

The multi-tip STM is build up from 4 scanners. All scanners are fully feedback controlled STMs. This capability is needed to allow the navigation of the tips on the sample surface

within a nanoscale. One of those scanners is a so-called high resolution scanner. While this special scanner is better protected against vibration and usually used for STM measurements, the other three are mainly applied for transport investigations.

All transport measurements were performed using electrochemically etched tungsten tips. Voltage pulses with up to $\pm 10\,\mathrm{V}$ are used to clean the tips before measurements.

To allow a precise positioning of the tips of the 4pp-STM, a SEM is mounted above the stage. The column is a GEMINI type, commercially fabricated by Carl Zeiss AG. The electron beam is generated by a field emission cathode, where electrons are extracted by a strong electric field from a filament tip. The tip is additionally heated to generate a high emission current and beam stability. The GEMINI type column features an additional booster voltage, applied after extraction of the electron beam, to maintain a high beam energy throughout the whole column. On the lower end of the column, close to the sample, deceleration of the electrons to the chosen energy takes place. This technique leads to a small beam diameter and minimizes the effect of aberration. This is of high importance in this specialized system, because due to the STM scanners the working distance of approx. $15\,\mathrm{mm}$ is relatively large. The images are generated by the signal of an in-line secondary electron detector.

The tips are held in feedback controlled mode to allow navigation across the sample without crashing. The feedback mode was turned of for the measurement itself and the tips are manually lowered via piezo elements towards the sample surface. The resistance is checked during this lowering to find stable contact conditions without crashing. A direct contact between tips and sample is achieved, leading to an ohmic contact on metallic surfaces. The contact conditions and resistance values of each tip are checked subsequently to ensure all probes are properly approached. Voltage and current is sourced and probed by means of a Keithley sourcemeter.

On of the main advantages of this measurement system is its flexibility. There are no limitations of probe arrangements beside the size of the tips and the sample. This allows any kind of probe spacing and geometries.

3.2 Mechanically controllable break junction (MCBJ)

The MCBJ approach is based on stretching a thin metallic wire down to an atomic point contact. Due to the geometry this kind of setup provides a high stability at a wide range of conditions. MCBJ has proven to be a flexible, stable and reliable tool to analyse the properties of single molecules [114–117]. The samples were structured by electron beam lithography to achieve a constriction of few micrometers providing a base for the formation of stable atomic gold (Au) contacts. The detailed process of sample fabrication is shown in the next section, followed by a description of the measurement principle.

3.2.1 Sample preparation

The samples were fabricated using the technique of electron beam lithography (EBL), an overview over the fabrication process is given in Fig. 3.2. A $125\,\mu\mathrm{m}$ thick stainless steel substrate is used to ensure flexibility of the sample. A polyimide layer is applied via spin coating to provide electrical insulation of the gold structure from the substrate.

Au contact pads are fabricated by shadow mask evaporation, building up from $8\,\mathrm{nm}$ of

1. Stainless steel substrate

125µm thickness

2. Polyimide coating

Spin coating insulating layer

3. Contact pad deposition

Shadow mask evaporation
of contact pads

4. E-beam resist coating

Spin coating
200nm MMA + 180nm PMMA

5. E - beam exposure

Exposure at 30kV, 340µC/cm²

6. Development

Metylisobutylketone (MIBK)

7. Metal deposition

Deposition of 7nm Cr
+ 70nm AU

8. Lift off

Lift off in Acetone

9. Reactive ion etching

RIE in O_2/CHF_3 80:20
atmosphere

Figure 3.2: Fabrication process of the electron beam structured MCBJ samples, starting with a stainless steel substrate. An insulating layer is spin coated, followed by macroscopic contact pads. The electron beam lithography is done with a double layer resist. The structure is developed after exposure and the bridge is formed by Au evaporation. Metal and resist residuals are removed during lift off. As a final step reactive ion etching is used to generate a freestanding structure.

chromium (Cr) as an adhesive layer followed by 100 nm Au. Those contact pads allow to contact the sample with macroscopic spring contacts, eliminating the need for further lithography steps.

A double layer of positive electron beam resist (methylmethaacrylate (MMA) and polymethylmethaacrylate (PMMA)) is used for structuring. The different behaviour under development of the two resists generate a protrusion, simplifying a clean lift off. The incident electron beam triggers a chemical modification in the resist, leading to solubility of the exposed parts upon development. Electron beam structuring was done using a JEOL-SEM 5900, equipped with an Raith lithography stage, at an acceleration voltage of 30 kV and a dose of $340 \, \mu C/cm^2$. After exposure and development, 5 nm Cr to ensure adhesion and 70 nm Au is evaporated, forming the constricted structure defined by the lithography step. The remaining resist is removed during the lift off.

As a final step, the polyimide layer is etched via reactive ion etching (RIE) in an O_2:CHF_3 atmosphere, resulting in an underetched middle part of the structure. A freestanding Au bridge is formed, allowing the stretching and breaking of the structure.
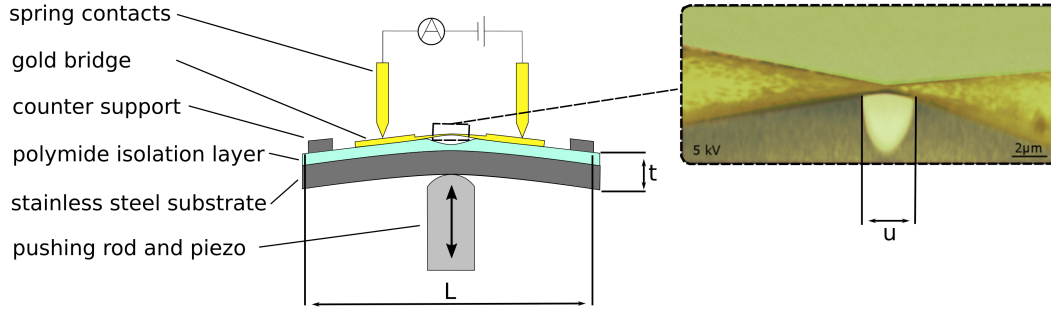
Figure 3.3: Setup for electronic transport measurement. The structured sample is stretched and broken by an piezo motor. The geometry of the setup allows very precise control of the electrode distance. The inset shows a false color SEM image recorded under a tilted angle. The freestanding part of the Au wire can clearly be seen. (Fig. taken and modified from [119])

3.2.2 Instrumentation and measurement principle

Transport measurements were performed using the setup depicted in Fig 3.3. The freestanding gold bridge is elongated by deforming the substrate from underneath by a piezo motor. The small step size of the motor combined with the sample geometry allows a very precise control of the contact formation. The relation between the movement of the motor and the total change of length modification of the sample can be described by the reduction factor R, given as

$$R = \frac{6tu}{L^2} = 7.3 \times 10^{-6} \tag{3.2.1}$$

where, t denotes the thickness of the structure of 138 μm, u the length of the freestanding bridge, denoted from the SEM images to be ≈ 2 μm and L the overall length of the sample of 15 mm, resulting in a reduction factor of 7.3×10^{-6}. Once the gold bridge is broken, forming atomic contacts, the electrode distance can be manipulated with sub-nm range precision due to the µm step size of the piezo [118].

All measurements were performed under high vacuum conditions at a pressure of 10^{-6} Pa, providing an extremely clean environment. Unfortunately, the vibrations of the necessary vacuum pumps limit the stability of the measurement.

Conductance traces were recorded by applying a constant voltage in between 1 mV and 100 mV and carefully bending the sample. Upon thinning of the wire a quantization of conductance can be observed, which can be seen as defined steps in the measurement. By sweeping the voltage IV curves can be measured at a fixed electrode distance, allowing deeper insight into the electron transport mechanism.

The Au bridge was fused after every conductance measurement and opened again to ensure clean contacts.

polyalanine (PA) molecules were introduced to the junction via a solution, formed by 0.1 mM propylene glycol with 25wt% trimethylamine as a solvent. The solvent desorbs during the pumping process and only the PA molecules remain at the surface as a self assembled monolayer (SAM).

Adsorption of atomic and molecular species on graphene

Graphene is a monolayer of carbon, formed by atoms arranged in a honeycomb lattice. The material is widely known for its extraordinary physical properties and is heavily under research interest since its discovery in 2004. There is a wide variety on possible applications for this material, reaching from electrical and thermal conducting purposes to sensors. An overview over the structural and electronic properties of graphene is given in Sec. 4.1, followed by a description of the production of epitaxial graphene on silicon carbide (SiC) substrates in 4.2.

Hydrogen adsorption to graphene is analyzed and explained in Sec. 4.3, followed by the presentation of the results on lead phtalocyanine (PbPc) molecules on hydrogenated graphene samples in Sec. 4.4. Finally, this chapter is concluded and summarized in Sec. 4.5.

The project was realized in the framework of the hanover school of nanotechnology doctorate program, a cooperation of the groups of Prof. Tegenkamp (Technische Universität Chemnitz), Prof. Sindelars (University of applied sciences Hannover) and Prof. Renz (located at the Institute of inorganic chemistry, Leibniz Universität Hannover).

4.1 Structural and electronic properties

Graphene is an atomic layer of carbon and consists of sp^2-hybridized atoms. Each atom forms three covalent σ-bonds with an angle of $120\,^\circ$ relative to each other. This leads to the formation of a hexagonal planar atomic configuration with honeycomb arrangement.

One additional perpendicular π-bond is formed by the $2p_z$ orbital. The electrons in this π-system are delocalized – mimicking a two-dimensional (2D) electron gas– causing the outstanding electronic properties of graphene. Although the notation *graphene* refers to single atomic layer of graphite, it is often used for multilayer system up to up to ten layers at all. In this case, the binding energy between carbon atoms within one layer is by far larger than the binding energy in between the layers (4.3 eV compared to 0.07 eV). This is the reason
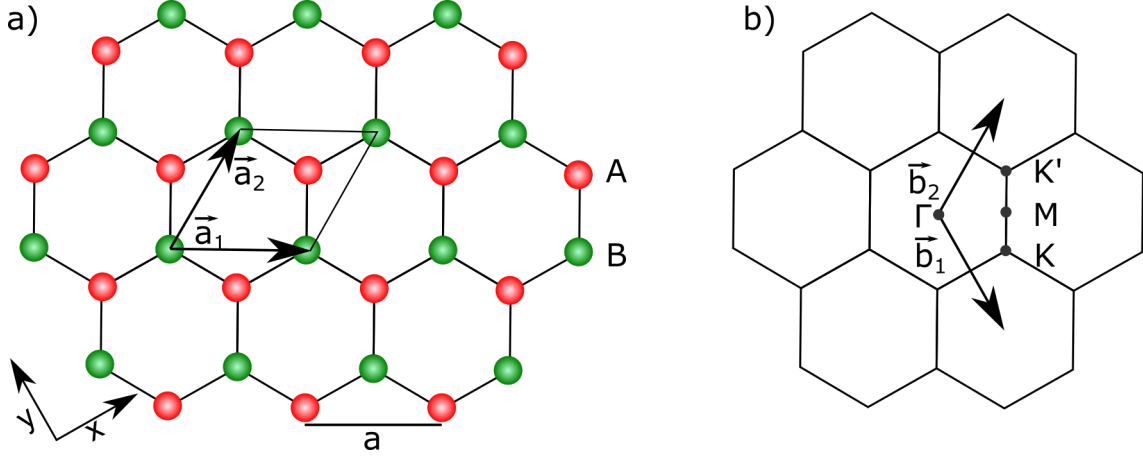
Figure 4.1: a) The graphene lattice with its two sublattices A and B (marked in green and red respectively). The unit cell is defined by the lattice vectors $\vec{a_1}$ and $\vec{a_2}$. b) Reciprocal lattice of graphene with marked Γ, K, K' and M point and the reciprocal lattice vectors $\vec{b_1}$ and $\vec{b_2}$.

why the mechanical exfoliation of graphene layers from graphite crystals works surprisingly well [26].

The lattice structure of graphene can be described by a triangular Bravais lattice with a base of two atoms per unit cell (see Fig. 4.1 a)). The unit cell vectors $\vec{a_1}$ and $\vec{a_2}$ are defined by

$$\vec{a_1} = \frac{a}{2}\left(3, \sqrt{3}\right) \; ; \; \vec{a_2} = \frac{a}{2}\left(3, -\sqrt{3}\right), \tag{4.1.1}$$

where a is the carbon-carbon distance of 1.45 Å and the lattice constant of the honeycomb structure is a $= |\vec{a_1}| = |\vec{a_2}| \approx 2.46$ Å. The corresponding reciprocal lattice is shown in Fig. 4.1 b). The reciprocal lattice vectors can be determined by

$$\vec{b_1} = \frac{2\pi}{3a}\left(1, \sqrt{3}\right) \; ; \; \vec{b_2} = \frac{2\pi}{3a}\left(1, -\sqrt{3}\right). \tag{4.1.2}$$

The two points K and K' are nonequivalent, due to the two present sublattices, and are located at

$$\begin{aligned} \mathrm{K} &= \frac{2\pi}{3\mathrm{a}}\left(1, -\sqrt{3}\right) \\ \mathrm{K'} &= \frac{2\pi}{3\mathrm{a}}\left(1, \sqrt{3}\right). \end{aligned} \tag{4.1.3}$$

Those points define most of the physical properties of graphene. The tight binding approach is suitable for calculating the band structure of the material, taking only π-orbitals and nearest and next-nearest neighbor hopping into account. The tight binding Hamiltonian reads as

$$H = -t \sum_{<i,j>,\sigma} \left(a_{\sigma,i}^{\dagger} b_{\sigma,i}^{\dagger} + H.c.\right) - t' \sum_{<i,j>,\sigma} \left(a_{\sigma,i}^{\dagger}\left(a_{\sigma,i} + b_{\sigma,i}^{\dagger}\left(b_{\sigma,i} + H.c.\right)\right)\right) \tag{4.1.4}$$

where for the chosen units $\hbar$ equals one for simplicity [120]. $a_{\sigma,i}\left(a_{\sigma,i}^{\dagger}\right)$ describe the annihilation (creation) of an electron, carrying spin s on sublattice A. For sublattice B the the
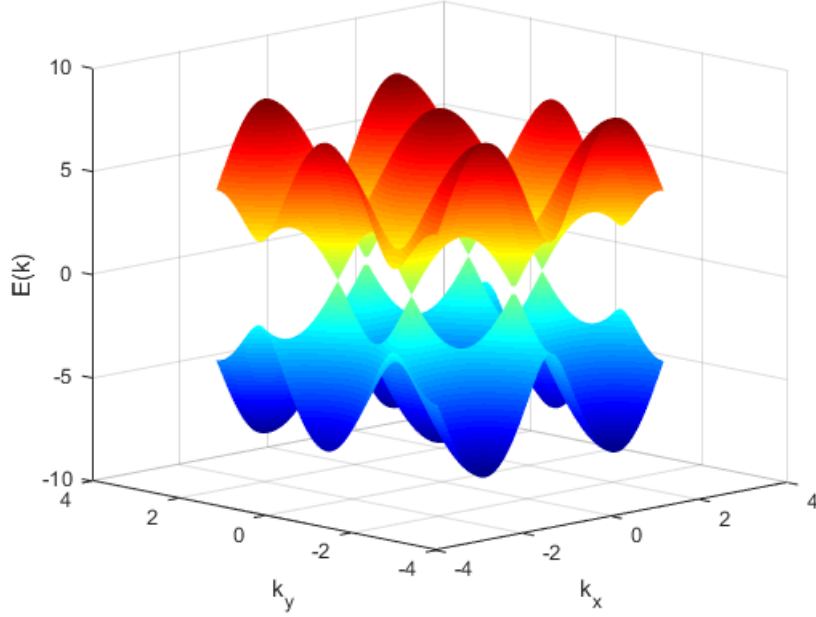
Figure 4.2: 3D representation of the bandstructure of graphene. The conduction and the valence band touch at the edges of the Brillouin zone. The image is produced via Eq. 4.1.5 using MATLAB.

annihilation (creation) of an electron is pursuant described by $b_{\sigma,i}$ $\left(b_{\sigma,i}^{\dagger}\right)$. The nearest- and next-nearest-neighbor hopping energies are described by t and t'. While hopping in between nearest neighbors requires a change of sublattice, the next nearest neighbor hopping allows the electron to remain on the original sublattice. This results in $t > t'$ with $t \approx 2.8\,\text{eV}$ and $-0.02\,\text{eV} \leqslant t' \leqslant 0.02\,\text{eV}$ [121].

This considerations result in the famous bandstructure of graphene, which is shown in Fig. 4.2. The valence and conduction bands touch at exactly one point at the corners of the first order Brillouin zone (K, K´). For undoped graphene, the Dirac point is perfectly aligned with the Fermi level, so the system is a zero-overlap semimetal. The energy bands are given by [120]:

$$
\begin{aligned}
E(\vec{k}) = \pm t_h &\sqrt{3 + 2\cos\left(\sqrt{3}k_y a\right) + 4\cos\left(\frac{\sqrt{3}}{2}k_y a\right)\cos\left(\frac{3}{2}k_x a\right)} \\
&- t_h'\left(2\cos\left(\sqrt{3}k_y a\right) + 4\cos\left(\frac{\sqrt{3}}{2}k_y a\right)\cos\left(\frac{3}{2}k_x a\right)\right).
\end{aligned}
\tag{4.1.5}
$$

Close to the K and K´ points the dispersion relation can be described by

$$
E(\vec{k}) = \pm \hbar v_f |\vec{k} - \vec{K}|
\tag{4.1.6}
$$

where the Fermi velocity is $v_f \approx 10^6 \frac{\text{m}}{\text{s}}$. Comparing to a free electron gas, where

$$
v_f = k/m = \sqrt{2e/m} \quad (\hbar = 1)
\tag{4.1.7}
$$

it gets clear, that the Fermi velocity of graphene is not dependent on the energy or momentum and the dispersion relation is essentially linear in close range around the Brillouin zone corners. These points are called Dirac points due to the linearity.

4.2 Epitaxial graphene on silicon carbon substrates
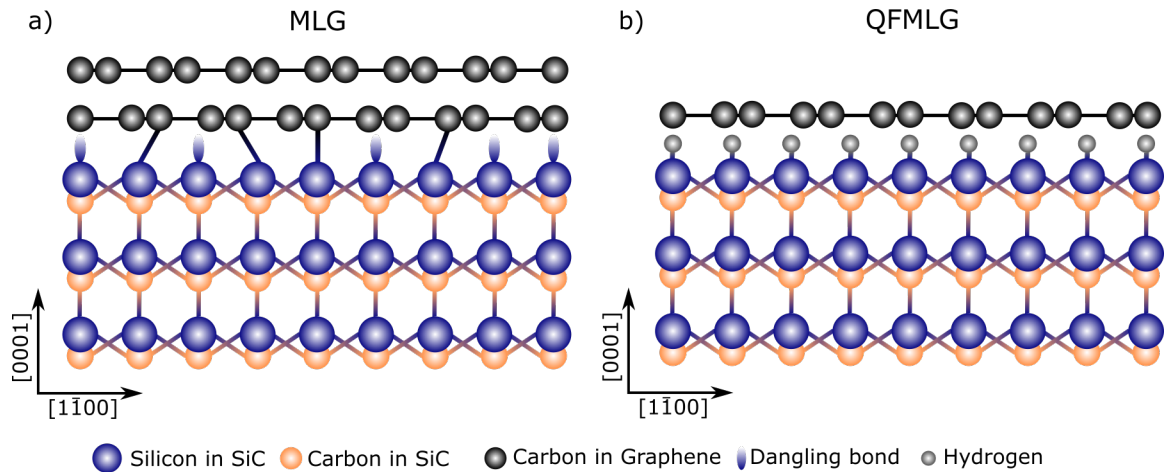
Figure 4.3: Crystal structure of a) monolayer graphene (MLG) and b) quasi-freestanding monolayer graphene (QFMLG) on the (0001=-face of a SiC substrate. In case of MLG, the buffer layer is covalently bound to the SiC substrate, the MLG is located on top of this buffer layer. In the intercalated QFMLG, the dangling bonds are saturated by hydrogen atoms.

The unconventional properties of graphene were discovered using mechanically exfoliated flakes from highly oriented pyrolytic graphite (HOPG) [25]. Several fabrication techniques for graphene were demonstrated since then, including besides exfoliation [25], the unzipping of carbon nano tubes [122] or chemical reduction of graphite oxide [123]. The two most prominent and promising methods are chemical vapour deposition (CVD) on transition metals [124–130] and thermal decomposition of SiC [131–137].

In this thesis, epitaxial graphene fabricated by the "Physikalisch-Technische Bundesanstalt" in Braunschweig, Germany [138, 139]. The thermal decomposition of SiC has been intensively studied and has shown to be a suitable approach for high quality large scale graphene convenient for electronic applications [140]. The main advantage of this approach is the direct fabrication of the graphene layer onto a semi-insulating, commercially available substrate without the requirement of transfer processes [132, 140, 141].

During annealing of SiC substrates Si is sublimated and the surface is graphitized. This method is suitable for preparation of graphene under ultra-high vacuum (UHV) conditions at typical temperatures of more than $1400\,°C$. It is possible to grow graphene from the silicon terminated $(0\,0\,0\,1)$ face as well as on the carbon terminated SiC $(0\,0\,0\,\bar{1})$ face. The growth process is the same for both faces: the Si vapor pressure is significantly higher than this of C and the Si sublimates faster at high temperatures. The remaining C atoms rearrange to a graphitic film at the surface. The graphene growth rates, growth morphology and electronic
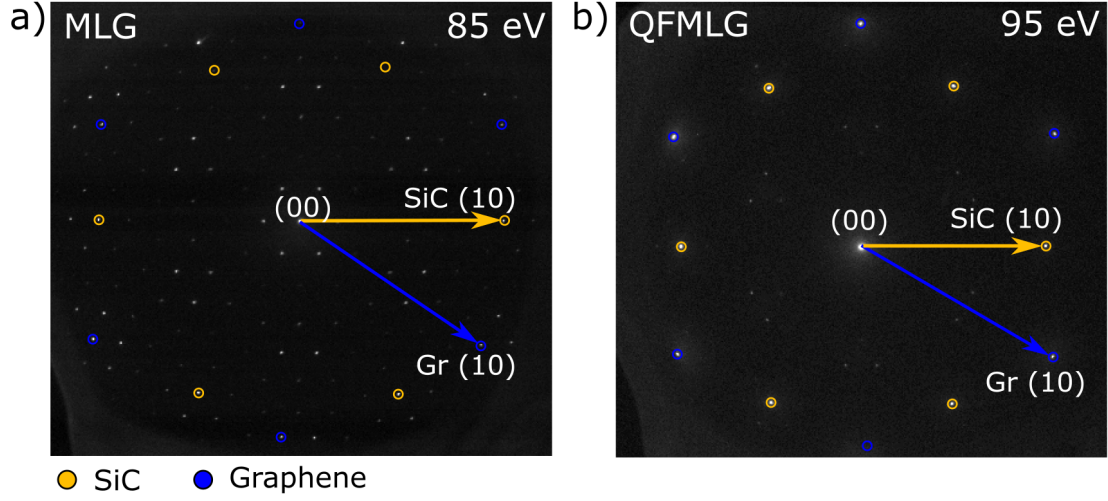
Figure 4.4: a) spot profile analysis low energy electron diffraction (SPALEED) pattern of a clean MLG sample and b) a QFMLG sample. The first order diffraction spots from graphene and the underlying SiC substrate are marked in blue and yellow, respectively. The graphene layers both reveal a $\left(6\sqrt{3} \times 6\sqrt{3}\right) R30°$ structure. Due to the complex crystal structure, besides the graphene and SiC spots, several reconstructions of the surface can be seen.

properties are different for each polar surface due to different surface reconstructions and growth kinetics [142–144].

The graphene layer is not directly grown on top of the substrate, but a rather complex buffer- or zerolayer is formed. This layer is partially sp^3 hybridized and forms covalent bonds to the underlying SiC crystal. It is therefore non-conductive and showing a band gap. The layer forms a $\left(6\sqrt{3} \times 6\sqrt{3}\right) R30°$ reconstruction with respect to the SiC, providing a template for subsequent graphene layer growth. This buffer layer forms a non-interacting interface to graphene layers on top of it, thus decoupling it from the SiC the substrate still has a significant electronic influence.

If the growth process is continued, another layer forms underneath the first one decoupling the initially grown layer from the substrate. This results in the presence of a buffer layer and a layer of MLG. Due to the decomposition process, the growth is not layer by layer on top of each other but reverse.

Charge transfer between the interface states of MLG induce an electron concentration of 1.2×10^{13} cm^{-2} [145–148] shifting the Fermi level to around 0.45 eV above the Dirac point To transform the a buffer layer into a graphene layer with improved electronic properties, intercalation of chemical species between this layer and the substrate has proven to be a suitable approach. A wide range of materials, including hydrogen [149–151], sodium [152], oxygen [153], lithium [154], silicon [155], gold [156], flourine [157] and germanium [145] has shown to be suitable for intercalation processes. The covalent bonds between the buffer layer and the SiC substrate are broken leading to an electronically decoupled QFMLG layer. Hydrogen has shown to be the most promising candidate for this purpose until now.

QFMLG is slightly p-doped so the Fermi level is shifted under the Dirac point by approx.

100 meV. The different structure of the two sample types can be observed in the diffraction patterns, exemplary SPALEED measurements are shown in Fig. 4.4. The diffraction pattern of graphene on SiC is quite complex and includes spots originating a lot of different reconstructions, which will not be explained in detail in this work. The interested reader is referred to the work of Riedl from 2010 [150]. The LEED pattern shows the characteristic $\left(6\sqrt{3} \times 6\sqrt{3}\right)$ R30° reconstruction originating from the bufferlayer [158]. The diffraction measurements do not allow to distinguish between buffer layer and monolayer graphene.

In case of hydrogen intercalation, the reconstruction spots loose and the graphene spots gain intensity. This is a strong indication for the decoupling of the interface layer from the substrate [149, 150].

## 4.3 Hydrogen adsorption on graphene

Carbon based materials have shown to be promising candidates for hydrogen storing [159–162] and vapor sensing applications [27, 163–167]. In this chapter the influence of atomic hydrogen adsorption to MLG and QFMLG with focus on the electronic transport properties is analyzed. Understanding the impact of hydrogen adsorption to the electronic properties lays the baseline for future applications based on this effects.

The results presented in this chapter are published under "Strong localization in weakly disordered epitaxial graphene" by D. Slawig et al. in Surface Science 707 (2021) [168].

4.3.1 Adsorption of atomic hydrogen

The delocalized electron system found in graphene mimics a two dimensional, relativistic electron gas. Point defects like hydrogen atoms, induce a local change from sp^2-hybridized orbitals to sp^3-hybridization. This effect does not only introduce scattering centers but also breaks the sublattice symmetry. This distortion of the honeycomb lattice is accompanied by a gap opening around the Dirac point E$_D$ and ordering of spin states around the H atom [169–171].

The electronic gap is defined by the coverage of hydrogen and large gaps can be opened by a very low amount of adsorbed hydrogen as schematically shown in Fig. 4.5, this plot is based on data collected from several studies, working experimentally with STM/STS [162] and angle-resolved photoemission spectroscopy (ARPES) [170, 172] or theoretically [173–176]. Rossi et al. [177] came up with a empirically found universal correlation between gap energy E$_{gap}$ and H coverage Θ: E$_{gap}$ = 3.8 eV $\cdot$ (Θ/100%)$^{0.6}$. The correlation becomes evident when comparing with the other result in Fig. 4.5. The adsorption process is quite complex and requires well defined starting conditions. There is a wide variety of studies performed on this topic, including measurement techniques like STM and ARPES [162, 172, 178, 179]. Different sticking coefficients were reported for hydrogen on graphene and/or graphite, differing by several orders of magnitude, from 1 to 10^{-4} [180–182]. The sticking is highly dependent on the quality of the graphene samples, high quality surfaces show an improved sticking probability. The chemisorption process is coupled to a steric effect. The formation of sp^3-bonds between graphene and a hydrogen atom requires a tetrahedron angle of 109.5°. Starting from a flat graphene surface, this requires the puckering of a carbon atom, shifting its atomic position by 0.1 nm out of the graphene plane [183]. This leads to an adsorption energy of 0.2 - 0.3 eV
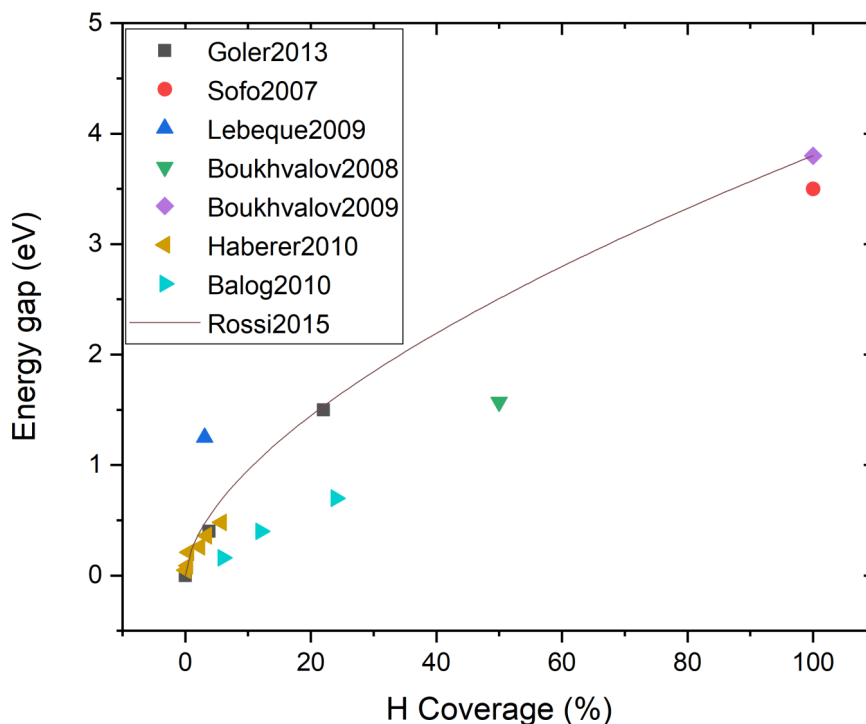
Figure 4.5: The bandgap at the Dirac point in dependence of the hydrogen coverage on a graphene sample is shown. The data points are collected from several studies as referenced in the legend [162, 170, 172–177].

[181, 184] for planar graphene. Contrary the adsorption of H on MLG reveals a considerably lower energy of 0.05 eV for the first atom, which is even vanishing for the second H atom and the formation of a dimer structure [162]. From theoretical investigations it is obvious, that the ortho-position for a second hydrogen is energetically not favorable, thus the p_z-state of every second C-atom is on average saturated by a H atom [184].

The reconstruction of the buffer layer modulates the graphene layer. As proven by scanning tunnelling microscope (STM), the convexly curved parts of the MLG structure provide preferential adsorption sites [162, 177], because the binding angle is already present and no puckering of carbon atoms is needed. Two main factors determining the adsorption energy become apparent from calculations: first the formation of the C-H bond and second the distortion of the carbon lattice and the correlated charge redistribution.

There is a maximum surface coverage of 0.4 ML predicted by theory. Still, the existence of graphane - fully hydrogen saturated graphene sheets - were anticipated by calculations and proven by experiment [25, 176, 185].

In this work, the low coverage regime is investigated. An extraordinary change of the electronic properties is induced in the material by hydrogen coverages below 1 % and is therefore of high interest. This adsorption regime is not examined by surface transport so far.

The experiments containing atomic hydrogen were performed using a thermal cracker (MBE components), hosted in the preparation chamber of the four-point probe (4pp)-STM. A cracking efficiency of 40 % is achieved for filament temperatures of 1700 °C. The partial H_2

pressure used for the adsorption was set to 1×10^{-7} mbar. According to manufacturer specifications the loss of H atoms due to recombination in our setup is approx. 90% caused by the distance in between the cracker outlet and the sample of 12 cm [186–188]. This results in a an exposure of the sample surface to a dose of about 0.25 Langmuir/min of atomic H. The wide range of reported sticking coefficients as mentioned above, does not allow a direct calculation of coverage from the dosage. In accordance with our experimental results regarding localization lengths and mean free path a sticking coefficient of $8 \pm 2 \times 10^{-4}$ is deduced. This results in an adsorption rate of $\approx 3 \times 10^{-6}$ ML/min. The relative coverages are given in monolayers (ML) with respect to C-atom density (3.8×10^{15} cm^{-2}). All adsorptions were performed at a substrate temperature of 300 K.

Heating of the sample to 920 K is found to lead to complete desorption of the hydrogen, restoring the electronic properties of the clean graphene sample. The sample is heated before every adsorption to assure a clean surface without residuals. For the coverage dependent transport measurements the sample was transferred in-situ at 300 K. Atomic hydrogen is expected to act as an acceptor. Assuming, that one electron from graphene is transferred to the chemical bond, in case of MLG at least a concentration in the order of 10^{13} cm^{-2} H$^+$ ions, equivalent to 0.0025 ML, or 0.25 % ML, is needed to shift the Fermi energy to the Dirac point. As shown above, the investigated coverage regime is lower by at least one order of magnitude. Moreover, due to recombination inside the hydrogen cracker, most of the beam will consist of neutral H-atoms [186]. This means the shift of the electrochemical potential is even smaller.

The sticking coefficients for hydrogen adsorption on MLG and QFMLG are quite similar. Therefore, although the coverage may differ by a factor of two, the Fermi level is shifted in both sample types roughly by the same amount. As QFMLG is in fact slightly p-doped, again the Fermi level will not coincide with E$_D$. Based on this assumption, the lift of the honeycomb lattice symmetry and concomitant gap opening at E$_D$, as discussed in context of Fig. 4.5, is excluded to be responsible for the electronic transport. This is in line with ARPES measurements on MLG, showing extended Fermi surfaces for comparable H coverages [189].

4.3.2 Structural analysis

The structural influence of H adsorption on MLG was investigated by high resolution SPALEED. For reference a diffraction pattern of clean MLG has been obtained (see Fig. 4.4). The surface was exposed to various dosages of atomic hydrogen at room temperature. At this temperature, the barrier for intercalation can not be overcome by the hydrogen atoms, thus only adsorption to graphene at the vacuum interface takes place. Diffraction measurements show no structural changes for hydrogen terminated surfaces within the low coverage regime. Compared to the diffraction pattern of clean MLG, as shown in Fig. 4.6 a). The diffraction pattern is not changed for the hydrogen exposed sampled, as shown in Fig. 4.6 b). The diffraction peaks are not broadened, but the background intensity is increased upon hydrogen adsorption, as shown in Fig. 4.6 c). This is expected for uncorrelated defects at the surface [190]. The coverage of less than 1% ML is not expected to change the structural properties of the sample. For high hydrogen coverages, an increased lattice constant by up to 2% was observed [191]. This effect was not seen in the SPALEED measurement, underlining the
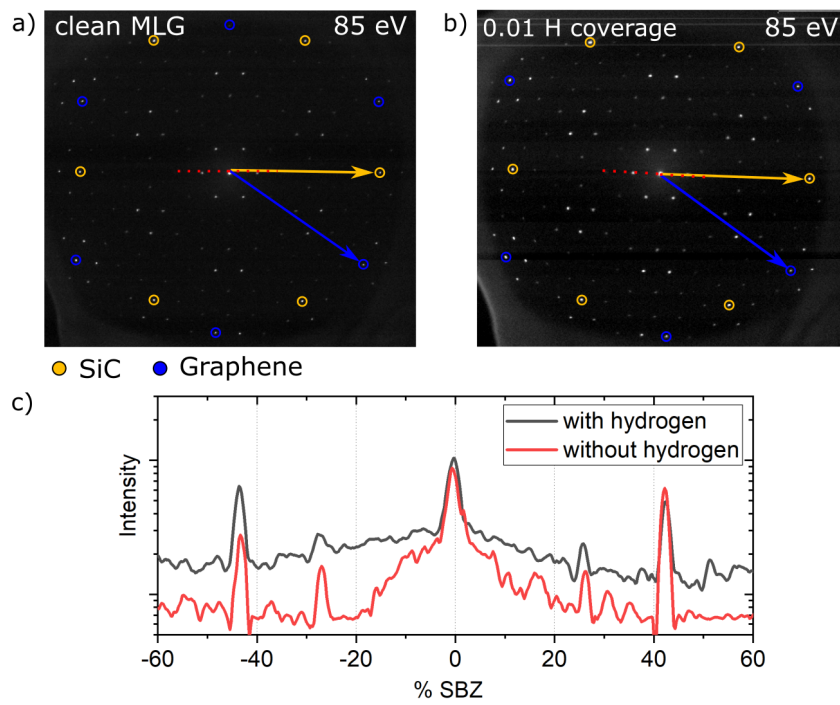
Figure 4.6: a) SPALEED pattern of a clean MLG sample and b) a hydrogen terminated sample The first order diffraction spots from graphene and the underlying SiC substrate are marked in blue and yellow, respectively. Besides the graphene and SiC spots, several reconstructions of the surface can be seen. No structural differences were observed in the measurements. This is underlined by linescans, shown in c), which were taken along the red dotted lines in a) and b). While the FWHM remains almost unchanged, the background increases, indicating the presence of defects at the surface.
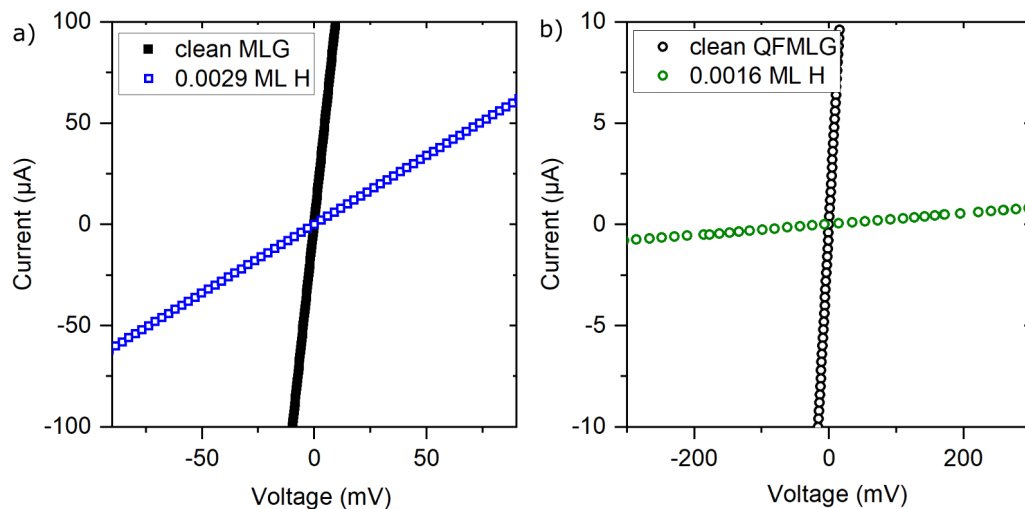
Figure 4.7: a) I-V curves of clean (black) and H-terminated MLG (blue) and measurements for clean (black) and hydrogen terminated (green) OFMLG All measurements were performed at 300K.

achieved low coverages.

Despite the absence of structural changes in the low coverage regime, hydrogen adsorption on carbon surfaces is known to have a high impact on the electronic transport properties.

4.3.3 Electrical transport measurements

I-V measurements on both sample types, MLG and QFMLG, reveal a linear characteristic as shown in Fig. 6.6, indicating the expected metallic behavior. The sheet resistance R_s for clean MLG is determined to be approx. $0.5\,k\Omega/\square$. This is in nice accordance with former studies [139]. The resistance value for QFMLG is initially higher and determined to approx. $14\,k\Omega/\square$. A completely decoupled layer is expected to show lower resistivity values than a MLG layer, because the electrochemical potential is closer to the Dirac point, which is accompanied by higher charge mobility [192]. Although at the Dirac point the density of states is lowered and no conductance exists. The resistivity indicates incomplete intercalation of the used sample with remaining fractions of buffer layer. The intercalated areas are percolated and the 2D behavior is obtained as revealed by tip distance dependent measurements [58]. The linear characteristic of the I-V curves is preserved upon hydrogen adsorption for both samples, as shown in Fig. 6.6. During hydrogen adsorption the sp^2-hybridization of graphene is locally changed to a sp^3-type bonding. The distortion of the lattice induces a change of the electron density, which acts as scattering center for propagating electrons, as described in Sec. 4.3.1. This effect increases the resistivity.

The sheet resistance R_s was found to increase for both sample types, MLG and QFMLG. As shown in Fig. 4.8, R_s increases by several orders of magnitude upon adsorption, even though the coverages are very low. This metal-insulator transition (MIT) is in agreement with SPALEED revealing reconstruction spots characteristic for a buffer-layer (cf. Fig.4.4 b). A closer look to Fig. 4.8 shows, almost the same time constant τ on the resistance increase for
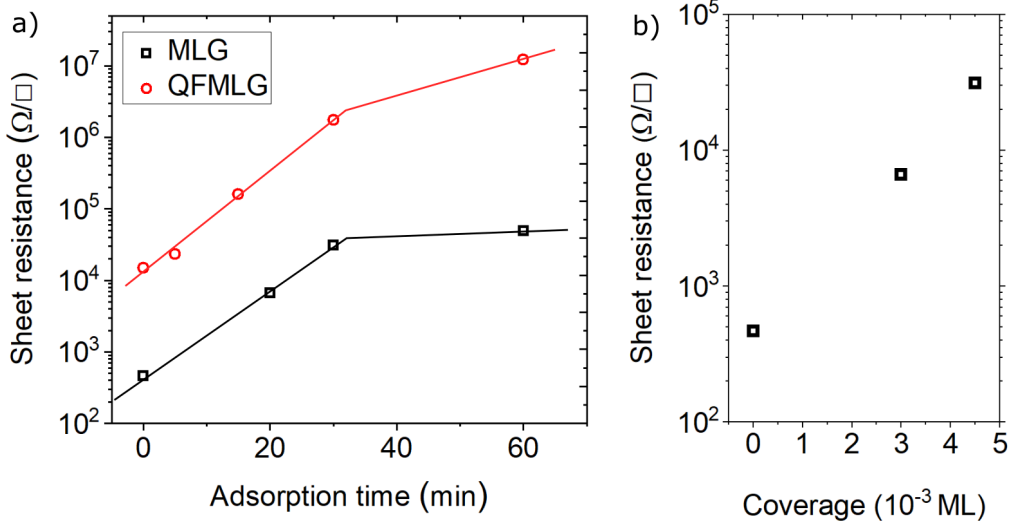
Figure 4.8: a) Sheet resistance as a function of H coverage for MLG (black) and QFMLG (red) measured at 300 K. The resistance is increased upon hydrogenation in both cases. Compared to the QFMLG sample, in case of MLG saturation is reached after approx. 30 min at a resistivity of 50 kΩ. b) Shows the resistivity increase as a function of coverage for the MLG sample.

MLG and QFMLG in the low coverage regime ($\tau_{\mathrm{MLG}} \approx 450$ s, $\tau_{\mathrm{QFMLG}} \approx 1000$ s). Slightly different sticking coefficients might explain the difference of a factor 2 in the time constants. In case of MLG the corrugation due to interaction with the buffer layer creates preferred adsorption sites for hydrogen in the low coverage regime [162]. On these preferred adsorption sites, chemisorption can take place without energy barriers, this is not the case for QFMLG. Higher hydrogen coverages were shown for p-type graphene samples by gating dependent hydrogenation experiments [193]. The coverages on MLG and QFMLG are expected to be very similar and the different chemical potentials do not seem to be the driving force for the different time scales.

The exponential increase of the resistance with increasing number of chemisorbed H atoms n_{H}, is described by $R \propto \exp L/L_0$, and indicates localization in the system. The effect of localization is explained in more detail in Sec. 2.3. In this scenario the mean-free path L_0 decreases upon adsorption, for measurements with fixed probe spacing L. The mean-free path for the electrons is in this case expected to be inversely proportional to the number of chemisorbed H atoms $L_0 \propto 1/\sqrt{n_{\mathrm{H}}}$. This includes the assumption of homogeneous adsorption on the surface. For the MLG sample, a clear plateau is reached at a coverage of approx. 5×10^{-3} ML. The transition is not as clear for the QFMLG sample.

Within the picture of Drude band conduction, the resistance is expected to follow $R \propto 1/L_0 \propto \sqrt{n_{\mathrm{H}}}$, where n_{H} is the concentration of H atoms. This correlation does not explain the exponential increase in resistance. This exponential increase is a hallmark for localization within 2D systems. It indicates that the phase coherence lengths L_Φ exceeds L_0. The measurements are performed at a temperature of 300 K, coming along with the limitation that only energy barriers below $2k_{\mathrm{B}}T \approx 50$ meV can be probed by transport. Although the
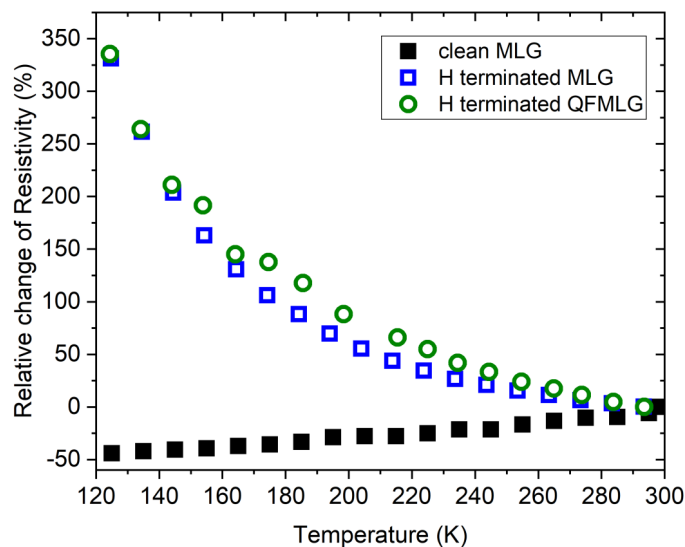
Figure 4.9: Relative change of the resistivity as a function of temperature. The clean MLG sample shows an increase of the resistivity with increasing temperature (back squares), while for H-terminated MLG and QFMLG surfaces the resistivity decreases (blue open squares and green open circles, respectively). The H-coverages for MLG and QFMLG were 0.0029 ML and 0.0006 ML, respectively.

H coverage further increases, its effect cannot directly be examined. To gain further inside into the transport behavior, temperature dependent measurements were performed. All adsorption processes were done at 300 K before cooling the sample, realizing different coverages in a reproducible way. Measurements were performed for a temperature range from 120 to 300 K, keeping the surface coverage constant during cooling.

The resistivity strongly increases with decreasing temperature for both sample types, as shown in Fig. 4.9 for exemplary H coverages. For comparison the temperature dependent resistivity of clean MLG is shown, where the resistivity decreases with decreasing temperature because of remote phonon-electron scattering [194].

4.3.4 Temperature dependence

The electrical measurements indicates, that hydrogenated graphene shows a behavior comparable to defective MLG. This comparison indicates variable range hopping (VRH) as the dominant transport mechanism [194]. During adsorption VRH replaces the metallic transport originating from the initial clean graphene layer. This behavior is an indication for activated transport. This is caused by the chemisorption of hydrogen and the concomitant change of electronic structure within the layer.

The concept of Anderson localization, as described in Sec. 2.3.1 can be used to describe this behavior. Although this model is used to describes strongly disordered systems, it is possible to provide a description of the measured phenomena. The resistivity within this framework given by Eq. 2.3.11 and determined by

$$R_{Sheet} \propto exp(T_0(\xi)T)^{1/(d+1)}, \tag{4.3.1}$$
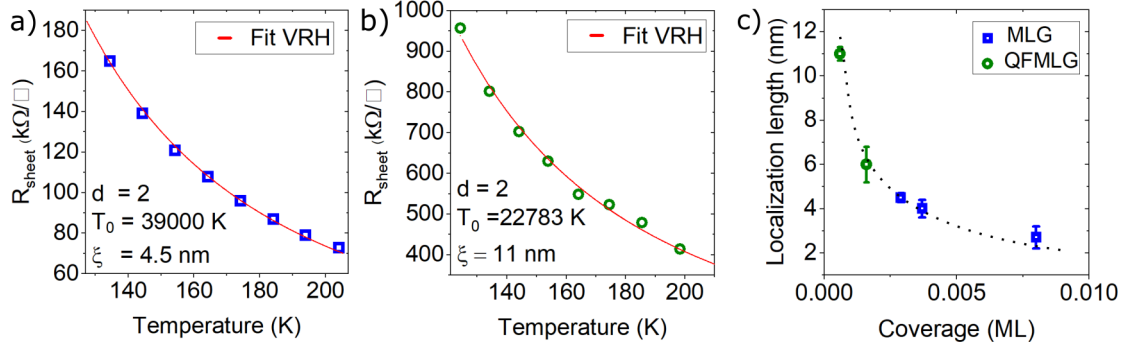
Figure 4.10: Sheet resistance R_S in dependence of the temperature for a) 0.0029 ML H on MLG and b) 0.0006 ML H on QFMLG. The fit corresponding to the variable range hopping model is marked by solid lines. The fit results for the parameters of the Anderson model, namely the dimension d, the Anderson temperature T_0 and the localization length ξ are shown in the panels. c) Localization length for different hydrogen coverages on MLG and QFMLG. The mean free path L_0 is indicated by the dotted line and fits nicely to the determined localization lengths.

where d denotes the dimension and $T_0(\xi)$ the Anderson temperature, which can be calculated according to Eq. 2.3.12[74, 195] and depends on the localization length ξ and the density of states at the Fermi energy $D(E_F)$. $D(E_F)$ is around $D(E_F) \approx 2 \times 10^{13}$ cm^{-2}eV^{-1} for MLG and $D(E_F) \approx 5 \times 10^{-12}$ cm^{-2}eV^{-1} for QFMLG [196, 197].

The residual contribution of the phonon-assisted transport channel destroys the phase coherence within the 2D electron gas system. To obtain a consistent picture, data points measured at temperatures higher than 200 K were excluded, to eliminate this residuals. The fitting results within the framework of this model are shown in Fig. 4.10 a) and b) for MLG and QFMLG, respectively.

For both systems, hydrogenated MLG and QFMLG, the dimensionality d is 2. This is independent from the hydrogen coverage probed within this study, underlining the preservation of the two dimensional character of graphene. Contrary, higher hydrogen coverages cause an increase of the Anderson temperature T_0. The corresponding localization length is therefore reduced upon adsorption, as shown in Fig. 4.10 c). The mean free path is found to scale nicely with the determined localization length $\xi \propto L'_0$. The mean free path lengths can be parameterized as $L'_0 \propto /1\sqrt{\alpha n_H}$, where the factor α describes the tendency of H to form dimers on graphene surfaces. The cluster density is therefore lower than the H atom density, the best agreements was obtained for $\alpha = 0.3 \ldots 0.5$. This finding fits to the expected dimer formation of H atoms on graphene surfaces.

For example, a coverage of 0.0029 ML refers to a density of 2×10^{12} cm^{-2} H-clusters. This corresponds to the occupation of every third (6×6) site with a separation of 4.5 nm. This, in turn correlates with the localization length.

The graphene lattice remains rather intact, as shown by diffraction measurements, and the wave function becomes localized in between the hydrogenated parts of graphene

$$|\Psi(r)| \propto \exp(|r - r_0|/\xi). \tag{4.3.2}$$
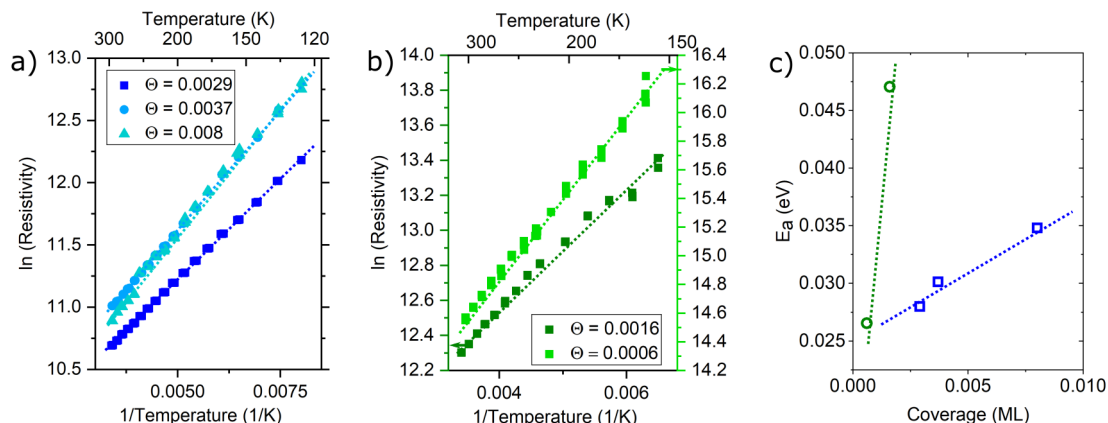
Figure 4.11: Arrhenius plots of hydrogen terminated MLG a) and QFMLG b) for different H-coverages. In this visualization the activation energy is proportional to the slope of the curves. c) Deduced activation energy E_a deduced from the data sets shown in a) and b). The dashed lines are guides to the eyes.

In turn, the hydrogenated graphene system resembles the condition of weak disorder and fulfills the Ioffe-Regel criterion [72]. For MLG with $E_F \approx 0.5\,\mathrm{eV}$ and $v_F = 1 \times 10^6\,\mathrm{ms}^{-1}$, the Fermi wavelengths $\lambda_F = hv_F/E_F \approx 8\,\mathrm{nm}$. H adsorption at the preferred convexly curved sites of the (6x6) reconstruction introduces scattering centers of much smaller separation lengths than the Fermi wavelength of the electrons, and is therefore violating the Ioffe-Regel criterion. Chemisorption leads to a concomitant charge transfer from the graphene substrate to the C-H bonds and the π-bands are renormalized, as seen in ARPES. Those effects are additionally amplifying the localization effect. The Fermi wavelength is even larger for almost charge neutral QFMLG.

In order to determine an average activation energy E_a to overcome phase coherence and therefore discriminate localization of electronic states, we performed an Arrhenius analysis. The activation energy can be determined by

$$R \propto \exp(E_a/k_B T). \tag{4.3.3}$$

As seen in Fig. 4.11, the activation energy is around $E_a \approx 30\,\mathrm{meV}$ in the low coverage regime and increases with increasing H-coverage. Although the adsorption of H on MLG and QFMLG transforms the metallic system in well defined insulating states, the resistivity behavior for a fixed H-coverage is well described with one activation energy over a wide a temperature range. In detail, for H-terminated MLG the activation energy varies between $28\,\mathrm{meV}$ and $35\,\mathrm{meV}$ for coverages ranging from 0.0006 to 0.008 ML. A similar behavior was found for QFMLG, where the activation energies range from $26\,\mathrm{meV}$ to $48\,\mathrm{meV}$ for a coverage of 0.0006 ML und 0.0016 ML, respectively. This means in first approximation, with regard to measurement uncertainties, the activation energies are independent from the used type of graphene. The determined activation energies are not corresponding to an actual gap opening at the Dirac point. Due to the internal doping of the graphene samples, this would not be possible to determine via electronic transport. The analyzed energies rather describe a loose of phase coherence.

In ARPES measurements performed in former studies, the π states of the clean system strongly renormalizes and give rise to what in this context is designated as a quasiparticle transformation [189]. Apparently, cooperative effects start to play an important role and increase the phase coherence.

4.3.5 Conclusion

The chemisorption of atomic hydrogen to graphene samples introduces scattering centers and breaks the sublattice symmetry, resulting in an electronic band gap at the Dirac point. The adsorption process was analyzed using two different types of graphene samples, MLG and QFMLG. A MIT transition was induced by chemisorption of small hydrogen concentration below 1 % of an monolayer. The metallic transport behavior originating from the clean graphene layer was replaced by VRH transport upon hydrogenation. This transition was observed by temperature dependent measurements with surface coverages of up to 0.008 ML of atomic hydrogen.

During the adsorption of hydrogen the sublattice symmetry of the graphene lattice is broken, introducing an electronic band gap of approx. 1eV [170, 172]. This band gap opening was proven by scanning tunnelling spectroscopy (STS) and is increasing with higher H coverages [162, 169]. Data recorded on the hydrogen clusters, indicates that the hydrogen covered parts of the samples are charge neutral. This means electronic hopping or tunneling across these areas is very unlikely.

The Anderson model can be successfully applied within the limit of weak disorder, although the system is not heavily disordered. The localization length and the mean free path coincide nicely. The selective chemisorption of H and the cluster formation act as scattering centers and in turn determine the mean free path.

For temperatures, below 200 K, the phase coherence length exceeds the mean free path and constructive interference of the charge carriers occurs, according to the Ioffe-Regel criterion. Based on former studies, the hopping and tunneling transport across or around these charge neutral hydrogen covered areas can be excluded as very unlikely. Thus, the Anderson model can be applied in the limit of weak disorder. The determined localization lengths coincide nicely with the mean free paths, which are determined by the coverage and the concomitant clustering of hydrogen.

At low temperatures, the charge carriers constructively interfere according to the Ioffe-Regel criterion. The activation energies, determined via Arrhenius analysis, for this MIT do not refer to the band gap opening on the Dirac point but to a breakage of phase coherence. An ordinary band insulator is therefore excluded.

4.4 Organic molecules on hydrogenated graphene: PbPc adsorption

Combining organic molecules and graphene is a promising approach for realizing new functional materials and sensor approaches [27, 163, 165, 173, 198]. The adsorption of molecules to graphitic substrates was of high interest during the last years [199–203]. A wide range of phenomena were investigated, ranging from large interactions, like the opening of a bandgap introduced e.g. by perylenetetracarboxylic diimide (PTCDI) to very weak coupled molecular layers, e.g. perylenetetracarboxylic dianhydride (PTCDA) [204]. The flexibility and tailoring possibilities of organic molecules open a large playground for functionalized materials.
Graphene based sensors thereby arouse a lot of interest [163, 165, 173, 198, 205–207]. Detecting charge transfer by less than one electron by electrical conductivity measurements at room temperature were reported [27], producing extraordinary sensitivity factors. Taguchi realized one of the first gas sensors, using SNO_2, in 1972 [208]. The sensitivity of chemical detectory relying on gas-solid surface reactions is often limited by the sintering process and the dense network of grain boundaries arising from the nanoparticle sizes. A chemical modification of those particles, e.g. oxidization or reduction induces an increase or decrease of conductance. While the first sensors were designed for detection of petroleum gas [209], their concepts were sucessfully extended to a wide range of other materials, including hydrogen [206].
Reaction barriers limit the sensitivity of these sensor concepts additionally, requiring elevated temperatures or the addition of metals. 2D graphene provides the highest surface to volume ratio and highly mobile low-noise charge carriers. Resistivity measurements capture changes in the carrier concentration as well as in charge carrier mobility thanks to the transport properties governed by the electronic bands. This makes graphene a highly promising candidate for sensor approaches.
Designing a sensor approach with molecules on graphene is rather challenging, despite the high potential sensitivity pf graphene it is not selective to molecules. This difficulty can be overcome by functionalization of graphene, although this often comes along with cutbacks of the exceptional properties of pristine graphene [198, 210, 211]. The interplay of PbPc molecules and chemisorbed hydrogen is investigated by surface transport and density functional theory (DFT). DFT calculations were performed by U. Gerstman working at the university of Paderborn. Transport investigation were performed by means of 4pp-STM.
The results presented in this chapter are submitted to be published under "Adsorption and reaction of PbPc on hydrogenated epitaxial graphene" in the Journal of Physical Chemistry C.

4.4.1 PbPc on graphene

Pthalocyanine molecules are of great interest because of their flexibility and functionalizability. The central core atom can be varied in size and charge, allowing to tailor the shape and the magnetic state of the molecule. Molecular storage concepts were investigated and there are proof of principle studies [212, 213].
    In this work, PbPc molecules were used. The structure of this molecule is depicted in Fig. 4.12. The central Pb atom is large compared to the cavity in an H_2Pc molecule. This causes a shuttlecock configuration as shown in the side view in Fig. 4.12 b). This configura-
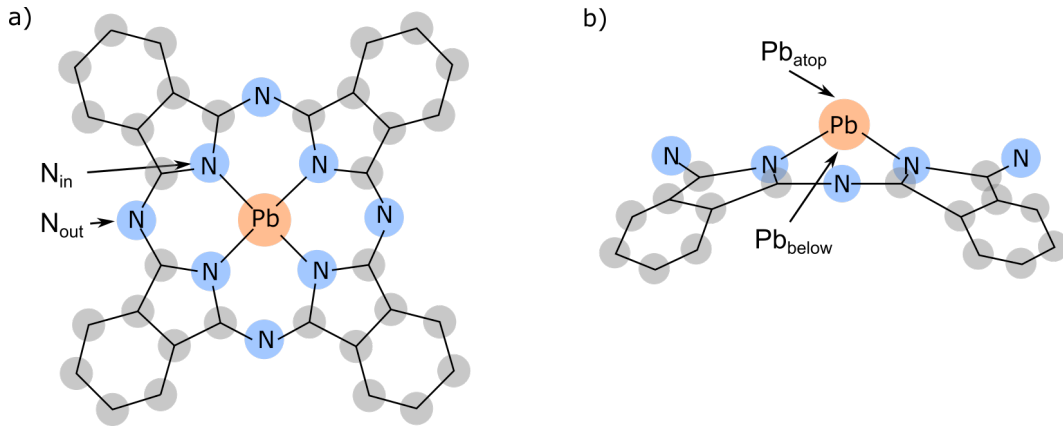
Figure 4.12: Strucutre of a PbPc molecules in a) top view and b) side view. Carbon atoms are shown in grey, nitrogen in blue and lead in orange. The side view pictures the typical shuttle cock configuration. Possible adsorption sites (N_in, N_out, Pb_atop and Pb_base) are indicated.

tion can be switched from top to bottom with an energy barrier of 4.3 eV [214].

The adsorption of PbPc on clean MLG surfaces was studied in previous work, e.g. by Nguyen et. al. [213, 215, 216]. As shown by STM studies, the adsorption of PbPc molecules on graphene surfaces results in highly ordered monolayer structures, with the Pb-atom pointing upwards. Because of the high energy barrier thermally activated switching is very unlikely. On graphene, the upward orientation of the Pb atom is energetically favored by at least 0.3 eV compared to the downward direction [217] and indicates the absence of a strong hybridization in between the molecular core and the underlying graphene [215].

All adsorption processes are performed under UHV conditions at a substrate temperature of 300 K. Thermal evaporation at 540 K from a Knudsen cell was used for organic beam epitaxy. The coverage of PbPc molecules is given in regard to a physical monolayer of flat-lying molecules. scanning electron microscope (SEM) images show the presence of PbPc molecules and provide a reasonable measure for the coverage as shown in Fig. 4.13. The black contrast represents the flat-lying molecules within a densely packed structure [215]. It was shown that the coupling between PbPc molecules and epitaxial graphene is very weak. Therefore, a high mobility of the molecules is expected at room temperature [218, 219]. Based on this assumption, the black contrast stems from nucleated molecules. PbPc has a large highest occupied molecular orbital (HOMO) lowest unoccupied molecular orbital (LUMO) gap and the secondary electron signal detected by the SEM is accordingly low. The molecules form islands in the vicinity of steps or other defects. A closer look to Fig. 4.13 b) reveals islands forming along the [$11\bar{2}0$] direction of the 6H-SiC wafers and are elongated along the step edges. The islands are formed by densely packed layers as observed in STM and shown in Fig. 4.13 c) [215].

From an electronic point of view, highly mobile molecules can be described as a 2D gas at the surface which is in equilibrium with those islands. Only the nucleated molecules can be visualized via SEM, but it is still a reasonable way of estimating the surface coverage. The relative change of resistivity upon PbPc adsorption is shown in Fig. 4.14 a). A small increase of about 4 % with every adsorption step is observed.
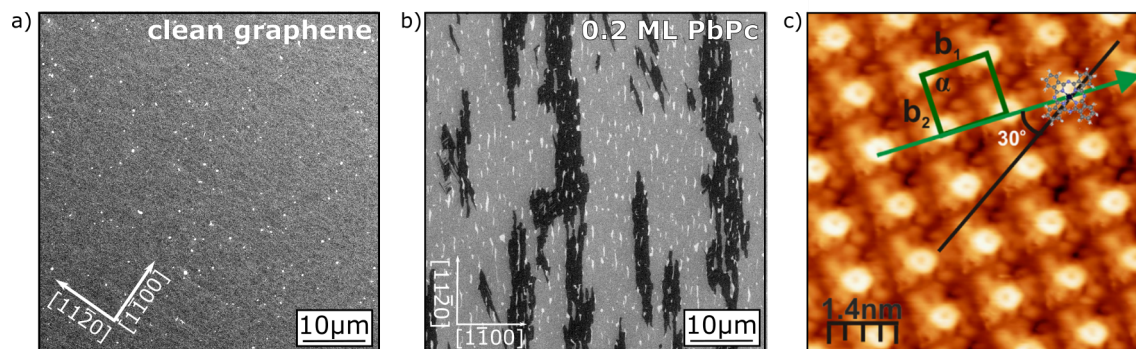
Figure 4.13: a) SEM image of clean MLG. The white spots refer to bilayer graphene. The overall secondary electron contrast is quite uniform and demonstrates a homogenious and percolated growth of graphene. b) SEM image of MLG with 0.2 ML PbPc. The dark contrast corresponds to islands of PbPc molecules and reflects the insulating state of PbPc. c) STM image ($V = -1\,V, I = 100\,pA, T = 77\,K$) of PbPc on pristine graphene. The unit cell of the well ordered structure is marked in green (Figure from [215]).

Former STS studies show the density of states of the adsorbed molecules and reveal no electronic states at the Fermi energy, indicating the molecules do not contribute to the electronic transport. The STS data shows no strong shifts in the molecular states, ruling out a charge transfer scenario [215]. The coupling between the PbPc molecules and the graphene surface is noninvasive and does not result in a change of electronic transport properties of the material. The resistance increase can apparently be explained by degradation of the PbPc layer due to the SEM electron beam during the tip positioning process. Irradiation dependent measurements show an increase of resistance with increasing beam exposure time. This is a strong indication for e-beam induced damages of the molecular layer [215, 220, 221]. More details of this degradation effect in this specific system, along with coverage, exposure time and beam energy dependent measurements are reported in the work of Nhung et.al. from 2019 [215]. For the used acceleration voltage of $15\,kV$ and a probe current of $1\,nA$, an increase of resistance of $2.5\,\Omega\square\,/\,min$ is expected. A tip positioning time in the range of $1\,min$ is estimated for the presented measurements. Based on this assumptions, the measured increase matches the expectation very well.

The corresponding I-V measurements are shown in Fig. 4.14 b). The characteristics are strictly linear for all measured coverages, as exemplary shown for $0.07\,ML$ and $0.47\,ML$ indicating the ohmic transport behavior is preserved upon adsorption.

4.4.2 Co-adsorption experiments: H and PbPc on graphene

As shown in Sec. 4.3.1, the effect of hydrogen adsorption towards graphene is very strong even for sub-monolayer coverages. Ultra low coverages of only half a percent of a monolayer induce an increase of resistivity by two orders of magnitude. This large effect, arouses interest in co-adsorption experiments.

PbPc molecules were evaporated onto pre-hydrogenated MLG. Thereby different hydrogen coverages, in between $0.0014\,ML$ and $0.0033\,ML$, were used for the preoccupancy. The results
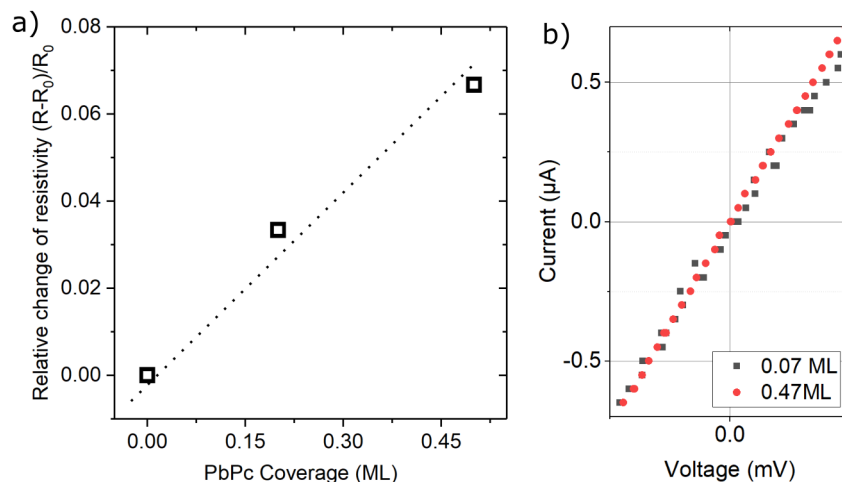
Figure 4.14: a) Relative change of resistivity of graphene with increasing surface coverage of PbPc. A small increase of about 4 % is seen for every adsorption step. b) IV measurement corresponding to different PbPc coverages of 0.07 ML and 0.47 ML. The characteristic remains strictly linear, indicating an ohmic behavior.

for three different initial hydrogen coverages are shown in Fig. 4.15. The data is corrected by the effect SEM induced molecular fragmentation, the value R_0 determines the resistivity of the clean MLG sample which is determined to $680\,\Omega/\square$. The resistivity of the hydrogenated graphene sample drops by orders of magnitude upon adsorption of PbPc molecules and reaches the values of clean graphene. The effect of chemisorption of hydrogen to graphene is completely annihilated.

The resistivity drops exponentially before reaching the value for clean graphene R_0 after adsorption of $\approx 0.1\,\text{ML}$ of PbPc. The adsorption rate is $0.15\,\text{ML/min}$ and is kept the same for the different hydrogen pre-occupancies. Transport measurements can not be performed during the adsorption and require sample transfer due to experimental limitations. Thanks to the constant adsorption rate, the measurements refer to the same time scale. All preparation and transfer steps were done in the same manner for all measurements, so the data can be analyzed with regard to their time performance. Apparent decay times can be determined as shown in Fig. 4.16 a). This allows a qualitative discussion of the results based on comparison of the three data sets.

The apparent decay times τ represent an upper limit and are in the order of $100\,\text{s}$. The time turns out to play a larger role than the coverage itself. If it is assumed, that every PbPc molecules is able to release one hydrogen atom from the graphene layer, a similar density of hydrogen and PbPc is expected. From literature, where the diffusivity for CuPc is determined to $10^{-10}\,\text{cm}^2/\text{s}$ [222, 223], it is known that high mobilities of the molecules on graphene are expected at room temperature. Based on such values, the decay times are expected to be significantly smaller. This is an indication for a small number of mobile molecules on the surface and a very efficient annihilation process.

The I-V characteristics remain strictly linear during the whole adsorption process, indicating
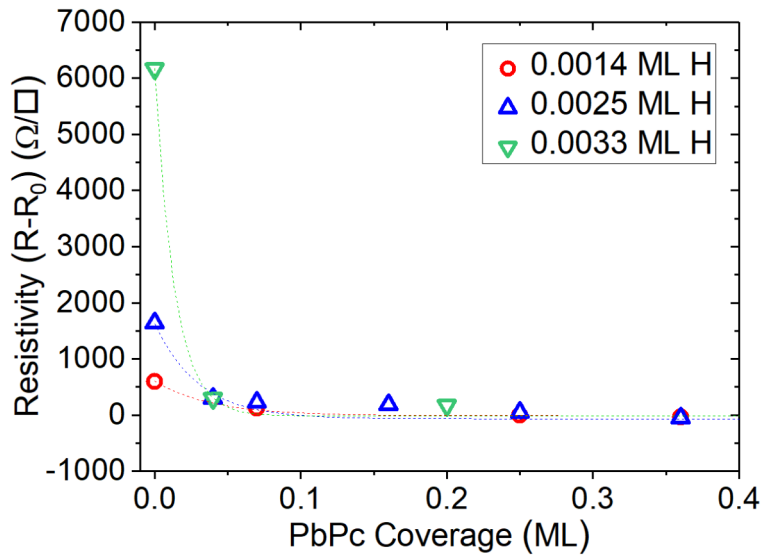
Figure 4.15: Resistivity upon PbPc adsorption on pre-hydrogenated MLG with different pre-occupancys. R_0 determines the resistivity of the clean MLG substrate.
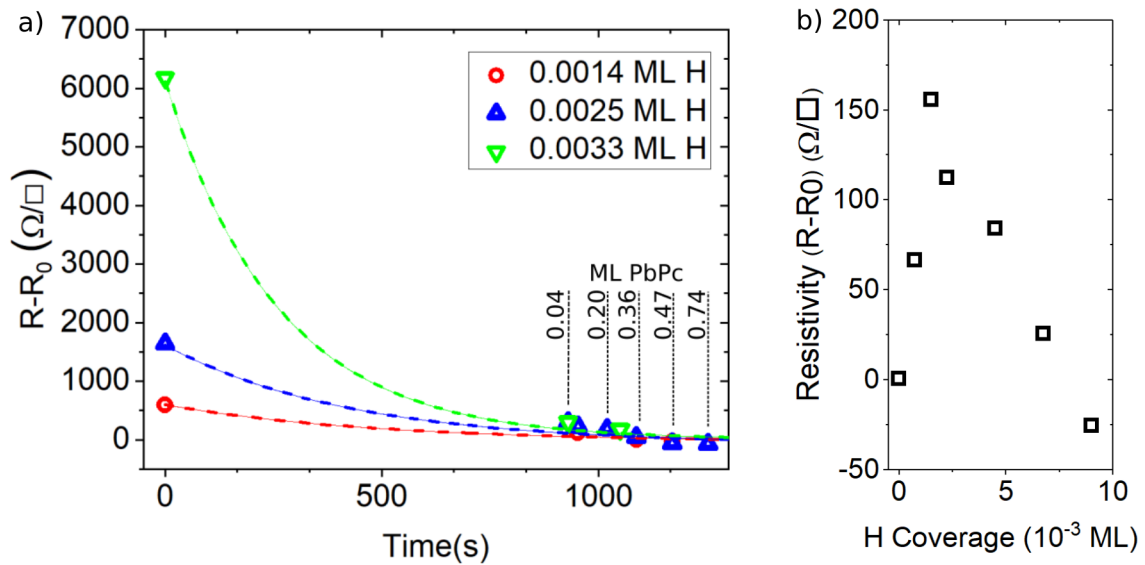
Figure 4.16: a) Change of resistivity versus time upon PbPc adsorption on MLG with different hydrogen coverage. The graph includes the transfer time prescribed by the experimental setup and the adsorption time of PbPc molecules. R_0 refers to the resistance of clean MLG. b) Change of the resistivity for H adsorption on 0.2 ML PbPc on MLG. The resistance values were corrected by the effect of molecule fragmentation during SEM imaging.

the transport behavior is ohmic and not changed with hydrogenation nor for the PbPc or the co-adsorbed phase.

To gain further insight into the system, measurements with a reversed adsorption sequence were performed. An initial coverage of 0.2 ML PbPc was evaporated to the substrate. The graphene surface still provides enough adsorption sites for hydrogen. Again the data is corrected by the molecular fragmentation. The results are shown in Fig. 4.16 b).

Compared to the reversed adsorption sequence, the observed change of resistivity is lower than expected for the localization process indicated by chemisorption of H atoms. This means, incoming H atoms are annihilated by the mobile PbPc molecules on the surface. The resistivity is increasing up to a coverage of 2×10^{-3} ML of hydrogen before reaching the original value again. The hydrogen adsorption was done subsequently using the same parameters for every step, excluding heating of the sample by the cracker filament as the reason for the transport behavior. The higher efficiency of the annihilation process for increasing H coverages may be explained by a modified retention times of the PbPc molecules in the islands or by varied mobilities of the molcules.

4.4.3 Theory and discussion

Under the assumption of a 2D PbPc gas on the surface, an increase of resistivity with increasing hydrogen coverage is expected. The concentration of mobile PbPc molecules is expected to be in the order of 10^{-5} with respect to the graphene lattice at maximum. For hydrogen coverages larger than 2×10^{-3} ML, the diffusivity of the molecules gets large enough to sample on average each graphene lattice site. The annihilation process gets more effective for higher hydrogen coverages.

Either the reaction of PbPc and H takes place before adsorbing to graphene, or the retention time of the PbPc molecules is modified by the presence of H-centers. Also, the PbPc islands are exposed to the hydrogen, which leads to an enlarged concentration of the PbPc gas at the surface, making the annihilation process more effective. Even after adsorption of 2 %ML of H, no significant change of resistivity is measured and no MIT takes place. This is indicative for higher order reaction dynamics. With the size of a PbPc molecules covering approximately 40 graphene unit cells, there are various reaction sited for H atoms provided.

To shine further light on this effect and the total reaction energy, DFT calculations were performed. The considerations are based on the reaction

$$(\mathrm{H/MLG})_\mathrm{s} + \mathrm{PbPc}_\mathrm{g} \rightleftarrows (\mathrm{MLG})_\mathrm{s} + (\mathrm{H/PbPc})_\mathrm{g}.$$
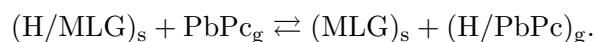
where $(\mathrm{H/MLG})_\mathrm{s}$ describes a chemisorbed H-atom at the MLG surface, while the index g refers to (physisorbed) species in the gas phase. The PbPc molecules provide a number of adsorption sites, e.g. the PbPc atom in the center, the C atoms and the N atoms on the lobe as shown in Fig. 4.12 [224]. The adsorption geometry of PbPc on planar MLG was analyzed in prior studies [215], and it was shown that the molecule adsorbs almost planar with the central Pb atom pointing upward. In a monolayer configuration the molecules are slightly tilted as revealed by π-stacking and intermolecular interaction details [217]. Intuitively, the atop position of the PbPc with its shuttlecock position appears as the energetically preferred since the π-stacking of the lobes and the MLG can be preserved. However a stable configuration was only found for H atoms adsorbed on top of the central atom. The calculated binding energies, with respect to atomic H and H_2 molecules are summarized in Table 4.1.

Table 4.1: Calculated binding energies the adsorption of atomic H to PbPc and free-base H_2Pc with respect to chemisorbed H at MLG and hydrogen in the gas phase. All energies are given in eV.

System	absorption site	@MLG	gas phase
Graphene +H	–	-0.95	
H + H	–		-2.26
HPc +H	C_{base}		-3.17
PbPc +H	Pb_{atop}	-0.03	+0.17
PbPc +H	Pb_{below}	—	-0.19
PbPc +H	C_{wing}	-1.17	-1.49
PbPc +H	N_{in}	-2.07	-1.99
PbPc +H	N_{out}	-2.38	-2.37
PbPc(H) +H	N_{out}	-2.70	-2.66
PbPc(H$_2$) +H	N_{out}	-2.53	-2.43
PbPc(H$_3$) +H	N_{out}	-2.83	-2.79
PbPc(H$_4$) +H	N_{in}	-1.03	-1.09
PbPc(H$_5$) +H	N_{in}	-1.08	-1.01
H$_2$Pc +H	N_{out}	-2.33	-2.26
H$_2$Pc(H) +H	N_{out}	-2.64	-2.60
H$_2$Pc(H$_2$) +H	N_{out}	-2.45	-2.38
H$_2$Pc(H$_3$) +H	N_{out}	-2.73	-2.70

The adsorption close to the plane of the wings, from below, is not possible and the H atom is barrier-less re-chemisorbed to graphene. An adsorption to the C atom at the wing, which is the closest to the substrate, is more probable. This could yield a reaction in between the H atom and the CH- group, resulting in a sp^3-hybridization of the affected C-atom. The concomitant structural relaxation of the wings results in a reduction of binding energy on graphene by 0.32 eV compared to the gas phase (cf. 4.1). Nevertheless, there still is an energy gain of 0.95 eV for adsorption of a H atom from the graphene layer.

The largest binding energy is found for adsorption of H atoms to the twofold coordinated pyridinic N_{out} atoms that bridge the four wings. The energy gain for this process is -2.38 , eV, which means an energy gain of 1.43 eV compared to H/graphene. Although the adsorption to the N_{in} atoms is possible, due to a small steric hindrance, the adsorption to N_{out} is preferred by 1.35 eV compared to an adsorption to N_{in}. Molecular hydrogen is not adsorbed by PbPc compared to the atomic species stabilized by the graphene support. The reaction of chemisorbed H atoms with the azo-nitrogen is surprisingly even barrier-free. The reaction between a chemisorbed H atom an a PbPc molecules is depicted in Fig. 4.17. Free base and planar H_2Pc molecules do not allow such an efficient reaction. The presence of the Pb atom obviously increases the reactivity of the molecule.

The chemisorption of H to MLG promotes the barrier-less reaction. Annihilation reactions with varying positions of the PbPc with respect to the H center of graphene were analyzed and show that the PbPc is guided, once the H atom is within the geometric dimension of the molecule. If one of the four N_{out} is crossing the H center with 0.2 Å lateral capture radius
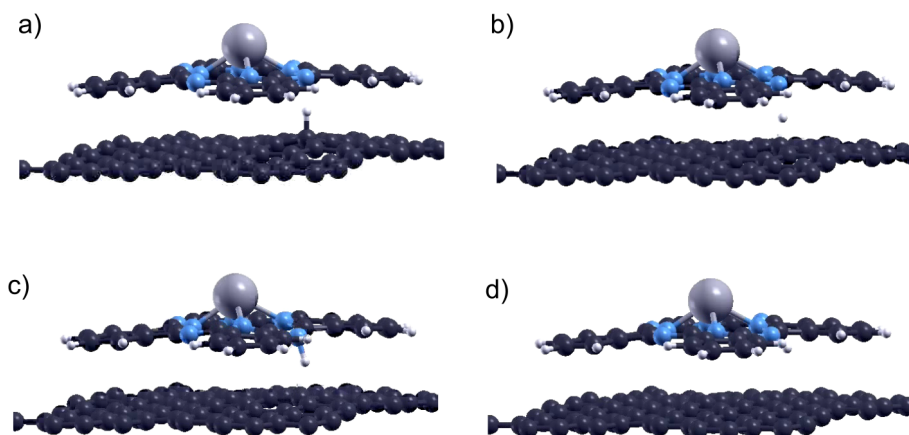
Figure 4.17: H atom chemisorbed on graphene reacting barrier-free with the nitrogen atom $N_o$ut of a PbPc molecule. The binding energies for further adsorption sites are shown in Tab. 4.1. a) Initial situation. A mobile PbPc molecule passes by a chemisorped H atom. b) The H atom is detached from the graphene. c) The H atom is transferred to the out N atom of the PbPc molecule. d) Final position. The H decorated PbPc molecule is relaxed.

the process is barrier-free, otherwise a multi-step process with moderate thermal activation energy is required.

The barrier-free reaction depends critically on the distance between one of the reacting N-atoms and the H atom. A threshold distance of 1.75 Å was determined for atomic-H attraction in the gas phase. This values holds also true for free-base H_2Pc and centro-symmetric CoPc and CuPc, confirming the reaction to be a common feature of Pc molecules.

Chemisorbed hydrogen is located about 1.8 Å above the lower part of the graphene substrate. This means, Van-der-Waals interactions allow a detachment of the H atom from graphene for H_{MLG}-N distances below 1.6 Å or adsorption heights below 3.4 Å. The detached H atom afterwards can be collected by the mobile Pc molecule.

The chemical reaction of atomic H-atoms and the N_{out}-atom of the molecule seems to be very local without parasitic inductive and mesomeric effects across the PbPc. The electron of the attached H atom is distributed over the entire molecule upon adsorption. The resulting HOMO is almost identical to the LUMO of isolated H-free PbPc, as shown in Fig. 4.18 a). As a result, the remaining azo-sites of PbPc can be subsequently saturated with additional H-atoms. For H_4PbPc a total binding energy of -2.83 eV is found. This is again only true for atomic hydrogen, the chemical reaction between molecular hydrogen and the PbPc molecules is neither probable nor energetically favorable. With respect to molecular H_2 a significantly lower binding energy of -0.5 eV is found.

While for H_4PbPc further adsorption of H atoms to the N_{in} position is possible, the strongly reduced binding energy of about 1.1 eV makes this reaction appear less probable. For planar Pc molecules, e.g. CoPc and CuPc , the binding energy of the third hydrogen adsorption is reduced to -1.9 eV, indicating the high efficiency of H annihilation is a generic property of non-planar Pc molecules.
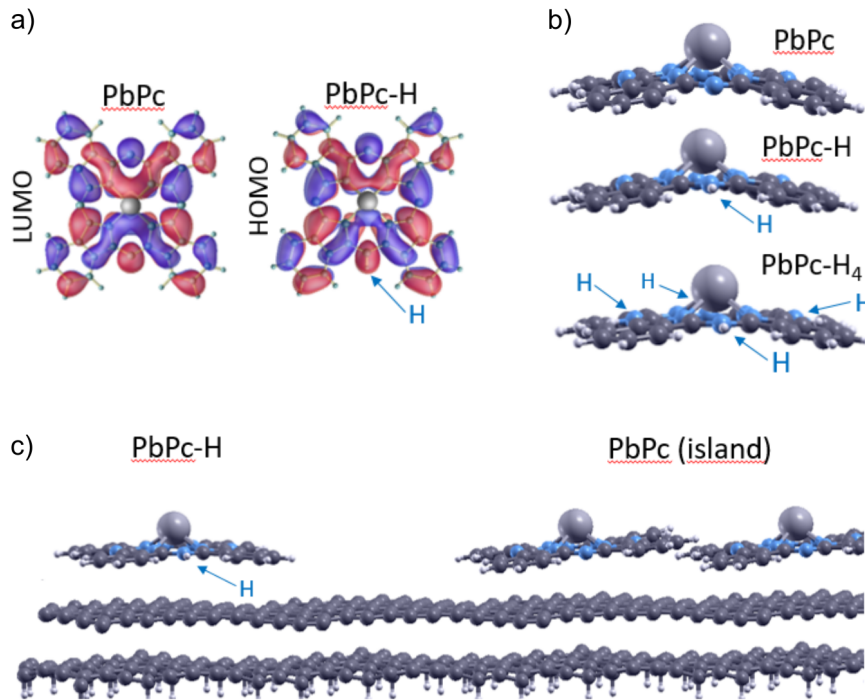
Figure 4.18: a) Comparison of PbPcb) PbPc molecule in the gas phase: The shuttlecock structure of the molecule flattens upon adsorption of H to the N_{out}-atom. b) Monolayer of PbPc and hydrogenated PbPc on epitaxial graphene. The intermolecular distance becomes significantly enlarged upon hydrogenation of the molecules due to a reduced flexibility of the wings. c) Isolated hydrogenated PbPc on MLG in comparison to layered PbPc molecules as found in islands. Because of the flattening of the PbPc molecule upon hydrogenation, the PbPc-H molecules tend to enlarge the intermolecular distance significantly or detach from the islands.

Compared to the gas phase structure of PbPc the relative bending of the shuttlecock structure is step wise reduced upon H adsorption as shown in Fig. 4.18 b). This flattening is independent on the substrate.,thus the resulting structure mimics more and more the one found for dense aggregation on HOPG [217], which suggests an increased binding energy if adsorbed on MLG. According te the DFT calculations this increase is actually moderate and amounts to roughly 0.03 eV per attached H-atom. Due to the flattening of the structure dense aggregation of the molecular species, as expected within the islands, gets less energetically favorable as depicted in Fig. 4.18. Consequently, H decorated molecules on the edge of the island are absorbed in a more planar form, this means they are slightly shifted away from the remaining PbPc island. On HOPG, a similar shift was found to remove the intermolecular interaction completely [217].

This means, H decorated molecules at the edge of the islands detach easily from the dense packed structure. This enlarged number of mobile PbPc molecules may give a hint towards the increased annihilation efficiency with increasing H exposure.

4.4.4 Conclusion

The co-adsorption processes of atomic H and PbPc molecules to MLG was analyzed by means of surface transport. While PbPc molecules couple very weakly to the graphene samples, localized hydrogen centers are known to strongly influence the transport behavior. This effect of hydrogenation to the transport properties of graphene is completely annihilated in presence of PbPc molecules. This interaction provides a chemical approach for selective reaction of mobile, physisorbed molecules.

DFT calculations reveal a barrier-free adsorption of hydrogen atoms to the azo-N atoms of the PbPc molecules. An energy gain is found for the reaction of one PbPc molecules with up to four H atoms, with a binding energy of $-2.8\,\mathrm{eV}$ w.r.t. atomic hydrogen for H_4PbPc. This annihilation process is found to be very effective and amplified by the size of the PbPc molecules.

4.5 Chapter conclusion

Graphene is a very promising material for different electronic and mechanical applications. Adsorption of atomic and molecular species to the initial inert material was analyzed within this chapter with special regard to possible sensor applications.

Atomic hydrogen has shown to have a massive influence on the transport behavior of MLG and QFMLG. Tiniest amounts, below $1\,\%$ of a monolayer of chemisorbed hydrogen induces a MIT. This large effect, obviously breaks the inert character of the graphene, providing a chemical approach for a selective reaction with physisorbed, mobile molecules.

The combination of atomic hydrogen and organic molecules on graphene was studied on the exemplary system of H and PbPc on MLG. The large effect of hydrogen chemisorption to graphene was found to be completely annihilated by the PbPc molecules. DFT calculations revealed that the N atoms of the PbPc molecules are preferential adsorption sites, allowing a barrier-free reaction with the chemisorbed H atoms. The size of the molecules amplifies the cross section of the reaction, making the annihilation process even very efficient.

Chapter 5

Low-dimensional carbon-based structures

Carbon is one of the most versatile building blocks for materials and depending on its form, hard as diamond or flexible as graphene. Microscopic carbon materials exist in different forms and dimensionalities, from zero-dimensional (0D) structures such as C_{60}, to one-dimensional materials like 1D carbon nanotube (CNT) and carbon nanofiber (CNF), up to 2D graphene layers and nano-sheets and finally the well known macroscopic materials like graphite and diamond [7–9]. These nanoscale structures are nowadays used as building blocks for compound materials, taking the nanoscale properties to a large scale producible macroscopic level.

This chapter is split in two parts covering two of those carbon-based materials. The first part of this chapter, Sec. 5.1 deals with CNF and the effects of doping them with nanocarbons, like CNT. The material system is presented in Sec. 5.1.1, followed by structural and electrical characterization in Sec. 5.1.2 and Sec. 5.1.3, respectively. The results are discussed in Sec. 5.1.4.

Section 5.2 describes the characterization of a graphene-based thin film conductor material. The material is described in Sec. 5.2.1, followed by the presentation of the experimental results in Sec. 5.2.2. Additional simulations to determine the complete conductivity tensor are described in Sec. 5.2.3. All transport investigations presented in this chapter were done by means of the 4pp-STM/SEM setup, which is describes in detail in Sec. 3.1. The results are summarized and concluded in Sec. 5.3.

5.1 Carbon nanofibers

Among carbon-based conductor materials, CNFs gained a lot of attention due to their simple fabrication, high temperature, chemical and mechanical stability and good electronic properties [39, 225, 226]. Within the different production methods, electrospinning and carbonization of polyacrylonitrile (PAN) is one of the most recognized. Compared to other precursor materials under investigation, like lignin and rayon, PAN leads to a higher degree of order within the graphitic structure of the fibers after high temperature carbonization [227].

This graphitic structure is the key parameter for modifying the material properties, because
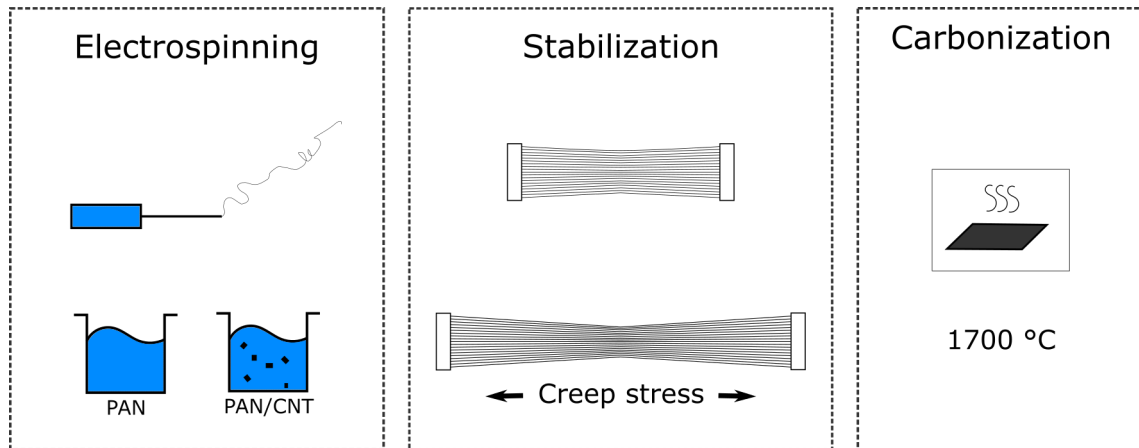
Figure 5.1: Schematic figure of the fiber fabrication process. Including electrospinning, stabilization for 10 h with or without external creep stress and carbonization at a temperature of 1700 °C.

of its impact to structural and electronic features of the sample. The formation of aligned graphitic domains in PAN fibers is limited by the formation of graphitic loops and by the disorder introduced to the carbon planes caused by the structure of the precursor material [228, 229]. One approach to overcome this limitation is the controlled addition of nanocarbons like CNT, often referred to as doping, which has already shown to improve the graphitization within the fibers [41, 42, 230, 231]. The effect of this doping on the structural and electronic properties of PAN-based CNFs is analysed and presented in the following.

These results were published as "Polyacrylonitrile (PAN) based electrospun carbon nanofibers (ECNFs): Probing the synergistic effects of creep assisted stabilization and CNTs addition on graphitization and low-dimensional electrical transport" by Ali, Slawig et. al. in Carbon 2021 [232]. The author of the present thesis participated in this study by performing and analyzing of the transport measurements and contributions to the original manuscript.

5.1.1 Sample variety and preparation

Sample preparation was done by A.B. Ali working in the group of Prof. Sindelar at the University of Applied Science Hanover. The fabrication process is schematically shown in Fig. 5.1 and can be found in more detail in Ali et. al. 2021 [232], where also the effect of different carbonization temperatures were analyzed from a structural point of view. The highest quality graphitic structure was found in samples processed at 1700 °C. Thus, these samples were used for the transport experiments presented here.

The samples were fabricated by electrospinning, followed by a 10 h stabilization step and high temperature carbonization. A set of four different samples with different process parameters was fabricated. Two of the samples are made from unmodified PAN. One of them was clamped during stabilization, exposed to the shrinkage stress contingent of the process to avoid free relaxation of the fibers, this sample is from here on marked as *PAN*. The other undoped sample was stabilized with additional creep stress during the stabilization step, from
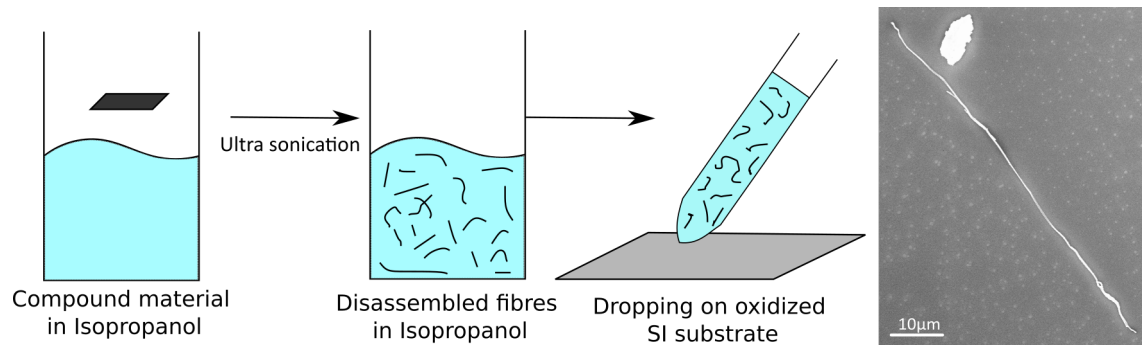
Figure 5.2: Isolation process of single fibers from the compound material. The compound is dissolved in isopropanol and ultrasonicated to ensure the disassembly of the fibers. The solution is dropped onto an oxidized silicon wafer and upon the evaporation of the solvent, the fibers are isolated on the surface. An Example of an isolated CNF observed by SEM is shown on the right.

here on named *PAN-T*. The same process was used for the CNTdoped, or templated, fibers. 1 wt% CNT was added to the initial solution, from which the samples were spun. Again, to one of the samples additional creep stress was applied, designated as *PAN/CNT-T*, while the other one was exposed only to shrinkage stress, named *PAN/CNT*.

Measurements were performed using the composite material and isolated single fibers. To single out individual CNFs, a piece of the fiber mat was dissolved in isopropanol and ultrasonicated for 5 min. The fibers are added to a oxidized silicon wafer via the drop casting method. The native oxide layer ensures the electronic isolation of the fiber from the silicon substrate. The solvent evaporates and the isolated fiber remains on the substrate. The complete isolation process is shown in Fig. 5.2. Isolated intact fibers with lengths of up to 80 μm were realized with this method. The main advantage of this isolation process is the ensure structural integrity of the fiber surface. It is therefore preferable to mechanical methods, like rubbing of the compound material.

5.1.2 Structural effects of CNT doping to CNF

While the focus of this work lies on the transport characteristics, A brief overview of the extensive structural analysis of the samples is given in the following. Detailed results of the structural analysis can be found in [232]

Scanning electron microscope (SEM) pictures of the four investigated samples are shown in Fig. 5.3. These images show that external creep stress (samples PAN-T and PAN/CNT-T) leads to an alignment of the fibers within the compound. The average diameter,measured after carbonization, ranges from 205 nm $\pm$ 49 nm for PAN to 250 nm $\pm$ 39 nm for PAN/CNT. The shrinkage upon carbonization is reduced for the CNT-templated samples, indicating a higher thermal stability of the sample. For comparison of the properties of the samples, the difference in diameter is neglectable. To gain deeper inside to the structural properties of the single fiber itself, X-ray diffraction, raman spectroscopy, infrared spectroscopy, x-ray photoelectron spectroscopy (XPS) and transmission electron microscopy (TEM) measurements were performed. The results can be briefly summarized as follows:
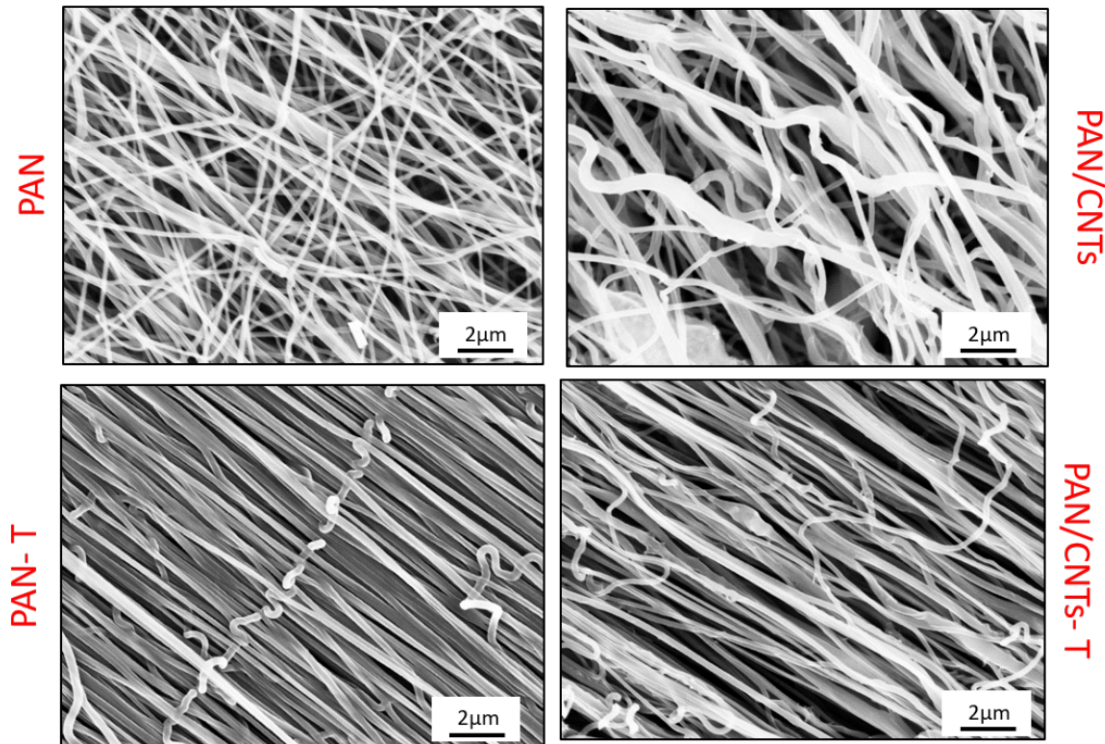
Figure 5.3: SEM pictures of the four investigated samples. The diameter of the fibers is found to be homogeneous and of similar size for all samples. The fiber compounds exposed to external stress are well aligned.

PAN fibers show no preferred alignment of graphitic planes. On an atomistic view, as observed in TEM measurements, curved fragments are observed, forming fullerene like structures. The addition of CNT increases the degree of graphitization inside the structure, as shown by a reduction of I_D/I_G ratio in Raman spectroscopy [233] and an increased sp^2/sp^3 ratio in XPS. This enhanced graphitization also increases the crystal size within the fiber, as seen in X-ray diffraction. TEM measurements reveal better aligned domains without curved fragments in the templated sample. These findings are in line with former studies, which have shown the formation of graphite in glassy carbon is enhanced upon the introduction of CNT. This effect can be explained by a confinement of matrix in the close range to the dopants [234] and the introduction of stress in the structure due to the alignment of the CNT [43].

The addition of creep stress during the stabilization process is known to improve the graphitic structure of the fibers, preventing curved structures and leading an enhanced orientation of crystal planes [235]. Surprisingly the atomistic picture shows, for the PAN/CNT-T sample a reduced graphitic plane alignment compared to the PAN-T as well as the PAN/CNT sample. Even fragmented and discontinuous domains are observed, which were not found in the other samples. Apparently, the admixture of CNT is counteracting on the effect of creep stress. CNT prevents the loss of orientation in a system without a global order by anchoring the PAN chains during stabilization. For the stressed system, the chains are aligned externally and the anchoring function of CNT is locally interfering with this effect.
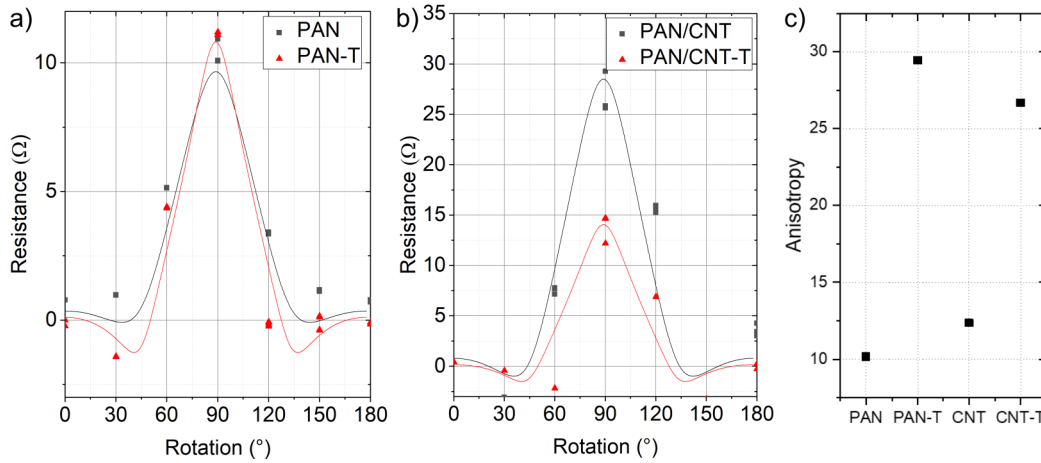
Figure 5.4: Rotational square measurement for a) PAN fibers with and without tension b) CNT doped PAN fibers with and without additional stress. c) Comparison of the anisotropy values corresponding to each of the samples.

5.1.3 Electrical Transport properties

Carbonized CNF with and without CNT doping were measured via four-point probe (4pp) STM. This approach has already proven to be a suitable method for fiber analysis [236]. Fiber mats as well as single fibers were addressed, leading to a wide variety of possible measurement approaches. Furthermore no contact fabrication, e.g., by lithography is necessary reducing the possibility of structural damage to a minimum.

The measurements done on the compound material show linear I-V characteristics, indicating ohmic behavior. I-V curves were recorded for different angles with respect to the main fiber alignment of the sample. The probe distance is $50\,\mu$m for all measurements. The resistance values in dependence fn the angle are shown in Fig. 5.4 a) and b) for the PAN and PAN/CNT samples respectively. The measurements reveal a clear dependence of the resistance on the angle between the measurement direction and the main fiber alignment direction. In both cases, the anisotropy is higher for the samples exposed to creep stress during the stabilization step, as shown in Fig. 5.4 c). When comparing the two non-stressed samples, the anisotropy is slightly increased upon templating with CNT.

The ensemble is microscopically not homogeneous so conductivity values can not be discriminated from anisotropy measurements, as described in Sec. 2.2.4. The analysis nevertheless gives rise to a qualitative comparison between the samples, indicating differences in fiber orientation and package density, which could already be seen in the SEM images.

The samples treated with creep stress, show much larger anisotropy values, which is obviously correlated to the improved alignment of the fibers within the compound. This effect limits the number of current paths perpendicular to the main fiber alignment direction. Previous work shows, that the electron transport in CNF takes place near the surface [236], therefore any fiber crossing acts as a scattering center, increasing the resistance along this current path. An improved alignment causes a reduction of fiber crossings and leads to an decreased resistivity of the compound material in the main direction of fiber alignment.
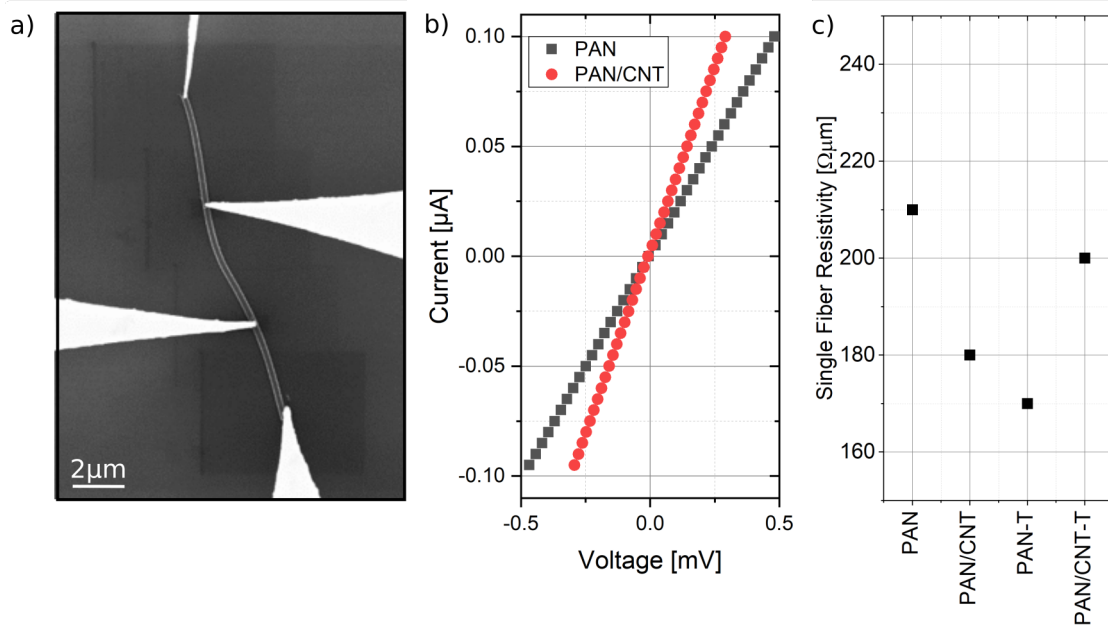
Figure 5.5: a) SEM image of a single PAN/CNT fiber contacted with 4 tips. b) Exemplary I-V characteristics of single fibers measured for the PAN and the PAN/CNT sample. The measurements indicate an ohmic behaviour for all samples. The resistance changes due to the structural changes upon external creep stress and templating. c) Overview of the measured conductance values of the samples.

To analyze the materials conductivity,the influence of different packing densities and the fiber alignment need to be excluded. To do so, single fibers were investigated. To eliminate contact resistance, 4pp measurements were performed, carefully positioning 4 probes on one sample. Fibers of all four types show linear IV characteristics, again indicating ohmic transport behavior. Apparently the main transport mechanism is conserved upon templating. The resistivity itself varies due to the structural changes within the atomic structure of the individual fiber. The single fiber resistivities are shown in Fig. 5.5 c). The resistance drops significantly upon the exposure to external creep stress in the presented samples, for PAN fibers by approx. 20% from 210 $\Omega\mu$m to 170 $\Omega\mu$m. This effect was observed in several studies before and is explained by the enhanced microscopic alignment of the graphitic units within the fiber [235–237].

A similar effect is observed when comparing the PAN and the PAN/CNT samples, where the templating significantly reduces the resistance, to a value of 180 $\Omega\mu$m. Similar improvement of the electrical and mechanical properties with increasing CNT doping has been shown before [238, 239]. Depending on the preparation an improvement of electrical conductivity up to 2 orders of magnitude for 0.5w% CNT in PAN CNF in possible[41]. The effect found in the presented data is not as large, but still significant. The exact quantity of the effect is dependent on the sample preparation method.

This effect is canceled for the PAN/CNT-T sample, where the measured resistance is 200 $\Omega\mu$m and is therefore higher compared to the PAN-T and the PAN/CNT sample. This counter intuitive results will be discussed in more detail in the next section.
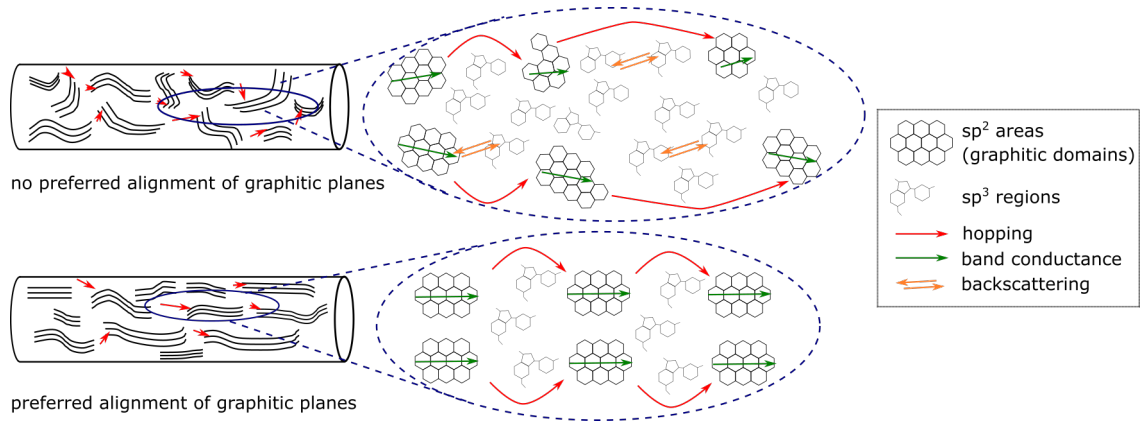
Figure 5.6: Schematic illustration of the electron transfer process through CNF without (top) and with (bottom) preferred alignment direction of the graphic planes. Within the crystal sp^2 hybridized areas, band conductivity is dominant (marked with green arrows), while in between the crystalline sptextsuperscribt3 parts hopping takes place (red arrows). The disorder of the structure on the top leads to an increased backscattering probability, resulting in a higher resistivity of the structure. The schematics are not to scale and the measured resistivity values indicate a low proportion of insulating parts.

5.1.4 Discussion: combining structural and electrical properties

The measured transport data is discussed in connection with the structural properties. The electrical properties of compound material are determined by the conductivity of single fibers and the local alignment. Electron transfer in CNF takes place close to the surface, therefore every fiber crossing acts as a scattering center. External stress improves the alignment of the fibers within the composite material, leading to enhanced conductivities. Due to different packaging densities, diameters and alignments of the sample sets a comparison of the single fiber properties can not be deduced from the compound material.

The internal structure of the fibers consists of sp^2 hybridized crystalline units and sp^3 hybridized areas. The electron transport process is a combination of band conductivity in the graphic domains and hopping in between those domains, across the insulating parts. Additionally, disorder within the fiber structure favors backscattering of the electrons, leading to an increased resistance. The electron transfer process is schematically shown in Fig. 5.6 for a fiber without and with preferred alignment direction of the graphic planes. Based on this assumptions the increase of number and size of the sp^2 areas result in an increase of conductivity.

This behavior, based on the structural properties, is suggested by the presented conductivity measurements. The structural analysis shows an enhanced graphitization and higher alignment of graphic planes for the PAN/CNT sample compared to the PAN fibers, as reflected by the increased conductivity of the templated fibers.

The exposure to external stress leads to an increased alignment of the graphic planes, as shown by comparison of the PAN and the PAN-T samples. In case of templated structures the influence of stress is not straight forward. In case of the PAN/CNT-T sample, the graphic planes are discontinuous and fragmented, leading to an increased resistivity compared to the PAN-T. This also leads to an increased scattering probability in between the ordered areas.

The increased backscattering probability partly voids the effect of enhanced graphitization.

5.1.5 Conclusion

The influence of nanocarbon doping on the electrical and structural properties of CNF was analyzed. Pure and CNT-doped PAN-based CNF were fabricated by electrospinning. Each sample type was stabilized with as well as without external creep stress. This set of four samples was analysed regarding structural and electronic properties. Measurements were performed on the compound material as well as on isolated single fibers.

External creep stress leads to an alignment of the fibers within the compound, reducing the anisotropy of the composite material. Additionally , the graphitic planes within the fibers are better aligned, resulting in a reduced resistance. The fibers stabilized without external creep stress, show an improved alignment of the graphitic planes upon CNT doping. This reflects to the electronic properties, resulting in decreased resistivity of the individual fibers. By combining both effects, the resulting in conductivity decrease compared to samples treated only with external stress or doping with CNT.

The presented findings reveal the strong dependence between electronic transport and the characteristics of the graphitic domains, e.g. size and alignment. External creep stress and the addition of CNT allow the tuning of those structural and electronic properties. The addition of nanostructures influences not only the structural properties but also the hopping and band mobilities.

5.2 Graphene-based conductor materials

To transfer the extraordinary properties of graphene to a macroscopic scale, nanocarbons like graphene flakes are used as building blocks to form composite materials. This concept is the base for a novel species of high carbon-based conductive materials. The bottom up approach and the corresponding influence of the exact assembly, overlap and alignment of the building blocks to the macroscopic conductivity causes a complicated analysis of the electronic properties.

For example, atomically thin sheets can be assembled from graphene dispersed in solution. From that a strong paper like material can be produced by vacuum filtration [35, 240, 241]. This facile synthesis allows, the fabrication of graphene-based nanoelectronic devices [242, 243]. Nevertheless the field of graphene-based conductor materials is still new and many challenges and opportunities remain. Within this work, the fundamental transport characteristics of this kind of material is under investigation. This provides the base for understanding the tailoring possibilities regarding possible future applications. The results presented in this chapter were published as "Anisotropic transport properties of graphene-based conductor materials" by D. Slawig et al. in the Journal of Materials Science [244]. While the transport study and analysis was performed by the author of this thesis, sample preparation and simulation were done by L. Rizzi, working for Bosch and the Technical University Chemnitz.
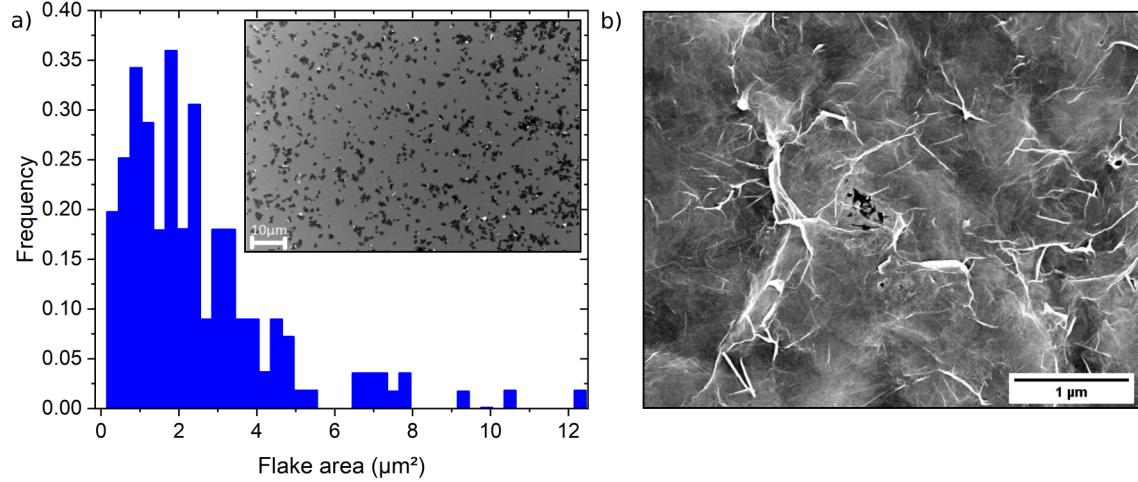
Figure 5.7: a) Area distribution of 177 graphene flakes on a silicon substrate, determined from high resolution SEM images. The shown flakes act as microscopic building blocks for the used sample. The flakes appear as dark gray shapes in the inset. The average flakes size is $2.51 \pm 0.15\,\mu\mathrm{m}^2$. b) SEM image of the sample surface, revealing inhomogeneities on the micro scale, while the overall sample is macroscopically homogeneous.

5.2.1 Sample preparation and structural properties

The graphene-based conductor materials were synthesized from a liquid graphene dispersion via vacuum filtration. This kind of materials are expected to be highly conductive, flexible and stable [35, 243, 245–247]. The dispersion was centrifuged to eliminate the smallest flakes. Analysis of SEM images of the final dispersion revealed an average flake size of $2.51 \pm 0.15\,\mu\mathrm{m}^2$. The area distribution was obtained from the analysis of SEM images, as shown in Fig. 5.7 a). The sample is produced from the flakes via a vacuum filtration process. More detailed information on the sample production process can be found in Ref. [37]. The film density of $1.41 \pm 0.11\,\mathrm{g} \cdot \mathrm{cm}^{-3}$ was calculated from the measured thickness of $4 \pm 0.3\,\mu\mathrm{m}$ and the determined mass of $6.4\,\mathrm{mg}$.

The SEM image shown in Fig. 5.7 b) exhibits a certain roughness of the surface, although the mum-sized flakes are arranged in flat layers. The film is homogeneous on a macroscopic scale, but the random positioning of the individual flakes cause an inhomogeneous structure on the microscale. The dispersion used to fabricate the investigated samples was 10 weeks old and comprised heavily agglomerated flakes. Due to this agglomeration, the sample is expected to contain rather nanographite particles than monolayer graphene flakes.

5.2.2 Experimental results: electrical transport measurements

The sample was brought to ultra-high vacuum (UHV) and degassed over $12\,\mathrm{h}$. Electric transport measurements were performed on the produced samples including a high number of graphene flakes, not on the single flakes itself. The probes were approached, fully feedback controlled, into tunneling contact, and manually lowered to form an ohmic contact with the sample surface. This ensured reliable transport measurements despite the flexible sample
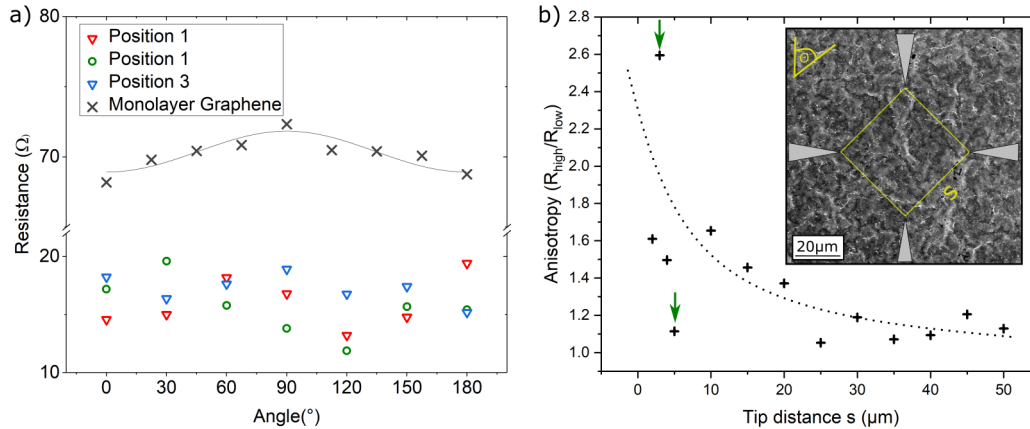
Figure 5.8: a) Resistance measured at three different positions (red, green and blue symbols) as a function of the rotation angle using the so called rotational square method (fixed probe distance of 50 µm), shown in the inset of panel b). For comparison, the data measured on a monolayer graphene sample (grey x symbols) [248] is shown. b) Resistance anisotropy (R_{high}/R_{low}) as a function of the tip distance. The dashed line is a guide to the eye. The green arrows indicate the strong variation of the anisotropy values. All measurements were performed at 300 K.

while keeping the surface damage reasonably low.

First, in order to gain information about the anisotropy, the rotational square method with a tip distance of 50 µm was applied. The tips were arranged in a square configuration, as shown in the inset of Fig. 5.8 b) and explained in Sec. 2.2.3. Measurements at different positions across surface were taken to investigate the overall homogeneity of the sample. The results for three different positions are shown in Fig. 5.8 a). The resistance values vary between $R_{high} \approx 20\,\Omega$ and $R_{low} \approx 12\,\Omega$, thus representing the overall good conductivity of this graphene-based conductor material. No significant differences for the different positions on the sample surface were found, indicating a macroscopic homogeneity.

Although, there are variations seen upon the change of angle, there is apparently no preferential direction for electron transport. To allow a comparison, a measurement on monolayer graphene [248] is shown. In thrdr two quasi-2D systems, which are very sensitive towards anisotropy, a clear maximum is visible, contrary to the measurements performed on the investigated material.

Apparently, in this graphene-based conductor material there are contributions from bulk transport, which expectantly lowers the sensitivity towards anisotropy. Uncorrelated variations are explained by microscopic inhomogeneities, i.e., the influence of the exact configuration of the flakes in between the measurement probes.

Tip distance (indicated in yellow as *s* in Fig. 5.8 b)) dependent measurements using a square configuration were performed to further investigate this effect. Based on the fact that the resistances along different directions show no clear trends, a fixed orientation of the square tip arrangement with respect to the sample was used. The ratio between the two measured resistance values, measured with an angle of 90° to one another, R_{high} and R_{low}, serve as an indicator for the local anisotropy. The results are plotted in Fig. 5.8 b).
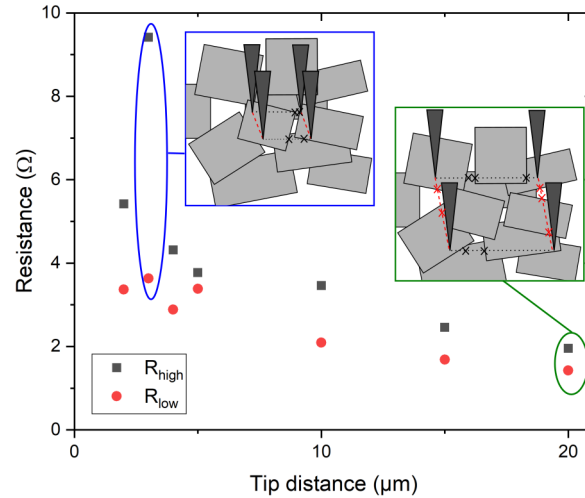
Figure 5.9: Measurement of the local anisotropy for different tip distances. The resistance increases with a decrease of the tip distance due to bulk contributions. For large distances a high number of flakes is in between the probes and the overlay is averaged in the different directions. For tip distances in the range of the average flake size, the number and orientation of the nanographitic flakes is crucial. The flakes are of nonuniform shape and pictures as square for reasons of clarity.

For large tip distances, no significant anisotropy was observed and the ratio is close to 1, i.e., the random orientation of a high number of flakes averages out any anisotropy. By reducing the tip distance, the anisotropy becomes gradually larger and exhibits a maximum around $s \approx 5\,\mu$m. In this distance range, strong variations of the anisotropy (marked by green arrows) are observed. For even smaller probe distances the anisotropy tends to saturate or possibly decreases. These measurements were difficult to realize, due to the materials flexibility and surface damages induced by the probes. For probe distances in the range of the average flake dimension of $\approx 1.5\,\mu$m^2, the anisotropy is expected to vanish, because the single flakes are isotropic and only their alignment and overlap gives rise to the measured anisotropy. This small probe distance could not be realized experimentally, but because of the influence of the exact probe configuration, and the variation of flakes sizes a conclusive data point is seen at a probe distance of $5\,\mu$m. For slightly larger distance, there is a high probability that adjacent flakes are contacted. Thus, the higher anisotropy values on this length scale of a few flake lengths, are indicative for a rotational misalignment of the flakes. This effect is schematically explained by Fig. 5.9.

One has to keep in mind that, for those small probe distances, bulk contributions play a major role within transport. The increase of the resistance with decrease of the tip distance is expected for a 3D transport regime. Apparently, for small distances, the number and also the orientation of single nanographitic flakes plays a major role. The azimuthal orientation of the flakes with respect to the fixed 4-tip assembly explains the conflicting anisotropy values marked by green arrows in panel b). For small distances, the exact flake configuration is crucial. A hallmark of the individual flake configuration at a certain position of the sample surface was observed, as this configuration significantly influences the measured conductivity.
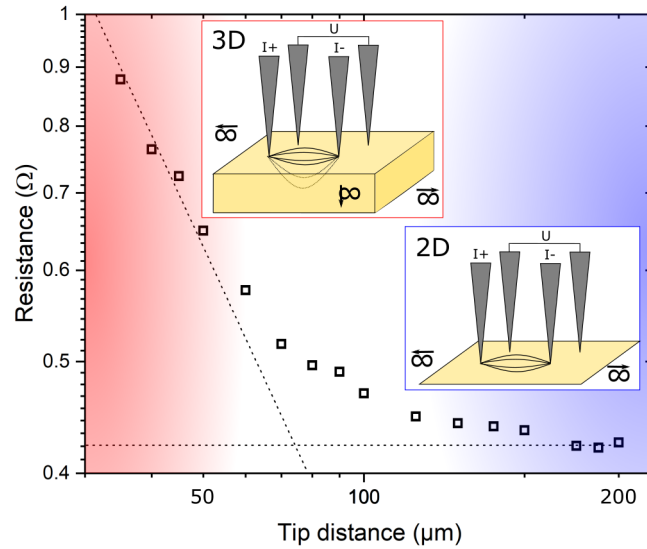
Figure 5.10: Resistance R versus the 4pp tip distance s in a semilogarithmic plot. The 2D and 3D regime is indicated in blue and red, respectively. The dotted lines describe the expected 2D and 3D behaviour based on the extracted conductivity values. The measurements were performed at 300 K using a squared array tip assembly as sketched in the insets.

Based on these conclusions not only the macroscopic sample but also the microscopic building blocks can be classified as anisotropic and microscopically inhomogeneous. This effect vanishes due to averaging for large dimension but has to be considered for understanding the fundamental material properties. While the in-plane anisotropy vanishes with large tip distances, the sample remains strongly anisotropic in the out-of-plane direction.

  Besides anisotropy and homogeneity, the dimensionality aspect has to be considered. The corresponding correction factor F_1 as determined in Sec. 2.2.2, based on the probe distance s and sample thickness t $= 4\,\mu$m, is unity.The factor beeing $F_1 = 1$ for t/s $< 1/4$ is only valid for homogeneous and isotropic materials, and marks the 2D regime in this case. For large tip distances the influence of single flake configurations can be neglected thanks to averaging and the system can be considered homogeneous and isotrop.

In contrast, for t/s > 4 the correction factor becomes dependent on the probe spacing s and determines to $F_1 = 2\ln 2(s/t)$. This behavior is expected for 3D transport [58, 60]. The variability of the measurement system allows a material characterization in 2 and 3 dimensions for thin film samples. Those two borderline cases of a 2D sheet and an infinite 3D sample are analyzed.

In order to further characterize the graphene-based conductor material, tip distances from $35\,\mu$m up to $300\,\mu$m were realized. Within this regime, no significant in-plane anisotropy was found and $\rho_x = \rho_y$ can be assumed. The results are shown in Fig. 5.10. A clear tip distance dependence is found and marks the 2D/3D transition. For a characterization of the 2D/3D transition, resistor network simulations were used.

As shown in Fig. 5.8, the system reveals no anisotropy for tip distances larger than s$=35\,\mu$m and appears as a 2D system for s $>100\,\mu$m. Therefore, the electrical resistivity in the 2D regime for the squared configuration can be deduced via $R_{2D} = \frac{\sqrt{\rho_y \rho_x}}{2\pi t} \ln(1 + \frac{\rho_x}{\rho_y}) =$
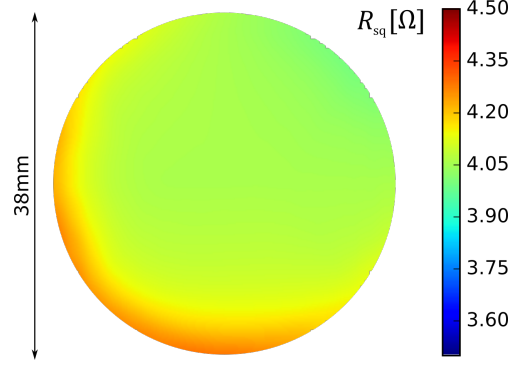
Figure 5.11: Eddy current measurement of the analysed film. The conductivity appears homogeneous on a macroscopic scale and the average value agrees with the data obtained from microscopic 4pp measurements.

$\rho_{x(y)} \ln(2)(2\pi t)^{-1}$ [58], where t is the thickness of the sample and ρ_x and ρ_y are the macroscopic resistivities in x- and y-direction. The resistance is assumed to be isotropic in this case. Details of the equations and their deduction can be found in Sec. 2.2.2 and Sec. 2.2.3. As a result, the in-plane conductivities $\sigma_{x(y)} = \rho_{x(y)}^{-1}$ for the 2D regime are determined to be $\sigma_x = \sigma_y = 65.2 \pm 1.6$ kS/m. To substantiate this result, additional macroscopic measurements via a non-contact eddy current device (SURAGUS EddyCus TFmap 2525SR) were conducted. The mean sheet resistance is approximately 4.1 Ω and the resistivity is found to be homogeneous across the sample, as shown in Fig. 5.11. The resulting conductivity of $\sigma_{eddy} = 61.1$ kS/m matches the microscopic 4pp measurements very well. This underlines the presented data, but only gives insight into the lateral conductance components and cannot fully reveal the anisotropic conductivity tensor including in- and out-of-plane parameters.

For probe separations between s=35 μm and s=100 μm , 3D behaviour (cf. Fig. 5.10) is observed. For this regime, the ρ_z component of the resistivity tensor can be deduced for a square 4pp configuration from $R_{3D} = \frac{\sqrt{\rho_{x(y)}\rho_z}}{\pi s}[1 - (1 + \frac{\rho_x}{\rho_y})^{-\frac{1}{2}}] = \frac{\sqrt{\rho_{x(y)}\rho_z}}{2\pi s}(2 - \sqrt{2})$ [58]. Based on the in-plane conductivity mentioned above, the out-of-plane conductivity is $\sigma_z = 133 \pm 0.5$ S/m. This result clearly corresponds to graphite, which is known to show anisotropy values in the range of 4×10^{-4} [249], rather than to graphene [249, 250]. This is an expected result due to the sample preparation method.

The 2D/3D transition discussed in context of Fig. 5.10 occurs at a considerably larger tip separation length than expected from on theory [58]. However, considering an *effective* thickness of the material $t_{eff} = t\sqrt{\xi}$, with $\xi = \frac{\rho_z}{\rho_{x(y)}} = \frac{\sigma_{x(y)}}{\sigma_z} \approx 490$ as the bulk anisotropy, the condition determining F_1 becomes $s \approx 4t_{eff} = 4t\sqrt{\xi}$. Using the sample thickness of t=4 μm and $\sqrt{\xi} \approx 20$, a tip distance of $s \approx 320$ μm is at least required to enter into a full 2D behavior. This is in good agreement with the presented findings.

5.2.3 Simulation

The simulations are based on a three-dimensional (3D) random resistor network model and were executed by Bosch in cooperation with the Technical University Chemnitz and the Fraunhofer Institute for Electronic Nano Systems ENAS.

Nanographite flakes were modeled as randomly shaped polygons with a surface area A and a thickness t_{flake}. The individual flakes were grouped into layers, which were then stacked to form a 3D structure. Despite the random flake shapes and positions, control over the overall packing density of the structure p and the average surface area of the flakes $\bar{A}$ is achieved. Overlaps between flakes constitute the nodes of the network, while the individual flakes connecting the nodes correspond to the edges. In-plane electron transitions between flakes can be neglected compared to the dominant out-of-plane transitions. From the fully constructed resistor network the macroscopic electrical conductivity of the given system is computed. Further details are reported in the publications by Rizzi et.al. from 2018 and 2020 [36, 37].

The resistances of the network edges are based on the following geometric properties: the overlap areas, the distances between overlaps, and the orientation of overlaps towards each other. Additionally, the flake thickness t_{flake}, the in-plane flake conductivity σ_{in} and the conductivity between individual nanographite flakes σ_{out} are included. While the geometric properties are randomly generated and only their averages are controlled. t_{flake}, σ_{in}, and σ_{out} serve as physical input parameters. They characterize the individual microscopic building blocks of the thin film and are closely linked to the macroscopic conductivity tensor. The input parameters can be modeled according to statistical distributions or with uniform effective quantities [36].

The 4pp transport measurements yield the macroscopic conductivity tensor $\sigma = (\sigma_{x(y)}, \sigma_{y(x)}, \sigma_z)$. With the help of microstructural simulations, the macroscopic sample conductivity is mapped to the properties of the microscopic building blocks. For the simulations presented here, the structures comprised a minimum of 95 000 flakes. The experimentally determined values of $\bar{A} = (2.5 \pm 0.15)\,\mu m^2$ and the packing density of $p = 0.6199 \pm 9 \cdot 10^{-5}$ were fixed. Performed parameter studies for 675 sets of the physical input parameters were performed, covering the range of $96\,layers \leq t_{flake} \leq 104\,layers$, $100\,kS/m \leq \sigma_{in} \leq 1500\,kS/m$ and $200\,S/m \leq \sigma_{out} \leq 1000\,S/m$. σ_{out} and σ_{in} refer to out-of and in-plane conductivity components on the microscopic scale, i.e., for the graphitic nanoclusters. These parameter ranges were identified with an appropriate set of test simulations to limit the calculation time. The resulting macroscopic film conductivities $\sigma_{x(y)}$ and σ_z are visualized in Fig. 5.12.

The flake thickness t_{flake} is directly converted to the number of stacked graphene layers N in each nanographite flake and indicated by the color of the circle in Fig. 5.12. In this representation, all data points that correspond to a specific flake thickness are located on a straight line, with negligible deviations due to the hidden parameters σ_{in} and σ_{out}. The reason for this being geometric anisotropy of each individual flake. Since the average flake area $\bar{A}$ is fixed, each flake thickness yields a different ratio of the flake dimensions, i.e. a well-defined different geometric anisotropy.

The black frame, magnified in the inset in Fig. 5.12, indicates the margin of error for the results of the 4pp measurements. The frame immediately shows that the measured results can only be obtained when the average flake thickness in the thin film is between 98 and 104 graphene layers, which confirms the building blocks to be nanographite rather than graphene. Based on the best fitting parameter sets, compared to the measured conductivity tensor, 675 different structures are generated, to evaluate the statistical fluctuations due to microstructural variations. The mean of each parameter set is shown in Fig. 5.12. While several possible combinations of $\sigma_{x(y)}$ and σ_z are found which are located within the range of the experimental
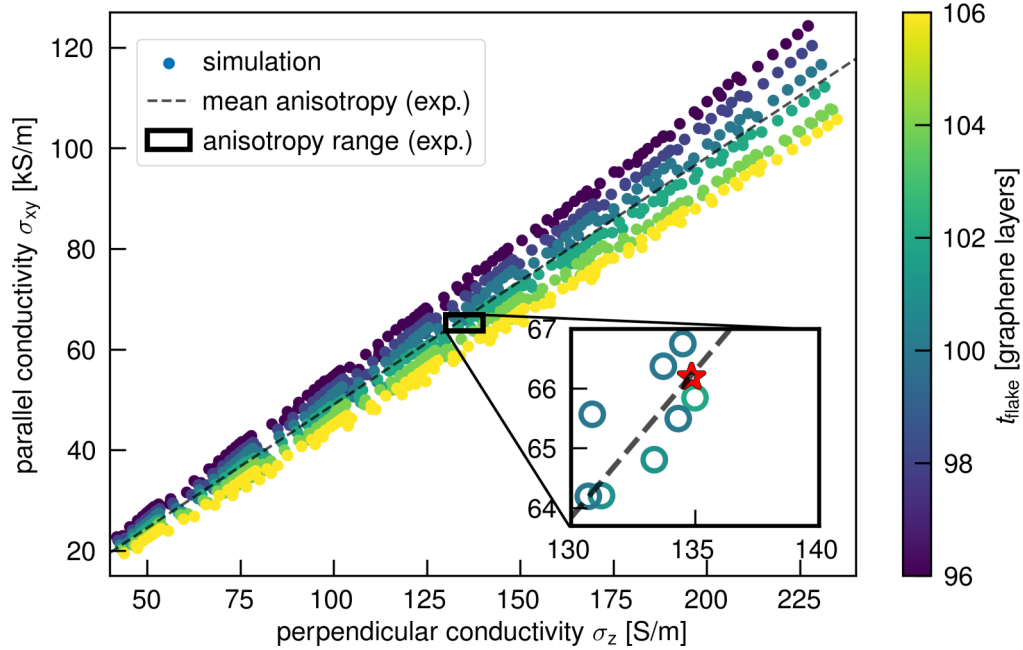
Figure 5.12: Simulation results for 675 different parameter sets. The black square indicates the anisotropy range expected from the experimental data, the black dotted line illustrates the mean experimental anisotropy. The optimized parameters are the in-plane and out-of-plane conductivity values, as well as the number of atomic layers in the graphite flakes. Every set of fitting parameters are indicated by circles, the color indicates the number of atomic layers. The enlarged part of the simulation results shows the anisotropy range expected from experiments, the parameters producing the best fitting results are indicated by the red star.

results, the parameters fitting best to the mean anisotropy can be identified (marked by red star). The optimal parameter set and the resulting macroscopic thin film conductivities are summarized in Table 5.1. The determined values for the flake conductivity $\sigma_{\text{in}} = 350\,\text{kS/m}$ and the conductivity between flakes $\sigma_{\text{out}} = 810\,\text{S/m}$ are well within the known range of graphite conductivities [251]. These parameters complete the microscopic explanation for the macroscopic thin film measurements.

5.2.4 Conclusion

A nanographite-based thin film conductor material was investigated. This material is representative for many solid state phases fabricated from microscopically well-defined two-dimensional building blocks. Systematic 4pp measurements with varying probe spacings reveal characteristic length scales at which such compounds can be treated as isotropic and even 2D. Moreover, for length scales close to the size of the microscopic building blocks, details about the assembly of these were unveiled and used as input for network simulations. By modelling the experimental conductivity values, details of the network structure as well as the electronic properties of the microscopic flakes became accessible and allow a comprehen-

Table 5.1: Parameters producing the best fitting results determined by simulation. σ_{in} and σ_{out} refer to the in-plane and out-of-plane conductivities for the microscopic nano-graphitic building blocks and $\sigma_{x(y)}, \sigma_z$ to the properties of the macroscopic graphene-based conductor material, respectively.

t_{flake} [layers]	σ_{in} [kS/m]	σ_{out} [S/m]	$\sigma_{x(y)}$ [kS/m]	σ_z [S/m]
100	350	810	66.257 ± 0.256	134.86 ± 0.3952

sive description of the material. The combination of transport measurements and simulation allowed the determination of the complete conductivity tensor.

5.3 Chapter conclusion

Two types of low-dimensional carbon-based conductors were analyzed, CNT-templated CNF and a graphite-based conductor material.

Mayor similarities were found in regard to the electrical resistivity. A main point of influence is the degree of ordering within the structure. The crystallite size and the alignment of the planes towards each other play a mayor role in determining the resistivity. Within well ordered graphitic areas, band conduction takes place. The crystallites are interfused with sp^3- hybridized areas or grain boundaries. These act as scattering centers or even barriers, allowing only tunneling or hopping electron transport. This co-existance of transport mechanisms raises the need of a complex description for electron transport through this group of materials.

While macroscopic transport characteristics can be determined quite easy through established measurement methods, investigating microscopic building blocks is more complicated. Not only the microscopic properties of the individual building blocks but also their crossings and alignment towards each other play a major role. This effect gives, for example, rise to the improved conductivity of CNF exposed to creep stress.

While effects originating from the exact configuration of the microstructures are averaged out on a macroscopic scale, they have to be considered for a detailed description of the materials properties. In the case of CNF the alignment of the graphitic planes within the fibers plays a major role for the transport characteristics. A similiar effect found in the graphite-based conductor material is the presence of the number of graphite layer within the single building block gets crucial as shown by simulations.

From a technological point of view, only detailed understanding of the microscopic and mesoscopic properties of these materials will allow the optimization of materials for applications like energy storage or sensing. Characterization of novel carbon-based materials was shown on two exemplary systems. Mayor focus was put on the combination of macroscopic and microscopic investigation, allowing to paint a complete picture of electron systems inside this promising materials.

Chapter **6**

Transport through single helical molecules

In this chapter, transport measurements through single polyalanine (PA), (within this study: polyalanine based polypeptides) molecules by means of mechanically controllable break junction (MCBJ) are presented. The molecules and their relevance for research and development are explained in regard to their special spin filter properties, namely the chiral induced spin selectivity (CISS) effect in Sec. 6.1. For the use of this effect the understanding of electric transport properties through this class of molecules is of general interest. The present work targets this issue, compared to the former chapter, on a more fundamental level. The experimental results are shown in Sec. 6.2. A model describing the results and a discussion of the measurements is presented in Sec. 6.3, followed by the conclusion of this chapter in Sec 6.4. Most of the findings in this chapter were published under the title of "Electronic transport through single polyalanine molecules" by D. Slawig et al. in Physical Review B 102 [119].

6.1 Polyalanine molecules and the CISS effect

6.1.1 The CISS effect

Enantiomers in chemistry are stereoisomers of molecules, that have identical composition, connectivity and conformation - but also have a non super-imposable mirror image. The two stereoisomers are comparable with a persons left an right hand, that also are mirror images of each other. The possible existence of two enantiomers of a molecule is called chirality.
A lot of biomolecules are chiral, e.g. DNA, peptides or proteins [252–254]. A polypeptide is used in the present study. Chiral molecules provide an unusually large electron spin polarization, known as the CISS effect. The large spin selectivity is unanticipated, since organic molecules are non-magnetic and known for their small spin orbit coupling (SOC). It was shown, that in fact the secondary structure is relevant for spin polarization [254]. Once the spinpolarized current is created, no further chirality of the material is needed to preserve this polarization [50].
Within the last two decades theoretical studies on the CISS effect [255–262], resulted in a
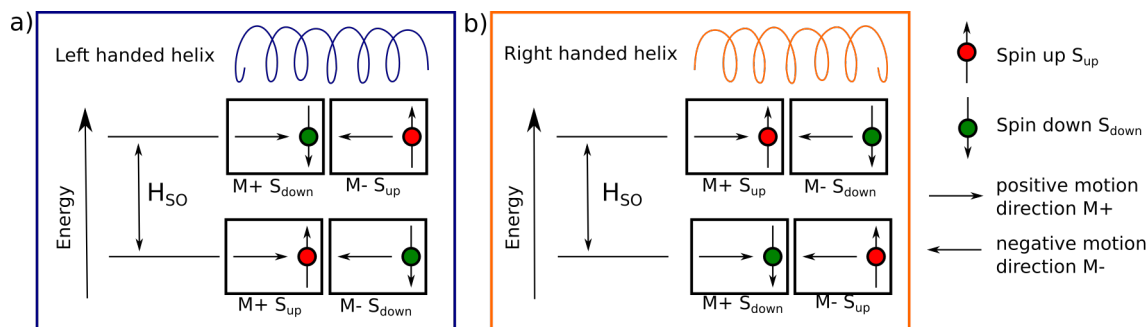
Figure 6.1: Energy scheme for the momentum-spin states of an electron propagating through a helical molecule. The states corresponding to opposite direction of motion and spin are degenerated and separated by an energy corresponding to twice the spin-orbit energy. For a left handed a) and a right handed b) helix, the ground states are exchanged. (Adapted from [48])

now broadly accepted model. It correlates the spin selectivity with a combination of enhanced SOC connected to breaking of spatial inversion symmetry. Anyhow the CISS effect is not understood so far and underestimated by several orders of magnitude by theoretical approaches.

The most simple approach to explain the CISS effect, is to consider a helical potential along the propagation axis of an electron. The lack of inversion symmetry and the transverse electric field component, cause an effective magnetic field oriented along this propagation axis. Within this effective magnetic field, the degeneration of the electron spin states is annulled leading to two possible spin states.

Cyclotron motion can be used for an estimation of the magnitude of this effective magnetic field within the molecules. Within this model the effective magnet field B_{eff} is given by

$$|B_{eff}| = \frac{mv}{qr} \tag{6.1.1}$$

where m describes the electrons mass, assuming the rest mass of a free electron, given by m = 9 × 10^{-31} kg, q indicates the electrons charge q = 1.6 × 10^{-19} C. At a kinetic energy of 1 eV the electron velocity is v = 6 × 10^5 m/s. The molecular radius is given by r, a typical value of r = 0.5 nm is assumed here. Based on these considerations, the SOC can be estimated by

$$H_{SOC} = \frac{g\mu_B}{2}|B_{eff}| = \frac{g\mu_B mv}{2qr} \tag{6.1.2}$$

where μ_B = 9.2 × 10^{-24} J/T is the Bohr magneton, and g is the g-factor for an electron. Within this model H_{SOC} is determined to H_{SOC} = 390 meV. By applying this simple model, the estimated value for H_{SOC} is large enough to explain the CISS effect. The distance in between the two possible spin states is hereby twice the value of H_{SOC} [46]. The freely propagating electron now has four possible states, described by the direction of motion (M+ designates positive direction and M− negative direction) and the direction of spin (S_{up} indicating spin up and S_{down} spin down). For an electron moving in the positive direction M + through a left-handed helix, S_{up} is stabilized relative to S_{down}. Thus M + S_{up} is the ground state. An electron with negative spin moving in the same direction, in the state M+ S_{down} is

located higher energy. In between the two states is a gap corresponding to twice the spin-orbit energy H_{SOC}. This scenario is depicted in Fig 6.1 a). Furthermore each state is degenerate with the state for an electron moving in the opposite direction with the opposite spin, thus the states $M+$ S_{up} and $M-$ S_{down} are degenerate as well as $M+$ S_{down} and $M-S_{up}$. If the handedness of the helical molecule is changed, the ground and the higher lying states are exchanged, as depicted in Fig. 6.1 b).

By now, it is known that no spin flipping takes place within this effect, but the backscattering of electrons containing the preferred spin is suppressed, while it is enhanced for electrons with different spin direction [254]. It was shown that the enhancement factor of spin polarization in helical systems is larger by a factor 10^2-10^3 compared to planar systems [263].

From the experimental side of view, many approaches were used to shine light on the described effect. The CISS effect was initially discovered by photoemission experiments. A monolayer of chiral molecules on a gold layer was found to provide spin selective properties. Based on the knowledge that circular polarized light ejects spin polarised photoelectrons from gold, switching the lights polarization and monitoring the photoelectron transmission, leads to the conclusion that the transmission through the chiral monolayer is spin dependent [264, 265]. This first examinations were followed by studies using photoemission [44, 266] electronic transport via magnetoresistance [47, 267, 268] and single molecule studies [45, 269, 270]. Furthermore, electronic transfer correlated with spin selectivity was under examination e.g. via spin dependent electrochemistry [266, 267] and capacitance analysis [271]. Chiral molecules and their spin polarization properties are of high interest regarding the development of future electronic devices and ongoing investigations reveal the high potential of this molecular based spintronic approach, indicating their future relevance in electronics and chiral selective chemistry [272, 273].

However, detailed investigation of electron transport across single PA molecules are missing to date. The possibility to achieve spintronic devices without permanent magnets is promising in regard of miniaturization and new device concepts. There was already a proof of concept for a new memory device based on chiral molecules [47]. Recently, it was shown that simply chemisorbing a molecular layer of chiral molecules results in magnetization of a ferromagnetic substrate [274, 275]. This effect does not require external magnetic fields or current and may provide possibilities for further miniaturization of electrical devices by serving as a miniature magnetization opportunity.

6.1.2 Polyalanine molecules
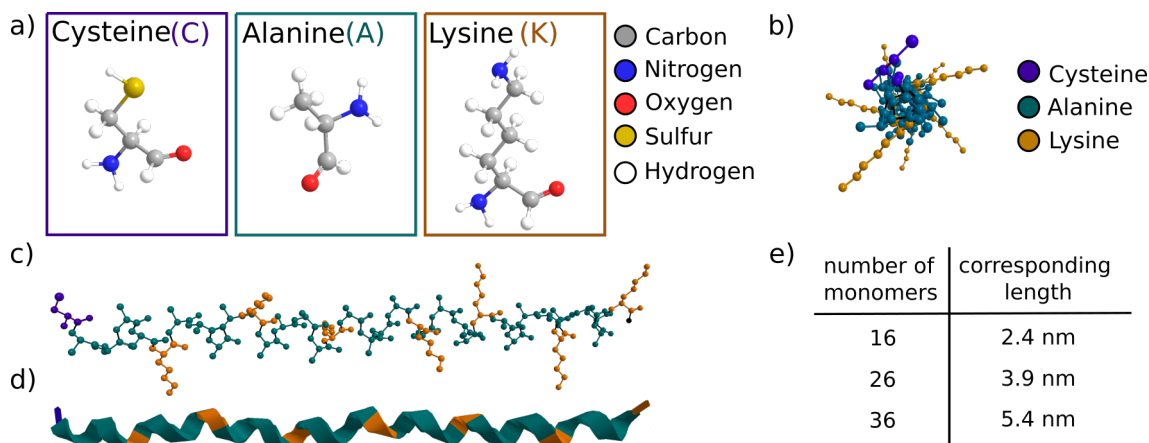
Figure 6.2: Peptides used in this study. a) The building blocks cysteine (C), alanine (A) and lysine(K) forming the molecular structure. Atomic structure of the 36mer polypeptide b) along the helical axis and c) perpendicular to the helical axis. d) Schematic picture of the α-helix structure, containing 10 windings. The colors represent the individual building blocks. e) Overview over the number of monomer building blocks and the corresponding lengths.

During this work, polyalanine based peptides, PA in the following, were analyzed. The peptides are build up from alanine (A), cysteine (C) and lysine (K) in a sequence of C[AAAAK]$_n$. An atomistic picture of the individual building blocks is shown in Fig 6.2 a). Those molecules arrange in an α-helix secondary structure, which is known to be very stable.
In this study three different molecular lengths were used, containing 16 (n=3), 26 (n=5) or 36 (n=7) monomers (16mer, 26mer and 36mer molecules respectively). The helix features a pitch size of 0.54 nm per winding, resulting in molecular lengths of L_{PA16} = 2.4 nm, L_{PA26} = 3.9 nm and L_{PA36} = 5.4 nm. An overview over the number of monomers and the corresponding lengths is shown in 6.2 e). As an example, the 36mer molecule is depicted in an atomistic presentation in Fig. 6.2 b) and c), Fig. 6.2 c) shows the helical secondary structure. Due to the structure of the molecules there is a large intrinsic dipole, e.g. around 129 D for a 36mer molecule.
Scanning tunnelling microscope (STM) studys [276, 277] reveal the formation of a self assembled monolayer (SAM) on the surface of gold (Au) contacts [276, 277]. The thiol (-SH) functional group located at the C unit of the PA molecules ensure a strong bond to the gold contacts. The strong dipole is expected to have an impact on the self-assembly of the molecular layer. The STM measurements reveal a well ordered lattice-periodic structure with hexagonal symmetry on the Au(111) surface as shown in Fig. 6.3 a) [276, 277].
Former studies on PA molecules on highly oriented pyrolytic graphite (HOPG) samples, show a very similar picture [278]. Hydrogen bonds in between the NH and CO functional groups along the helical backbone are enabled by interdigitation of the molecules. Due to this, the molecular layer reveals a lateral and also a high rotational order. Density functional theory (DFT) calculations show a strong hybridization between the S 2p and the Au 3d states for cysteine on Au(111), along with the formation of bonding and antibonding states below

the Fermi energy E_F [279]. Another outcome of these calculations is the rotation of the molecular axis of cysteine by around $30°$ with respect to the surface normal. Further details depend severely on the residual groups as well as the length of the molecules [280].

In order to verify the length of the molecules used in the transport experiments STM
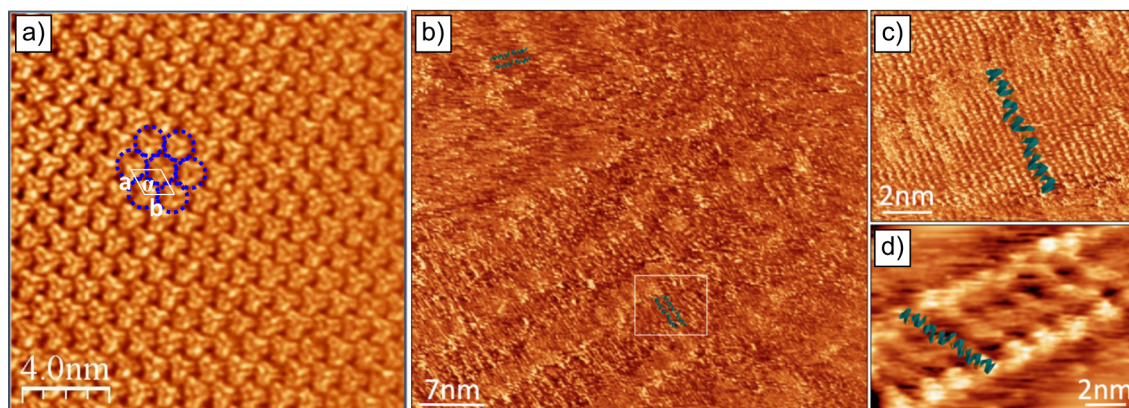
Figure 6.3: a) STM image recorded for thiolate-terminated molecules at $+1.5\,V$ and $0.5\,nA$. A densely packed monolayer with a unit cell of $a = b = 1.2\,nm$ and an angle of $\alpha = 60^c$irc. Figure from [277] The thiole end group causes an up-right standing alignment of the molecules. STM images b) to d) are recorded for phenyl-terminated PA molecules, the phenyl groupd cause a flat lying arrangement of the molecules. b) Different domains can be observed in large-scale STM images. Image taken under ambient conditions in solution. c) Zoom-in of b), showing more clearly the assembly of the PA molecules into stripes ($+1.1$ V, 1.1 nA, 300 K). d) Closeup of the same PA/HOPGsystem investigated by UHV-STM ($+1.2$ V, 0.9 nA, 77 K). The average length is about $5.4 \pm 0.3\,nm$. (Fig. taken from [119])

measurements on 36mer molecules functionalized with phenyl groups on both ends were performed. Phenyl groups lead to a flat-laying configuration of the molecules. As shown in Fig. 6.3 different domains can be observed. High resolution STM images performed under UHV condition show molecules lining up in stripes. The unidirectionally closed packaging for the flatlying molecules is most likely, favored by the interdigitation process, which was proposed for the formation of self-assembled monolayer structures on HOPG and Au(111) [277, 278]. The length of the molecules was determined to be 5.4 ± 0.3 nm. This analysis is limited by the quality of the STM measurements, although the length can be considered constant in the scope of this study. This is in accordance to the expected quality for molecules synthesized by means of a peptide sequencer.

6.2 Experimental results

All measurements shown in this chapter were performed by means of MCBJ which is explained in detail in Sec. 3.2. Clean Au junctions were measured as a baseline for the molecular measurements. The typical steps at integer values of G_0, as expected from the Landauer fromula, Eq. 2.1.11 explained in Sec. 2.1.3, were observed in the measurements. This result is exemplarily shown in Fig. 6.4 a). The conductance trace is plotted over time, to underline the long
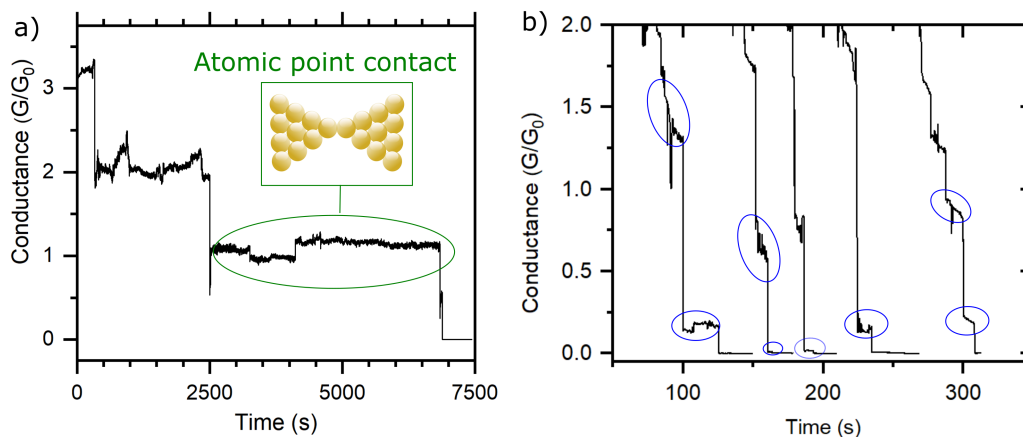
Figure 6.4: a) Conductance trace of a clean Au junction. Clear steps at integer values of G_0 can be seen, indicating the formation of an atomic point contact. The measurement is plotted versus time, to show the junction stability, which is proven by measuring an atomic point contact for more than 30 minutes. b) Conductance traces during the opening cycle of a junction with 36mer PA-molecules. The steps above G_0 can be attributed to Au-Au configurations. The plateaus below G_0 correspond to molecular configurations inside the junction. The different traces are shown to underline to importance of statistical analysis. (Fig. taken and modified from [119])

time stability. The value of $1\,G_0$ is characteristic for an atomic point contact formed by Au atoms and was stable for more than 30 min [281–285]. This indicates a high stability of the measurement setup. An exposure to the used solvent without molecules show no difference to the clean junctions, indicating a complete evaporation. The latter conductance traces, show well established plateaus below G_0, as shown in Fig. 6.4 b), which are not present in traces from clean or pure solvent exposed junctions . Therefore this low conductance values can be attributed to transport through single PA molecules.

The conductance traces of molecule incorporated junctions differ strongly in comparison to each other, which can be explained by different molecule-contact and molecule-molecule configurations inside the junction. To extract reliable information from those measurements a statistical analysis was performed. Up to 2×10^6 conductance traces at a constant bias voltage of $10\,\mathrm{mV}$ were evaluated for each of the three molecules lengths. The recorded conductance values plotted as histograms are shown in Fig. 6.5. Histograms present the distribution of data. The data range is divided into a series of intervals, so called bins. The bin size used in this study is $0.002\,G_0$. The number of events that fall into a specific bin is counted. This allows a lucid imaging of the plateau values.

For each molecule the histogram reveal the most probable conductance values (marked by violet arrows), which are $G_{PA16} = 50\,\mathrm{mG_0}$, $G_{PA26} = 10\,\mathrm{mG_0}$ and $G_{PA36} = 7\,\mathrm{mG_0}$. Additional satellite peaks, most clearly seen in the 36mer molecule measurement, can be identified in all the histograms. The satellites are better visualized on a logarithmic scale as shown in the insets of Fig 6.5. Those satellite peaks refer to different molecule-molecule configurations [86, 286], as discussed in detail in Sec 6.3.2.
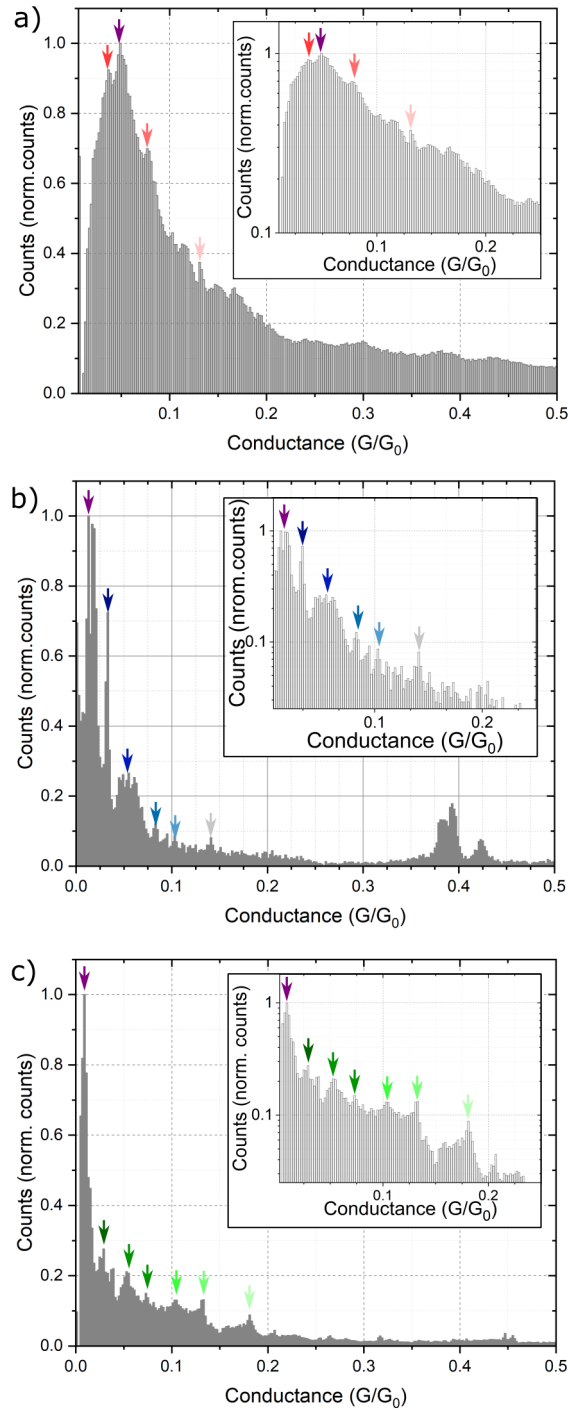
Figure 6.5: Normalized conductance histograms of PA molecules of different length in between Au electrodes. The histograms are normalized to the peak with the highest counts (bin size 0.002 G_0) to increase comparability. All measurements were performed at 300 K. The main conductance and the satellite peaks are marked with arrows. Inset: The low conductance regime on a logarithmic scale. a) Analysis of about 1.7×10^6 data points for the 16mer PA. The main conductance peak is located at $G_{PA16} = 0.05$ G_0. b) A 26mer molecule; 3×10^4 data points. The main peak is located at $G_{PA26} = 0.01$ G_0. (c) Histogram for a 36mer molecule; analysis of 2×10^6 data points. The main conductance peak is at $G_{PA36} = 0.007$ G_0.(Fig. taken from [119])
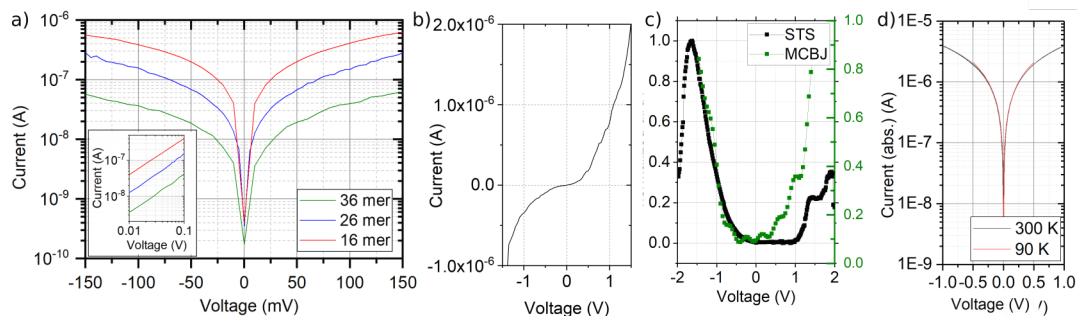
Figure 6.6: a) I-V curves for three molecular lengths taken at 300 K of the most stable configuration (marked with violet arrows in the histograms shown in Fig. 4). Inset: Linear power-law behavior. b) Asymmetric I-V curve as recorded in less than 5% of the measurements c) Comparison of the dI/dV characteristic of an asymmetric curve (as shown in b)) and a STM measurement. Due to the different types of contact the scale differs and is normalized for better visualization. The overall shape of the measurements is very similar. d) Temperature dependent I-V curves for a voltage range from -1 V to 1 V, exemplarily for 26mer. The characteristic does not change upon temperature change. The absolute value of the current is shown here, to highlight the symmetry of the current with respect to the polarity of the bias voltage.

The histograms show a large background compared to measurements of smaller molecules [287, 288]. Due to the length of the molecules, in the present case multiple molecular configurations in the junction are possible. Assuming PA molecules are attached to each Au contact, the configuration entropy is additionally enlarged.

In addition to the conductance measurements, I-V characteristics were recorded. By sweeping the voltage from -150 mV to 150 mV at the most stable configurations, deeper insight in the electron transport properties is gained. The used voltage and molecular length is expected to cause electric fields varying in between 10^5 and 10^6 V/cm. Despite the large intrinsic dipole of the molecule, measurements of the three molecules shows symmetric I-V curves in almost all cases, as shown in Fig. 6.6 a). Asymmetric I-V curves, as exemplarily shown for a measurement of a 36mer molecules in Fig. 6.6 b), are similar to those obtained by scanning tunneling spectroscopy [278] on SAM structures as shown in Fig. 6.6 c). The shape of the curves is very similar and indicates measurements on single molecules. Those type of curves were only observed in less than 5% of the measurements.

6.3 Discussion and the ratcheting model

The measurement results allow a wide range of analysis. In the following section, the dominant transport mechanism is determined, followed by propose of a model to explain the measurement data. Energetic considerations regarding the tunneling barrier and an internal and external Stark effect complement this discussion.

6.3.1 Determination of the dominant transport mechanism

The dipole moment of the used molecules is a result of the helical assembly of CO and NH_3 sites within the polypeptide units. The pairing and the accompanying interdigitation of these molecules, as seen in STM [278], are most likely mediated by the formation of hydrogen bonds. Nevertheless, the helical structure is maintained as seen in STM.

Scanning tunnelling spectroscopy (STS) experiments have shown that there is no density of states in the low-bias regime at E_F for the case of single molecules [278]. Therefore the electronic transmission around zero bias is extremely low. In general, transport through molecules can be often described by elastic tunneling, as described in Sec. 2.4.3, where the conductance is given by the universal quantum conductance G_0 weighted by the transmission for each channel. The preexponential factor according to this model is around $0.25\,G_0$ for our measurements, which is reasonably close to the value expected for a perfect quantum point contact [88, 289].

In accordance to that, electronic tunneling is expected to be the dominant transport channel. The basic transport mechanisms through organic molecules and their significant characteristics are explained in more detail in Sec. 2.4. The I-V characteristics show a linear power-law behavior in the low-voltage regime, as shown in the inset of Fig. 6.6 a). This means the current is almost directly proportional to the voltage ($I \propto V^{1.1}$) for a fixed distance. This behavior is expected for elastic tunneling as described in further detail in Sec. 2.4.1.

The conductivity found for PA is comparably high with respect to other biomolecules [290–292], which might be explained by the chirality of the molecule. CISS related studies found that for one electron spin, which means half of a non polarised current, long-range and efficient electron transport is expected [293]. This finding for chiral molecules is in qualitatively accordance with the high conductance values found here.

This assumption is substantiated by temperature dependent measurements, which are shown exemplarily for a 26mer molecule in Fig. 6.6 d). The measurements at 300 K and 90 K look almost the same, thus activated transport in this temperature regime is negligible. This further indicates electron tunneling along the PA molecules as the dominant transport mechanism.

Within the Landauer Theory the conductance G can be modelled as a function of the effective length L as $G(L) \propto e^{-\beta \cdot L}$. The decay constant β is specific for the analyzed molecule. For example, for tryptophan and conjugated molecules decay constants of 5.8 and 4 ± 2 nm^{-1} were found respectively [85, 86, 286, 288], while measurements on alkane based molecules revealed values between $\beta = 7\,\mathrm{nm}^{-1}$ and $\beta = 11\,\mathrm{nm}^{-1}$. The effective length is not mandatorily the length of the molecule. To apply the model to the conductance measurements, molecular configurations need to be considered.
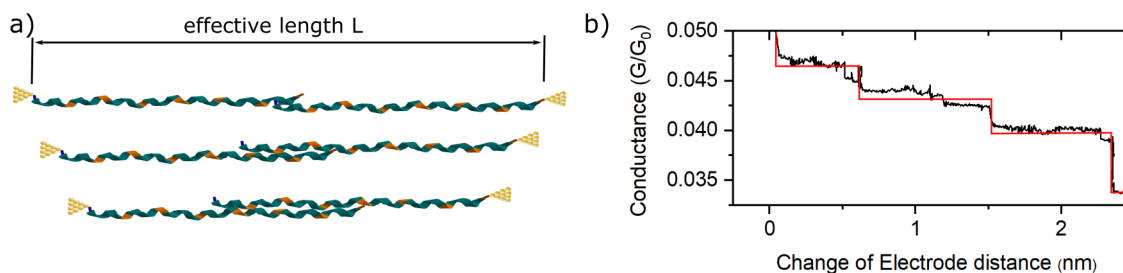
Figure 6.7: a) Illustration of the ratcheting of two interdigitated PA molecules with different effective lengths L. b) Change in the conductance versus the electrode distance for a 16mer molecule. The plateau length of 0.7–0.8 nm fits nicely to the lengths of five monomers [AAAAK] as sketched in a) for a 36mer PA.

6.3.2 Molecular configurations: The ratcheting model

For molecules implying a large dipole, asymmetric I-V characteristic are expected. The symmetric I-V curves measured here can be explained by the possible interdigitation of two molecules. Each of the molecules chemisorbs on one contact via the thiole bond formed by the lysine terminated side of the peptide. Based on the accompanying STM study, the molecules are expected to form a SAM on the Au nanoconstriction. Therefore it is likely that during the break of the junction, molecules lean in between the electrodes from both sides. Due to this formation, two molecules with opposing dipoles lay beside each other within the junction as schematically drawn in Fig 6.7 a). In such a scenario the overall dipole is significantly reduced. Only one enantiomer is present in the molecular solution used in this experiment, this means interdigitation, as observed in STM measurements [277] between adjacent molecules is still feasible and will stabilize certain molecular configurations. When the electrode distance is changed, the periodicity of the molecular sequence leads to stable positions at specific overlap values, which correspond to a number of [AAAK] units.

To underline this concept, the conductance as a function of electrode distance for a 16mer molecule is shown in Fig. 6.7 b). The electrode distance was calculated from the motor position, corrected by the reduction factor of the system. Steps of about 0.7-0.8 nm occur, corresponding nicely with the 0.75 nm [AAAAK] unit length of the polypeptides. The configuration with the highest probability, is a head-to-head configuration with an overlap of 0.75 nm, or rather one [AAAAK] unit, to provide an effective current transmission. This changes for smaller effective lengths during the closing cycles, were the overlap is increased. The corresponding molecular configurations are schematically shown in Fig 6.7 b) for a 36mer molecule.

This analysis leads to the conclusion of various two-molecule assemblies that are stabilized by interdigitation. Ratcheting takes place during the opening and closing cycles, triggered by the periodicity of the molecules.

Relating those considerations back to the statistical analysis of the conductance traces, all three molecular lengths show the same modulation in the histograms. To some extent, of cause other ratcheting configurations than the most probable ones are also likely, giving rise to the background in the histograms. In any case, the pronounced satellite peaks indicate an overlap by multiples of the unit length as most stable positions, which is in nice accordance
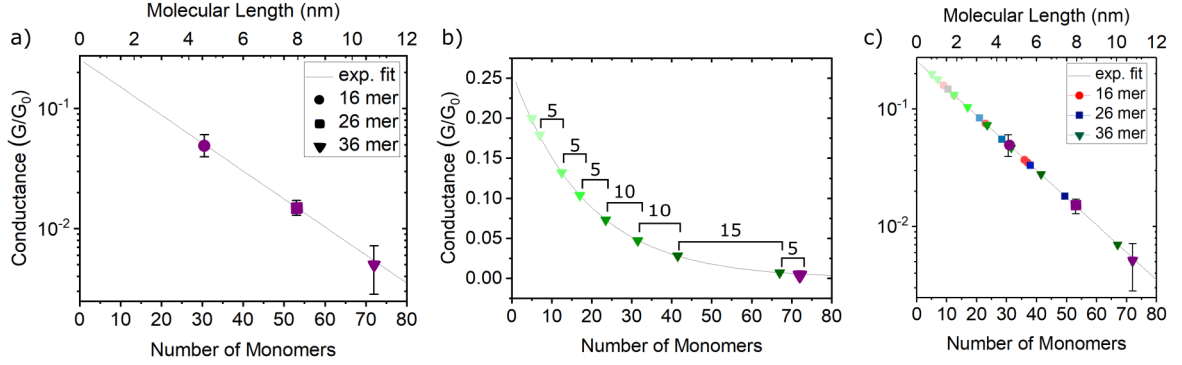
Figure 6.8: a) Exponential fit through the main conductance peaks for each of the three molecules. b) Conductance values for the peak positions found for the 36mer molecule as a function of the number of monomers. c) Data referring to the conductance values of the satellites shown in Fig. 6.5 were superimposed on the fit shown in a). This allows to determine the effective length of the molecule in the junction. (Fig. taken from [119])

with the proposed ratcheting model.

An exponential fit to the three intense conductance peaks from the histograms in Fig. 6.5 as a function of the molecular length L is shown in Fig 6.8 a). The main peaks, marked with violet arrows in the histograms, are assumed to correspond to a head-to-head configuration of two PA molecules. A decay constant of $\beta \approx 3.5 \text{nm}^{-1}$ is obtained, which is comparable with the reported values for conjugated molecules.

The satellite peaks found in the histograms were positioned on the tunneling curve generated from the main peaks to analyse the corresponding effective molecular lengths. This corresponding lengths refer to integer values of monomers, as is depicted in more detail for the 36mer molecule in Fig. 6.8 b). As a matter of fact, the satellite peaks show a fivefold sequence periodicity, which matches exactly the five monomer [AAAAK] units of the polypeptide with a length of 0.75 nm. This periodicity nicely emphasizes the proposed ratcheting behaviour, which assumes stable configurations of two molecules which overlaps corresponding to those molecular building blocks.

6.3.3 Estimation of the tunneling barrier

To evaluate the barrier height for a tunneling process the I-V curves shown in Fig. 6.6 a) are further analyzed. The tunneling current can be reasonably parametrized by $\text{I} \propto \text{Ve}^{-2\kappa\text{L}}$. κ is determined by the electron mass m_e and the effective tunneling barrier height Φ^* via $\kappa = \sqrt{2\text{m}_\text{e}\Phi^*}/\hbar$. Assuming that the tunneling barrier is independent of the molecular length, it can be modeled from the difference in the I-V sets for two different molecules with different lengths L_1 and L_2 via

$$\Phi^* = \frac{\hbar^2}{8m_E} \times ln\frac{(I_1/I_2)^2}{(L_2-L_1)^2} \qquad (6.3.1)$$

The resulting barrier height determined from the ratio of the 36mer and the 16mer molecules (measurements shown in Fig. 6.8) is shown in Fig. 6.9. The effective length is the most prob-
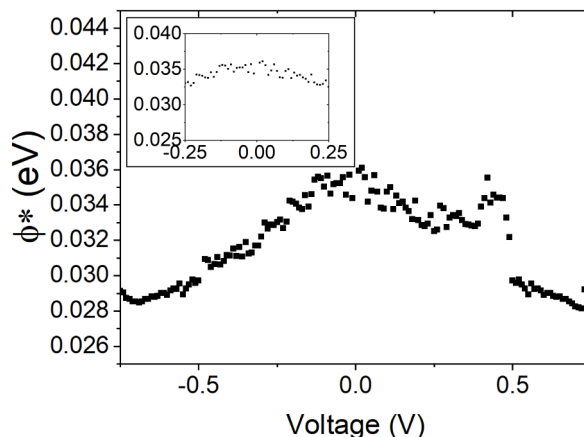
Figure 6.9: The effective barrier height Φ* calculated from the I-V curves in Fig. 6.6 for the 36mer
and 16mer PA molecules. Inset: Barrier height in the low-bias regime deduced from
different data sets.(Fig. adapted from [119])

able head-to-head configuration, according to the discussion above, two times the molecules
length corrected by the overlap of one [AAAAK] unit. In the low-bias regime the tunneling
barrier is constant for fields up to 10^5 V/cm. For large fields, the barrier starts to change.
For the low-bias regime in the range of -0.25 V to 0.25 V the barrier is constant at a value of
approx. 35 meV. For larger voltages the barrier starts to decrease. Unexpectedly no temper-
ature dependence is found for the electronic transport although the barrier height is in the
range of $k_b T$ at room temperature.

  Studies using molecular orbital theory reveal a gradual decrease of the gap with an increas-
ing electric field, for critical fields around 1×10^7 V/cm, for a 15mer polyalanine, [111]. The
so called Stark effect describes the shift of molecular states due to static, external electric
fields. This effect has already been observed for other biomolecules [294, 295]. The external
fields in the measurements shown in Fig. 6.5 are comparably low. Thus a renormalization
of the molecular electronic states due to an external Stark effect is negligible for low-bias
conductance measurements as shown here.

In the presented case, the molecular structure along the molecules is renormalized by the
strong interaction of the local electric field that comes along with pair configuration of the
molecules. Despite symmetric I-V curves resulting from the pairing, the dipole might not
necessarily be canceled. As concluded from the measurements here, the local dipole is still
present, giving rise to a strong renormalization due to internal electric fields. This trend may
be increased by additional intermolecular hydrogen bonds. Besides this internal Stark effect,
it is shown that external fields effects exceeding 5×10^5 V/cm change the molecular orbital
structure [111].

An study by Christancho et al. published in 2010 [**Christancho2010**], indicates an increase
of the external field by roughly a factor of 5 which reduces the effective barrier height by 30 %
. The determined tunneling barrier for PA molecules is smaller by one order of magnitude
compared to other systems. This means the molecular fields causing the internal Stark shift as
observed in this work, should be larger by a factor of 10^3 to 10^4 compared to the external ones.

6.4 Chapter conclusion

The electron transport through polyalanine based peptides of various lengths was studied via MCBJ. Analysis of length dependence and I-V characteristics, point to electron tunneling as the dominant transport mechanism.

Statistical analysis of conductance traces was performed and and revealed regularly spread satellite peaks next to the main conductance peaks. The intermolecular interaction and the peptide sequence lead to a locking of the PA assembly inside the junction at multiples of the [AAAAK] units. A ratcheting effect during the opening and closing of the junction is proposed, explaning the presence of multiple stable configurations inside the junction and causing the presence of satellite peaks in the histograms. The conductance values of the used molecules were determined to be $0.007\,G_0$, $0.01\,G_0$ and $0.05\,G_0$ for peptide sequences containing 16, 26 or 26 monomers respectively.

The high conductance through the molecules is reflected by the small reduction factor of $\beta = 3.5$ nm^{-1}. This is in agreement with the low apparent tunneling barrier of $35\,\mathrm{meV}$. A temperature dependence of electronic transport is not found but would be expected for tunneling barriers in the range of $k_B T$ at room temperature. This discrepancy could not be addressed within this work and remains a question for following studies. I-V measurements from $90\,\mathrm{K}$ to $300\,\mathrm{K}$ show no temperature dependence and exclude hopping transport as an effective mechanism.

Within the framework of nonresonant tunneling, the transmission probability depends exponentially on the molecular lengths. The reduction factor for saturated molecules is usually in the range of 7-11 nm^{-1} [79] and therefore significantly larger than the one measured for the PA molecules within this study. This indicates a smaller electronic gap structure.

For proteins, like DNA, a two-channel model including tunneling as well as hopping is even more appropriate [106] to describe the electron transport through this systems. For larger molecules, where donor-bridge-acceptor configurations come into play, the hopping transport can better be describes by Marcus theory, where the conductance is related to the electron transfer rate k_{ET}. Linear dependence is expected for off-resonant tunneling and sequential hopping. The coupling strengths in our case are not known, but this theoretical approach combining hopping and tunneling might lead to more detailed understanding of the transport mechanism in future analysis.

Chemisorbed molecules at both Au contacts are assumed, resulting in symmetric I-V curves. The presence of the molecular dipole and the interdigitation process leads to molecular fields introducing an internal Stark effect. Large external fields exceeding $5 \times 10^5\,\mathrm{V/cm}$ additionally change the molecular orbital structure. However, to understand these findings regarding electron transport, further calculations including configuration aspects of peptide sequences are necessary.

A detailed measurement series investigating the transport properties of single PA molecules was performed. Based on the analysis, a model was proposed explaining the transport properties of this polypeptides in regard to their geometrical configuration within the electrodes. This new finding provides an important stepping stone towards the understanding of electron transport through biomolecules. Regarding the CISS effect, measurements using magnetic contacts could be used in future measurements to investigate the behavior.

Part III

Conclusion

Conclusion

7.1 Summary

The electronic structure of two-dimensional graphene is known to be (very) sensitive to the presence of other specimen in close vicinity. In this context the sensoring properties of graphene for molecular and hydrogen co-/adsorption is investigated the first research topic. The second topic considers one-dimensional carbon fibers and two dimensional graphene flakes accumulated in fabric-like compound materials. Electronic conductivity has been found to depend significantly on the orientation of the microscopic building block and their internal properties.

Finally, single molecule conductivity is investigated by means of mechanically controlled break junction measurements as the third research topic.

Adsorption of atomic and molecular species on graphene

The inert character of extended 2D graphene prevents a flexible functionalization of graphene. Highly reactive atomic hydrogen is utilized to break this inertness, allowing the electronic transport properties to be tailored. Atomic hydrogen was found to induce a metal-insulator transition (MIT) on monolayer graphene (MLG) and quasi-freestanding monolayer graphene (QFMLG) even for extremely low coverages below $1\,\%$ ML. The metallic transport of pristine graphene is replaced by variable range hopping (VRH) upon hydrogenation as shown by temperature dependent measurements. The resistance increased by several orders of magnitude for the measured H-coverages up to $0.008\,$ML. Hopping around and tunneling across the chemisorbed hydrogen centers were excluded and localization effects, described within the framework of Anderson localization, were found and confirmed by the coincidence of the localization lengths, the mean free paths and the coverage, with regard to clustering of the H atoms. The chemisorption of H and the concomitant sublattice symmetry breaking, result neither in a band insulator nor in a "bad metal". The very large Fermi-wavelengths of pristine

graphene get determined by the mean free path upon hydrogenation. The interaction of pristine and hydrogenated graphene with organic molecules was investigated exemplary for PbPc. While the transport through pristine graphene is not influenced by PbPc, a strong effect was observed for hydrogen-functionalized graphene. Here, the molecules completely annihilate the resistance increase introduced by H chemisorption. DFT calculations revealed a barrierless chemical reaction in between the N atoms of the PbPc molecules and the chemisorbed H atoms, restoring the transport properties of pristine graphene. An energy gain of 2.8 eV with respect to atomic hydrogen is found for the absorption of 4 H atoms to the N-atoms of PbPc. The reaction is amplified by the size of the PbPc molecules and the possible subsequent adsorption to all four N atoms of the molecule, inducing an extremely efficient annihilation process. This chemical reaction was experimentally observed for the first time in the scope of this thesis.

This proofs that graphene-based sensors selective to physisorbed molecules can be achieved. The presented analysis confirms a large sensitivity of around 10 ppm of functionalized graphene towards PbPC molecules.

Low dimensional carbon based materials

In the second experimental chapter, analysis of CNFs and a graphene-based compound material are presented. Main similarities between those two composite materials were found with regard to electric conductivity. A major influence on the properties is the degree of ordering inside the structure, which is true for both the internal crystallinity inside the microscopic building blocks as well as for the alignment of this units towards each other in the compound. The impact of graphitic plane alignment within the nanostructures to the macroscopic conductivity of the material was shown on CNFs. Templating of the structure with CNT as well as external creep stress result in an improved alignment and enhanced conductivity of the structure. A strong dependence between the structural and electronic properties was revealed, the addition of nanocarbons therefore results not only in structural improvements but also in an enhanced conductivity. This improvements are not straight-forward additive and parasitic effects can start to play a role, e. g. the combination of carbon nanotube (CNT) templating and external creep stress in CNF results in a lower conductivity than the individual techniques.

The interplay between the microscopic alignment and the compound properties was illuminated by experiment and theory on a graphene-based conductor material. Graphene flakes resemble perfect microscopic building block and can be easily tuned with regard to their size and number of layers [36, 37, 69], providing very defined components for compound materials. Probe distance dependent measurements on such compounds revealed characteristic dimensions: while spacings significantly larger than the size of the microscopic building block allowed to treat the material as two-dimensional (2D) and isotropic, measurements at the scale of the building blocks reveal details about the assembly. These have been used as input for simulations. The complete conductivity tensor, combining the mesoscopic properties of the building block and the macroscopic ones of the compound material can not be accessed by experiment alone. The grain boundaries between the individual building blocks act as scattering centers or barriers, allowing electrons only to pass by via tunneling or hopping

transport. The co-existence of these two transport mechanisms requires a rather complex description of the materials properties. On a macroscopic scale, effects originating from the exact configuration of the nanoscale units average out, but a detailed understanding of electron transport through composite materials requires an exact knowledge of these influences. An approach for combining the macroscopic and microscopic transport properties to achieve the complete conductivity tensor by a combination of experiment and simulation was presented in this thesis. This is a crucial first step for material optimization with regard to possible applications like sensing or energy storage.

Transport through single helical molecules

Electron transport through chiral polyalanine molecules was investigated by means of MCBJ. Length dependent measurements revealed electron tunneling as the dominant transport mechanism with conductance values between $0.007\,G_0$ and $0.01\,G_0$ for molecular lengths between $2.6\,\mathrm{nm}$ and $5.4\,\mathrm{nm}$. The reduction factor is determined to $3.5\,\mathrm{nm}^{-1}$ and is in good agreement with the determined low tunneling barrier of $40\,\mathrm{meV}$. This large conductance values are counter intuitive, regarding the length of the molecules. The electrode distance of several nanometers makes direct tunneling an unlikely mechanism to reach the determined high conductance values. A process including several molecular states und multiple charge carriers could explain this behavior, but is not accessible by experiment. The energetic structure of the molecule is changed in presence of charge carriers and induce space charge effects. A theoretical appraoch by density functional theory (DFT) or the non-equilibrium greens function formalism can be a possibility to identify those effects and mechanisms. Additionally, intermolecular effects are found in transport measurements and scanning tunnelling microscope (STM) studies, which means the rotational ordering needs to be considered in application and research study design. Molecules are expected to chemisorb at both Au contacts and induce an interdigitation process, which results in symmetric I-V curves. The interdigitation combined with molecular dipol moments induce an internal Stark effect in the system. Based on this, a model explaining the observed transport properties in regard to their geometrical configuration between the contacts is proposed.

7.2 Outlook

Multiple carbon-based materials were investigated in the scope of this thesis. For all these materials, fundamental understanding of the electron transport is crucial to exploit their full application potential. The transfer of graphenes extraordinary properties towards macroscopic applications can be made possible by the use of compound materials. These already started to be used by industrial companies, like Bosch. Macroscopic graphene-based conductors provide not only weight savings but are also very cost-efficient, with prices nearly one order of magnitude below copper. To optimize these materials and exploit their range of usability, tailoring of the properties to a special use is needed. This can be e.g. achieved by intercalation or doping techniques [245, 247]. The presented way to determine the conductivity tensor of such materials can be used for a large number of materials and allow a comparison between those. The conductivity tensor can be used as a reference to qualify, describe

and compare novel or tuned materials. Besides, the exact influence of alignments, crossings and a detailed descriptions of the different transport mechanisms still needs to be considered and quantified in future investigations to complete the description of electron transport through carbon-based materials. Graphene is a well established material for a wide range of research questions and applications. Functionalization is needed to transfer this to sensor questions and studies. Hydrogenation of graphene is a suitable functionalization method to break the inert character and achieve a sensitivity towards physisorbed molecules like PbPc. The chemical reaction was found to be barrier-free by DFT calculations. Surprisingly, to the knowledge of the author, the reaction between H atoms and the N atom of the PbPc molecule are not investigated experimentally and almost no theoretical studies were performed until now. In the scope of this work, the interaction of PbPc with H functionalized graphene was proven. This reaction is expected to occur for other metallic Pc molecules as well but is not investigated yet. An experimental approach to further investigate this behavior cav be the direct observation of the reaction by STM Further analysis of the underlying chemical reaction might bring forth other material combinations showing a similar behavior. Also, graphene-based applications, sensitive to other specimen can be developed.

Molecular electronics, using biomolecules and their exceptional properties like spin selective electron transfer is just beginning to develop and still far away from industrial usage. But the CISS effect has already shown its potential in applications [47]. To exploit the possibilities, the effect itself and the concomitant electron transfer through chiral molecules needs to be completely understood. While the physical background of the CISS effect was puzzling at first, there is now a broadly accepted theoretical explanation. However, there are still differences between theory and experiment that need to be solved. This means, the electron transport through biomolecules needs to be further investigated, with respect to co-existance of different transport mechanisms or configurational aspects. Furthermore, intermolecular effects start to play a role and need to be carefully considered for the possible application development. To completely understand the findings presented in the scope of this work, theoretical investigations including the configuration aspects of the peptide sequence are needed. From the experimental side, simultaneous investigation of the spin selectivity and the electron transport properties of the molecules are possible with measurements using magnetic contacts.

Fundamental understanding is the first step on the way towards new electronic applications. Carbon-based materials are found in all states of application development, ranging from market-ready industrial purposes to proof of concept devices in research studies and will continue to grow in importance in the next years. Based on the findings of this work, new uses of carbon-based materials become possible, especially sensor applications show promising prospects for the future after silicon-based electronics.

Part IV

Appendix

Bibliography

[1]   J. B. Williams. "The Electronics Revolution". In: *The Electronics Revolution.* Springer International Publishing, 2017, pp. 270–274. DOI: `10.1007/978-3-319-49088-5_29`.

[2]   B. H. McCarthy and S. Ponedal. *IBM Unveils World's First 2 Nanometer Chip Technology, Opening a New Frontier for Semiconductors.* 2021.

[3]   B. Hoeneisen and C. A. Mead. "Fundamental limitations in microelectronics-I. MOS technology". In: *Solid State Electronics* 15.7 (1972), pp. 819–829. ISSN: 00381101. DOI: `10.1016/0038-1101(72)90103-7`.

[4]   M. Schulz. *The end of the road for silicon?* 1999. DOI: `10.1038/21526`.

[5]   C. MacK. *The Multiple Lives of Moore's Law.* 2015. DOI: `10.1109/MSPEC.2015.7065415`.

[6]   J. Shalf. *The future of computing beyond Moore's Law.* 2020. DOI: `10.1098/rsta.2019.0061`.

[7]   E. H. Falcao and F. Wudl. "Carbon allotropes: beyond graphite and diamond". In: *Journal of Chemical Technology & Biotechnology* 82.6 (2007), pp. 524–531. ISSN: 02682575. DOI: `10.1002/jctb.1693`.

[8]   S. Nasir, M. Z. Hussein, Z. Zainal, and N. A. Yusof. *Carbon-based nanomaterials/allotropes: A glimpse of their synthesis, properties and some applications.* 2018. DOI: `10.3390/ma11020295`.

[9]   A. Hirsch. *The era of carbon allotropes.* 2010. DOI: `10.1038/nmat2885`.

[10] Y. A. Kim, T. Hayashi, M. Endo, and M. S. Dresselhaus. "Carbon nanofibers". In: *Springer Handbook of Nanomaterials.* Springer, Berlin, Heidelberg, 2013, pp. 233–262. ISBN: 9783642205958. DOI: `10.1007/978-3-642-20595-8_7`.

[11] S. Jalali-Asadabadi et al. "Electronic Structure of Crystalline Buckyballs: fcc-C60". In: *Journal of Electronic Materials* 45.1 (2016), pp. 339–348. DOI: `10.1007/S11664-015-4080-2`.

[12] A. H. Castro Neto. "The carbon new age". In: *Materials Today* 13.3 (2010), pp. 12–17. ISSN: 1369-7021. DOI: 10.1016/S1369-7021(10)70029-8.

[13] K. S. Novoselov et al. "Electronic properties of graphene". In: *physica status solidi (b)* 244.11 (2007), pp. 4106–4111. ISSN: 1521-3951. DOI: 10.1002/PSSB.200776208.

[14] S. S. Batsanov. "Size effect in the structure and properties of condensed matter". In: *Journal of Structural Chemistry 2011 52:3* 52.3 (2011), pp. 602–615. ISSN: 1573-8779. DOI: 10.1134/S0022476611030231.

[15] E. Roduner. "Size matters: Why nanomaterials are different". In: *Chemical Society Reviews* 35.7 (2006), pp. 583–592. ISSN: 14604744. DOI: 10.1039/b502142c.

[16] X. Zhuang et al. *Two-dimensional soft nanomaterials: A fascinating world of materials.* 2015. DOI: 10.1002/adma.201401857.

[17] E. Pomerantseva et al. "Energy storage: The future enabled by nanomaterials". In: *Science* 366.6468 (2019). ISSN: 0036-8075. DOI: 10.1126/SCIENCE.AAN8285.

[18] S.-J. Park et al. "Review—A Review of Advanced Electronic Applications Based on Carbon Nanomaterials". In: *ECS Journal of Solid State Science and Technology* 9.7 (2020), p. 071002. ISSN: 2162-8777. DOI: 10.1149/2162-8777/abb035.

[19] B. R. C. D. Menezes et al. *Recent advances in the use of carbon nanotubes as smart biomaterials.* 2019. DOI: 10.1039/c8tb02419g.

[20] L. M. Peng, Z. Zhang, and C. Qiu. "Carbon nanotube digital electronics". In: *Nature Electronics* 2.11 (2019), pp. 499–505. ISSN: 25201131. DOI: 10.1038/s41928-019-0330-2.

[21] S. Yoon et al. "Carbon nanotubes embedded poly(3,4-ethylenedioxythiophene):poly(styrenesulfonate) hybrid hole collector for inverted planar perovskite solar cells". In: *Journal of Power Sources* 435 (2019), p. 226765. ISSN: 03787753. DOI: 10.1016/j.jpowsour.2019.226765.

[22] K. E. Kitko and Q. Zhang. *Graphene-based nanomaterials: From production to integration with modern tools in neuroscience.* 2019. DOI: 10.3389/fnsys.2019.00026.

[23] J. Y. Jeon and T. J. Ha. "Waterproof Electronic-Bandage with Tunable Sensitivity for Wearable Strain Sensors". In: *ACS Applied Materials and Interfaces* 8.4 (2016), pp. 2866–2871. ISSN: 19448252. DOI: 10.1021/acsami.5b12201.

[24] X. Li et al. "Carbon and Graphene Quantum Dots for Optoelectronic and Energy Devices: A Review". In: *Advanced Functional Materials* 25.31 (2015), pp. 4929–4947. ISSN: 16163028. DOI: 10.1002/adfm.201501250.

[25] K. S. Novoselov et al. "Electric field in atomically thin carbon films". In: *Science* 306.5696 (2004), pp. 666–669. ISSN: 00368075. DOI: 10.1126/science.1102896.

[26] A. H. Castro Neto et al. "The electronic properties of graphene". In: *Reviews of Modern Physics* 81.1 (2009), pp. 109–162. ISSN: 00346861. DOI: 10.1103/RevModPhys.81.109. arXiv: 0709.1163.

[27] F. Schedin et al. "Detection of individual gas molecules adsorbed on graphene". In: *Nature Materials* 6.9 (2007), pp. 652–655. ISSN: 14761122. DOI: 10.1038/nmat1967.

[28] T. Kuila et al. "Chemical functionalization of graphene and its applications". In: *Progress in Materials Science* 57.7 (2012), pp. 1061–1105. ISSN: 0079-6425. DOI: 10.1016/J.PMATSCI.2012.03.002.

[29] D. W. Boukhvalov and M. I. Katsnelson. "Chemical functionalization of graphene". In: *Journal of Physics: Condensed Matter* 21.34 (2009), p. 344205. ISSN: 0953-8984. DOI: 10.1088/0953-8984/21/34/344205.

[30] Huai-Ping Cong, Jia-Fu Chen, and Shu-Hong Yu. "Graphene-based macroscopic assemblies and architectures: an emerging material system". In: *Chemical Society Reviews* 43.21 (2014), pp. 7295–7325. DOI: 10.1039/C4CS00181H.

[31] M. Li and J. Lian. "Microstructure Dictating Performance: Assembly of Graphene-Based Macroscopic Structures". In: *Accounts of Materials Research* 2.1 (2020), pp. 7–20. DOI: 10.1021/ACCOUNTSMR.0C00053.

[32] R. A. Matula. "Electrical resistivity of copper, gold, palladium, and silver". In: *Journal of Physical and Chemical Reference Data* 8.4 (1979), pp. 1147–1298. ISSN: 15297845. DOI: 10.1063/1.555614.

[33] M. Köhne and L. Rizzi. *Can graphene compete with copper in electrical conductivity? | Bosch Global.* 2021.

[34] R. Raccichini, A. Varzi, S. Passerini, and B. Scrosati. "The role of graphene for electrochemical energy storage". In: *Nature Materials 2014 14:3* 14.3 (2014), pp. 271–279. ISSN: 1476-4660. DOI: 10.1038/nmat4170.

[35] D. Li and R. B. Kaner. *Materials science: Graphene-based materials.* 2008. DOI: 10.1126/science.1158180.

[36] L. Rizzi et al. "Electrical Conductivity Modeling of Graphene-based Conductor Materials". In: *ACS Applied Materials and Interfaces* 10.49 (2018), pp. 43088–43094. ISSN: 19448252. DOI: 10.1021/acsami.8b16361.

[37] L. Rizzi et al. "Quantifying the influence of graphene film nanostructure on the macroscopic electrical conductivity". In: *Nano Express* 1.2 (2020), p. 020035. DOI: 10.1088/2632-959x/abb37a.

[38] B. Fang, D. Chang, Z. Xu, and C. Gao. "A Review on Graphene Fibers: Expectations, Advances, and Prospects". In: *Advanced Materials* 32.5 (2020), p. 1902664. ISSN: 0935-9648. DOI: 10.1002/adma.201902664.

[39] L. Zhang et al. *A review: Carbon nanofibers from electrospun polyacrylonitrile and their applications.* 2014. DOI: 10.1007/s10853-013-7705-y.

[40] L. Feng et al. "Carbon Nanofibers and Their Composites: A Review of Synthesizing, Properties and Applications". In: *Materials* 7.5 (2014), pp. 3919–3945. ISSN: 1996-1944. DOI: 10.3390/ma7053919.

[41] T. Maitra et al. "Improved graphitization and electrical conductivity of suspended carbon nanofibers derived from carbon nanotube/polyacrylonitrile composites by directed electrospinning". In: *Carbon* 50.5 (2012), pp. 1753–1761. ISSN: 00086223. DOI: 10.1016/j.carbon.2011.12.021.

[42] Y. Zhang, K. Song, J. Meng, and M. L. Minus. "Tailoring polyacrylonitrile interfacial morphological structure by crystallization in the presence of single-wall carbon nanotubes". In: *ACS Applied Materials and Interfaces* 5.3 (2013), pp. 807–814. ISSN: 19448244. DOI: 10.1021/am302382m.

[43] L. J. Lanticse-Diaz et al. "The effect of nanotube alignment on stress graphitization of carbon/carbon nanotube composites". In: *Carbon* 47.4 (2009), pp. 974–980. ISSN: 00086223. DOI: 10.1016/j.carbon.2008.11.046.

[44] V. Hamelbeck et al. "Spin Selectivity in Electron Transmission Through Self-Assembled Monolayers of Double-Stranded DNA". In: *Science* 331.6019 (2011), pp. 894–897. ISSN: 0036-8075. DOI: https://doi.org/10.1126/science.1199339. arXiv: 20.

[45] Z. Xie et al. "Spin specific electron conduction through DNA oligomers". In: *Nano Letters* 11.11 (2011), pp. 4652–4655. ISSN: 15306984. DOI: 10.1021/nl2021637.

[46] R. Naaman and D. H. Waldeck. "Spintronics and Chirality: Spin Selectivity in Electron Transport Through Chiral Molecules." In: *Annual review of physical chemistry* 66.January (2015), pp. 263–281. ISSN: 1545-1593. DOI: 10.1146/annurev-physchem-040214-121554.

[47] O. Ben-Dor, S. Yochelis, I. Felner, and Y. Paltiel. "Unusual magnetic behavior in a chiral-based magnetic memory device". In: *Journal of Magnetism and Magnetic Materials* 398 (2016), pp. 259–263. ISSN: 03048853. DOI: 10.1016/j.jmmm.2015.09.005.

[48] R. Naaman and D. H. Waldeck. "Chiral-induced spin selectivity effect". In: *Journal of Physical Chemistry Letters* 3.16 (2012), pp. 2178–2187. ISSN: 19487185. DOI: 10.1021/jz300793y.

[49] R. Naaman and Ron. "Chirality - Beyond the Structural Effects". In: *Israel Journal of Chemistry* 56.11-12 (2016), pp. 1010–1015. ISSN: 00212148. DOI: 10.1002/ijch.201600102.

[50] G. Bullard et al. "Low-Resistance Molecular Wires Propagate Spin-Polarized Currents". In: *Journal of the American Chemical Society* 141.37 (2019), pp. 14707–14711. ISSN: 15205126. DOI: 10.1021/jacs.9b06142.

[51] P. Drude. "Zur Elektronentheorie der Metalle". In: *Annalen der Physik* 306.3 (1900), pp. 566–613. ISSN: 00033804. DOI: 10.1002/andp.19003060312.

[52] A Sommerfeld. *Zur Elektronentheorie der Metalle auf Grund der Fermischen Statistik. I. Teil: Allgemeines, Strömungs- und Austrittsvorgänge.* Tech. rep.

[53] R. Gross and A. Marx. *Festkörperphysik.* De Gruyter Oldenbourg, 2014. DOI: 10.1524/9783110358704.

[54] S. Datta. *Electronic Transport in Mesoscopic Systems.* Cambridge University Press, 1995. DOI: 10.1017/cbo9780511805776.

[55] M. Büttiker. "Four-terminal phase-coherent conductance". In: *Physical Review Letters* 57.14 (1986), pp. 1761–1764. ISSN: 00319007. DOI: 10.1103/PhysRevLett.57.1761.

[56]   M. Büttiker. "SYMMETRY OF ELECTRICAL CONDUCTION." In: *IBM Journal of Research and Development* 32.3 (1988), pp. 317–334. ISSN: 00188646. DOI: `10.1147/rd.323.0317`.

[57]   M. Büttiker. "Role of quantum coherence in series resistors". In: *Physical Review B* 33.5 (1986), pp. 3020–3026. ISSN: 01631829. DOI: `10.1103/PhysRevB.33.3020`.

[58]   I. Miccoli, F. Edler, H. Pfnür, and C. Tegenkamp. "The 100th anniversary of the four-point probe technique: The role of probe geometries in isotropic and anisotropic systems". In: *Journal of Physics Condensed Matter* 27.22 (2015). ISSN: 1361648X. DOI: `10.1088/0953-8984/27/22/223201`.

[59]   J. Albers and H. L. Berkowitz. "An Alternative Approach to the Calculation of Four-Probe Resistances on Nonuniform Structures". In: *Journal of The Electrochemical Society* 132.10 (1985), pp. 2453–2456. ISSN: 0013-4651. DOI: `10.1149/1.2113598`.

[60]   S. Zolfaghar Tehrani, W. L. Lim, and L. Lee. "Correction factors for films resistivity measurement". In: *Measurement: Journal of the International Measurement Confederation* 45.3 (2012), pp. 219–225. ISSN: 02632241. DOI: `10.1016/j.measurement.2011.11.019`.

[61]   W. Versnel. "Electrical characteristics of an anisotropic semiconductor sample of circular shape with finite contacts". In: *Journal of Applied Physics* 54.2 (1983), pp. 916–921. ISSN: 00218979. DOI: `10.1063/1.332054`.

[62]   A. Mircea. "Semiconductor sheet resistivity measurements on square samples". In: *Journal of Scientific Instruments* 41.11 (1964), pp. 679–681. ISSN: 09507671. DOI: `10.1088/0950-7671/41/11/307`.

[63]   J. Wasscher. "Electrical transport phenomena in MnTe, an antiferromagnetic semiconductor". In: (1969). DOI: `10.6100/IR43336`.

[64]   L. J. van der PAUW. "A METHOD OF MEASURING SPECIFIC RESISTIVITY AND HALL EFFECT OF DISCS OF ARBITRARY SHAPE". In: *Semiconductor Devices: Pioneering Papers*. WORLD SCIENTIFIC, 1991, pp. 174–182. DOI: `10.1142/9789814503464_0017`.

[65]   P. Bøggild et al. *Mapping the electrical properties of large-area graphene.* 2017. DOI: `10.1088/2053-1583/aa8683`.

[66]   A. V. Melnikov, M. Shuba, and P. Lambin. "Modeling the electrical properties of three-dimensional printed meshes with the theory of resistor lattices". In: *Physical Review E* 97.4 (2018), p. 043307. ISSN: 24700053. DOI: `10.1103/PhysRevE.97.043307`.

[67]   C. O'Callaghan et al. "Effective medium theory for the conductivity of disordered metallic nanowire networks". In: *Physical Chemistry Chemical Physics* 18.39 (2016), pp. 27564–27571. ISSN: 14639076. DOI: `10.1039/c6cp05187a`.

[68]   F. Dalmas et al. "Carbon nanotube-filled polymer composites. Numerical simulation of electrical conductivity in three-dimensional entangled fibrous networks". In: *Acta Materialia* 54.11 (2006), pp. 2923–2931. ISSN: 13596454. DOI: `10.1016/j.actamat.2006.02.028`.

[69] L. Rizzi et al. "Computationally efficient simulation method for conductivity modeling of 2D-based conductors". In: *Computational Materials Science* 161 (2019), pp. 364–370. ISSN: 09270256. DOI: 10.1016/j.commatsci.2019.02.022.

[70] P. W. Anderson. "Absence of diffusion in certain random lattices". In: *Physical Review* 109.5 (1958), pp. 1492–1505. ISSN: 0031899X. DOI: 10.1103/PhysRev.109.1492.

[71] N. F. Mott, W. D. Twose, and W. D. Twose∼. "The theory of impurity conduction". In: *Advances in Physics* 10.38 (1961), pp. 107–163. ISSN: 1460-6976. DOI: 10.1080/00018736100101271.

[72] B. L. Ioffe. *LIMITS OF APPLICABILITY OF THE WEAK-INTERACTION THEORY*. Tech. rep. 5. 1960, pp. 1608–1614.

[73] N. F. Mott. "Metal-insulator transitions". In: *Contemporary Physics* 14.5 (1973), pp. 401–413. ISSN: 00234753. DOI: https://doi.org/10.1080/00107517308210764.

[74] N. F. N. F. Mott and E. A. E. A. Davis. *Electronic processes in non-crystalline materials*. 2d ed. Oxford ;New York: Clarendon Press, 1979, p. 590. ISBN: 9780198512882.

[75] E. Abrahams, P. W. Anderson, D. C. Licciardello, and T. V. Ramakrishnan. "Scaling theory of localization: Absence of quantum diffusion in two dimensions". In: *Physical Review Letters* 42.10 (1979), pp. 673–676. ISSN: 00319007. DOI: 10.1103/PhysRevLett.42.673.

[76] M. H. Cohen, H. Fritzsche, and S. R. Ovshinsky. "Simple band model for amorphous semiconducting alloys". In: *Physical Review Letters* 22.20 (1969), pp. 1065–1068. ISSN: 00319007. DOI: 10.1103/PhysRevLett.22.1065.

[77] N. F. Mott and J. H. Davies. "Metal-insulator transition in doped semiconductors". In: *Philosophical Magazine B* (1968). ISSN: 1463-6417. DOI: 10.1080/01418638008222332.

[78] V. Ambegaokar, B. I. Halperin, and J. S. Langer. "Hopping conductivity in disordered systems". In: *Physical Review B* 4.8 (1971), pp. 2612–2620. ISSN: 01631829. DOI: 10.1103/PhysRevB.4.2612.

[79] H. B. Akkerman and B. de Boer. "Electrical conduction through single molecules and self-assembled monolayers". In: *Journal of Physics: Condensed Matter* 20.1 (2008), p. 013001. ISSN: 0953-8984. DOI: 10.1088/0953-8984/20/01/013001.

[80] M. Suzuki, S. Fujii, and M. Fujihira. "Measurements of currents through single molecules of alkanedithiols by repeated formation of break junction in scanning tunneling microscopy under ultrahigh vacuum". In: *Japanese Journal of Applied Physics, Part 1: Regular Papers and Short Notes and Review Papers* 45.3 B (2006), pp. 2041–2044. ISSN: 00214922. DOI: 10.1143/JJAP.45.2041.

[81] W. Haiss et al. "Measurement of single molecule conductivity using the spontaneous formation of molecular wires". In: *Physical Chemistry Chemical Physics* 6.17 (2004), pp. 4330–4337. ISSN: 14639076. DOI: 10.1039/b404929b.

[82] F. Chen et al. "Effect of anchoring groups on single-molecule conductance: Comparative study of thiol-, amine-, and carboxylic-acid-terminated molecules". In: *Journal of the American Chemical Society* 128.49 (2006), pp. 15874–15881. ISSN: 00027863. DOI: 10.1021/ja065864k.

[83] R. L. York, P. T. Nguyen, and K. Slowinski. "Long-range electron transfer through monolayers and bilayers of alkanethiols in electrochemically controlled Hg-Hg tunneling junctions". In: *Journal of the American Chemical Society* 125.19 (2003), pp. 5948–5953. ISSN: 00027863. DOI: `10.1021/ja0211353`.

[84] F. Milani et al. "Ultrathin π-Conjugated Polymer Films for Simple Fabrication of Large-Area Molecular Junctions". In: *ChemPhysChem* 8.4 (2007), pp. 515–518. ISSN: 14394235. DOI: `10.1002/cphc.200600672`.

[85] A. Shah et al. "Electron transfer in peptides". In: *Chemical Society Reviews* 44.4 (2015), pp. 1015–1027. ISSN: 0306-0012. DOI: `10.1039/C4CS00297K`.

[86] L. Sepunaru et al. "Electronic transport via homopeptides: The role of side chains and secondary structure". In: *Journal of the American Chemical Society* 137.30 (2015), pp. 9617–9626. ISSN: 15205126. DOI: `10.1021/jacs.5b03933`.

[87] J. G. Simmons. "Generalized Formula for the Electric Tunnel Effect between Similar Electrodes Separated by a Thin Insulating Film". In: *Journal of Applied Physics* 34.6 (1963), pp. 1793–1803. ISSN: 00218979. DOI: `10.1063/1.1702682`.

[88] J. C. Cuevas and E. Scheer. *Molecular Electronics*. Vol. 15. World Scientific Series in Nanoscience and Nanotechnology. WORLD SCIENTIFIC, 2017. ISBN: 978-981-322-602-9. DOI: `10.1142/10598`.

[89] C. R. Arroyo et al. "Influence of binding groups on molecular junction formation". In: *Journal of the American Chemical Society* 133.36 (2011), pp. 14313–14319. ISSN: 00027863. DOI: `10.1021/ja201861k`.

[90] K. Kanthasamy and H. Pfnür. "Conductance through single biphenyl molecules: Symmetric and asymmetric coupling to electrodes". In: *Beilstein Journal of Nanotechnology* 6.1 (2015), pp. 1690–1697. ISSN: 21904286. DOI: `10.3762/bjnano.6.171`.

[91] K. Wang and B. Xu. "Modulation and Control of Charge Transport Through Single-Molecule Junctions". In: *Topics in Current Chemistry* 375.1 (2017), p. 17. ISSN: 2365-0869. DOI: `10.1007/s41061-017-0105-z`.

[92] T. A. Su et al. "Chemical principles of single-molecule electronics". In: *Nature Reviews Materials* 1 (2016). ISSN: 20588437. DOI: `10.1038/natrevmats.2016.2`.

[93] C. Van Dyck and M. A. Ratner. "Molecular rectifiers: A new design based on asymmetric anchoring moieties". In: *Nano Letters* 15.3 (2015), pp. 1577–1584. ISSN: 15306992. DOI: `10.1021/nl504091v`.

[94] R. Frisenda et al. "Electrical properties and mechanical stability of anchoring groups for single-molecule electronics". In: *Beilstein Journal of Nanotechnology* 6.1 (2015), pp. 1558–1567. ISSN: 21904286. DOI: `10.3762/bjnano.6.159`.

[95] Z. Li, M. Smeu, M. A. Ratner, and E. Borguet. "Effect of Anchoring Groups on Single Molecule Charge Transport through Porphyrins". In: *The Journal of Physical Chemistry C* 117.29 (2013), pp. 14890–14898. ISSN: 1932-7447. DOI: `10.1021/jp309871d`.

[96] E. Leary et al. "Incorporating single molecules into electrical circuits. the role of the chemical anchoring group". In: *Chemical Society Reviews* 44.4 (2015), pp. 920–942. ISSN: 14604744. DOI: `10.1039/c4cs00264d`.

[97]   L. A. Zotti et al. "Revealing the role of anchoring groups in the electrical conduction through single-molecule junctions". In: *Small* 6.14 (2010), pp. 1529–1535. ISSN: 16136810. DOI: 10.1002/smll.200902227.

[98]   W. Sheng et al. "Quantum transport in alkane molecular wires: Effects of binding modes and anchoring groups". In: *Journal of Chemical Physics* 131.24 (2009). ISSN: 00219606. DOI: 10.1063/1.3276280.

[99]   G. Breit and E. Wigner. "Capture of slow neutrons". In: *Physical Review* 49.7 (1936), pp. 519–531. ISSN: 0031899X. DOI: 10.1103/PhysRev.49.519.

[100] R. Landauer. "Electrical resistance of disordered one-dimensional lattices". In: *Philosophical Magazine* 21.172 (1970), pp. 863–867. ISSN: 00318086. DOI: 10.1080/14786437008238472.

[101] A. Miller and E. Abrahams. "Impurity conduction at low concentrations". In: *Physical Review* 120.3 (1960), pp. 745–755. ISSN: 0031899X. DOI: 10.1103/PhysRev.120.745.

[102] E. M. Conwell. "Impurity band conduction in germanium and silicon". In: *Physical Review* 103.1 (1956), pp. 51–61. ISSN: 0031899X. DOI: 10.1103/PhysRev.103.51.

[103] N. F. Mott. "ON THE TRANSITION TO METALLIC CONDUCTION IN SEMI-CONDUCTORS". In: *Canadian Journal of Physics* 34.12A (1956), pp. 1356–1368. ISSN: 0008-4204. DOI: 10.1139/p56-151.

[104] F. Evers, R. Korytár, S. Tewari, and J. M. Van Ruitenbeek. "Advances and challenges in single-molecule electron transport". In: *Reviews of Modern Physics* 92.3 (2020), p. 035001. ISSN: 15390756. DOI: 10.1103/RevModPhys.92.035001. arXiv: 1906.10449.

[105] S. Lindsay. "Ubiquitous Electron Transport in Non-Electron Transfer Proteins". In: *Life* 10.5 (2020), p. 72. ISSN: 2075-1729. DOI: 10.3390/life10050072.

[106] A. Nitzan. "Electron transmission through molecules and molecular interfaces". In: *Annual Review of Physical Chemistry* 52.1 (2001), pp. 681–750. ISSN: 0066-426X. DOI: 10.1146/annurev.physchem.52.1.681.

[107] W. B. Davis, M. A. Ratner, and M. R. Wasielewski. "Dependence of electron transfer dynamics in wire-like bridge molecules on donor-bridge energetics and electronic interactions". In: *Chemical Physics* 281.2-3 (2002), pp. 333–346. ISSN: 03010104. DOI: 10.1016/S0301-0104(02)00444-5.

[108] L. Xiang et al. "Intermediate tunnelling–hopping regime in DNA charge transport". In: *Nature Chemistry* 7.3 (2015), pp. 221–226. ISSN: 1755-4330. DOI: 10.1038/nchem.2183.

[109] C. Lambert, G. Nöll, and J. Schelter. "Bridge-mediated hopping or superexchange electron-transfer processes in bis(triarylamine) systems". In: *Nature Materials* 1.1 (2002), pp. 69–73. ISSN: 14761122. DOI: 10.1038/nmat706.

[110] Y.-T. Long, E. Abu-Irhayem, and H.-B. Kraatz. "Peptide Electron Transfer: More Questions than Answers". In: *Chemistry - A European Journal* 11.18 (2005), pp. 5186–5194. ISSN: 0947-6539. DOI: 10.1002/chem.200500143.

[111] D. Cristancho and J. M. Seminario. "Polypeptides in alpha-helix conformation perform as diodes". In: *Journal of Chemical Physics* 132.6 (2010), p. 065102. ISSN: 00219606. DOI: 10.1063/1.3310387.

[112] R. Frisenda and H. S. Van Der Zant. "Transition from Strong to Weak Electronic Coupling in a Single-Molecule Junction". In: *Physical Review Letters* 117.12 (2016), p. 126804. ISSN: 10797114. DOI: 10.1103/PhysRevLett.117.126804.

[113] J. Baringhaus. "Mesoscopic transport phenomena in epitaxial graphene nanostructures : a surface science approach". PhD thesis. Hannover: Leibniz Universit"at Hannover, 2015. DOI: https://doi.org/10.15488/8404.

[114] J. M. van Ruitenbeek et al. "Adjustable nanofabricated atomic size contacts". In: *Review of Scientific Instruments* 67.1 (1996), pp. 108–111. ISSN: 00346748. DOI: 10.1063/1.1146558.

[115] E. H. Huisman et al. "Public exhibit for demonstrating the quantum of electrical conductance". In: *Science* 79.8 (2011), pp. 1–15. ISSN: 00029505. DOI: 10.1119/1.3593276. arXiv: 1103.3739.

[116] C. A. Martin, D. Ding, H. S. J. Van Der Zant, and J. M. Van Ruitenbeek. "Lithographic mechanical break junctions for single-molecule measurements in vacuum: Possibilities and limitations". In: *New Journal of Physics* 10 (2008). ISSN: 13672630. DOI: 10.1088/1367-2630/10/6/065008. arXiv: 0802.0629.

[117] B. Smith. "Fabricating and Measuring an Atomic Point Contact". In: (2006).

[118] S. A. G. Vrouwe et al. "Mechanics of lithographically defined break junctions". In: *Physical Review B - Condensed Matter and Materials Physics* 71.3 (2005), p. 035313. ISSN: 10980121. DOI: 10.1103/PhysRevB.71.035313.

[119] D. Slawig et al. "Electronic transport through single polyalanine molecules". In: *Physical Review B* 102.11 (2020), p. 115425. ISSN: 2469-9950. DOI: 10.1103/physrevb.102.115425.

[120] P. R. Wallace. "The band theory of graphite". In: *Physical Review* 71.9 (1947), pp. 622–634. ISSN: 0031899X. DOI: 10.1103/PhysRev.71.622.

[121] S Reich, J Maultzsch, C Thomsen, and P Ordejó. "Tight-binding description of graphene". In: *PHYSICAL REVIEW B* 66 (2002), p. 35412. DOI: 10.1103/PhysRevB.66.035412.

[122] L. Jiao et al. "Narrow graphene nanoribbons from carbon nanotubes". In: *Nature* 458.7240 (2009), pp. 877–880. ISSN: 00280836. DOI: 10.1038/nature07919.

[123] M. Choucair, P. Thordarson, and J. A. Stride. "Gram-scale production of graphene based on solvothermal synthesis and sonication". In: *Nature Nanotechnology* 4.1 (2009), pp. 30–33. ISSN: 17483395. DOI: 10.1038/nnano.2008.365.

[124] J. Wintterlin and M. L. Bocquet. "Graphene on metal surfaces". In: *Surface Science* 603.10-12 (2009), pp. 1841–1852. ISSN: 00396028. DOI: 10.1016/j.susc.2008.08.037.

[125] S. Park and R. S. Ruoff. "Chemical methods for the production of graphenes". In: *Nature Nanotechnology* 4.4 (2009), pp. 217–224. ISSN: 17483395. DOI: 10.1038/nnano.2009.58.

[126] S. Marchini, S. Günther, and J. Wintterlin. "Scanning tunneling microscopy of graphene on Ru(0001)". In: *Physical Review B - Condensed Matter and Materials Physics* 76.7 (2007), p. 075429. ISSN: 10980121. DOI: 10.1103/PhysRevB.76.075429.

[127] P. W. Sutter, J. I. Flege, and E. A. Sutter. "Epitaxial graphene on ruthenium". In: *Nature Materials* 7.5 (2008), pp. 406–411. ISSN: 14764660. DOI: 10.1038/nmat2166.

[128] S. Bae et al. "Roll-to-roll production of 30-inch graphene films for transparent electrodes". In: *Nature Nanotechnology* 5.8 (2010), pp. 574–578. ISSN: 17483387. DOI: 10.1038/nnano.2010.132.

[129] M. H. Rümmeli et al. "On the role of vapor trapping for chemical vapor deposition (CVD) grown graphene over copper". In: *Chemistry of Materials* 25.24 (2013), pp. 4861–4866. ISSN: 15205002. DOI: 10.1021/cm401669k.

[130] M. H. Rümmeli et al. "Direct low-temperature nanographene cvd synthesis over a dielectric insulator". In: *ACS Nano* 4.7 (2010), pp. 4206–4210. ISSN: 19360851. DOI: 10.1021/nn100971s.

[131] C. Riedl et al. "Structural properties of the graphene-SiC(0001) interface as a key for the preparation of homogeneous large-terrace graphene surfaces". In: *Physical Review B - Condensed Matter and Materials Physics* 76.24 (2007), p. 245406. ISSN: 10980121. DOI: 10.1103/PhysRevB.76.245406.

[132] K. V. Emtsev et al. "Towards wafer-size graphene layers by atmospheric pressure graphitization of silicon carbide". In: *Nature Materials* 8.3 (2009), pp. 203–207. ISSN: 14764660. DOI: 10.1038/nmat2382.

[133] Y. M. Lin et al. *100-GHz transistors from wafer-scale epitaxial graphene*. 2010. DOI: 10.1126/science.1184289. arXiv: 1002.3845.

[134] A. J. Van Bommel, J. E. Crombeen, and A. Van Tooren. "LEED and Auger electron observations of the SiC(0001) surface". In: *Surface Science* 48.2 (1975), pp. 463–472. ISSN: 00396028. DOI: 10.1016/0039-6028(75)90419-7.

[135] U. Starke and C. Riedl. "Epitaxial graphene on SiC(0001) and : From surface reconstructions to carbon electronics". In: *Journal of Physics Condensed Matter* 21.13 (2009), p. 134016. ISSN: 09538984. DOI: 10.1088/0953-8984/21/13/134016.

[136] I. Forbeaux, J. Themlin, and J. Debever. "Heteroepitaxial graphite on Interface formation through conduction-band electronic structure". In: *Physical Review B - Condensed Matter and Materials Physics* 58.24 (1998), pp. 16396–16406. ISSN: 1550235X. DOI: 10.1103/PhysRevB.58.16396.

[137] C. Berger et al. "Ultrathin epitaxial graphite: 2D electron gas properties and a route toward graphene-based nanoelectronics". In: *Journal of Physical Chemistry B* 108.52 (2004), pp. 19912–19916. ISSN: 15206106. DOI: 10.1021/jp040650f. arXiv: 0410240 [cond-mat].

[138] D. Momeni Pakdehi et al. "Homogeneous Large-Area Quasi-Free-Standing Monolayer and Bilayer Graphene on SiC". In: *ACS Applied Nano Materials* 2.2 (2019), pp. 844–852. ISSN: 25740970. DOI: 10.1021/acsanm.8b02093. arXiv: 1811.04998.

[139] D. Momeni Pakdehi et al. "Minimum Resistance Anisotropy of Epitaxial Graphene on SiC". In: *ACS Applied Materials and Interfaces* 10.6 (2018), pp. 6039–6045. ISSN: 19448252. DOI: 10.1021/acsami.7b18641.

[140] W. A. De Heer et al. "Large area and structured epitaxial graphene produced by confinement controlled sublimation of silicon carbide". In: *Proceedings of the National Academy of Sciences of the United States of America* 108.41 (2011), pp. 16900–16905. ISSN: 00278424. DOI: `10.1073/pnas.1105113108`.

[141] T. Seyller et al. "Epitaxial graphene: a new material". In: *physica status solidi (b)* 245.7 (2008), pp. 1436–1446. ISSN: 03701972. DOI: `10.1002/pssb.200844143`.

[142] R. Yakimova et al. "Morphological and electronic properties of epitaxial graphene on SiC". In: *Physica B: Condensed Matter* 439 (2014), pp. 54–59. ISSN: 09214526. DOI: `10.1016/j.physb.2013.12.048`.

[143] G. G. Jernigan et al. "Comparison of epitaxial graphene on si-face and C-face 4H SiC formed by ultrahigh vacuum and RF furnace production". In: *Nano Letters* 9.7 (2009), pp. 2605–2609. ISSN: 15306984. DOI: `10.1021/nl900803z`.

[144] W. Norimatsu and M. Kusunoki. "Structural features of epitaxial graphene on SiC 0 0 0 1 surfaces". In: *Journal of Physics D: Applied Physics* 47.9 (2014), p. 094017. ISSN: 00223727. DOI: `10.1088/0022-3727/47/9/094017`.

[145] K. V. Emtsev et al. "Ambipolar doping in quasifree epitaxial graphene on SiC(0001) controlled by Ge intercalation". In: *Physical Review B - Condensed Matter and Materials Physics* 84.12 (2011), p. 125423. ISSN: 10980121. DOI: `10.1103/PhysRevB.84.125423`.

[146] U. Starke, S. Forti, K. V. Emtsev, and C. Coletti. *Engineering the electronic structure of epitaxial graphene by transfer doping and atomic intercalation.* 2012. DOI: `10.1557/mrs.2012.272`.

[147] C. Virojanadara et al. "Homogeneous large-area graphene layer growth on 6H-SiC(0001)". In: *Physical Review B - Condensed Matter and Materials Physics* 78.24 (2008), p. 245403. ISSN: 1550235X. DOI: `10.1103/PhysRevB.78.245403`.

[148] V. Darakchieva et al. "Large-area microfocal spectroscopic ellipsometry mapping of thickness and electronic properties of epitaxial graphene on Si- and C-face of 3C-SiC(111)". In: *Applied Physics Letters* 102.21 (2013), p. 213116. ISSN: 00036951. DOI: `10.1063/1.4808379`.

[149] C. Riedl et al. "Quasi-free-standing epitaxial graphene on SiC obtained by hydrogen intercalation". In: *Physical Review Letters* 103.24 (2009), pp. 1–4. ISSN: 00319007. DOI: `10.1103/PhysRevLett.103.246804`. arXiv: `arXiv:0911.1953v1`.

[150] C. Riedl, C. Coletti, and U. Starke. "Structural and electronic properties of epitaxial Graphene on SiC(0001): A review of growth, characterization, transfer doping and hydrogen intercalation". In: *Journal of Physics D: Applied Physics* 43.37 (2010), p. 374009. ISSN: 00223727. DOI: `10.1088/0022-3727/43/37/374009`.

[151] C. Virojanadara, A. A. Zakharov, R. Yakimova, and L. I. Johansson. "Buffer layer free large area bi-layer graphene on SiC(0 0 0 1)". In: *Surface Science* 604.2 (2010), p. L4. ISSN: 00396028. DOI: `10.1016/j.susc.2009.11.011`.

[152] C. Xia et al. "Detailed studies of Na intercalation on furnace-grown graphene on 6H-SiC(0001)". In: *Surface Science* 613 (2013), pp. 88–94. ISSN: 00396028. DOI: `10.1016/j.susc.2013.03.011`.

[153] M. H. Oliveira et al. "Formation of high-quality quasi-free-standing bilayer graphene on SiC(0 0 0 1) by oxygen intercalation upon annealing in air". In: *Carbon* 52 (2013), pp. 83–89. ISSN: 00086223. DOI: 10.1016/j.carbon.2012.09.008.

[154] C. Virojanadara, S. Watcharinyanon, A. A. Zakharov, and L. I. Johansson. "Epitaxial graphene on 6H-SiC and Li intercalation". In: *Physical Review B - Condensed Matter and Materials Physics* 82.20 (2010), p. 205402. ISSN: 10980121. DOI: 10.1103/PhysRevB.82.205402.

[155] C. Xia et al. "Si intercalation/deintercalation of graphene on 6H-SiC(0001)". In: *Physical Review B - Condensed Matter and Materials Physics* 85.4 (2012), p. 045418. ISSN: 10980121. DOI: 10.1103/PhysRevB.85.045418.

[156] I. Gierz et al. "Electronic decoupling of an epitaxial graphene monolayer by gold intercalation". In: *Physical Review B - Condensed Matter and Materials Physics* 81.23 (2010), p. 235408. ISSN: 10980121. DOI: 10.1103/PhysRevB.81.235408. arXiv: 1003.2355.

[157] A. L. Walter et al. "Highly p -doped epitaxial graphene obtained by fluorine intercalation". In: *Applied Physics Letters* 98.18 (2011), p. 184102. ISSN: 00036951. DOI: 10.1063/1.3586256.

[158] C Riedl et al. "Structural and electronic properties of epitaxial graphene on SiC (0001): a review of growth , characterization , transfer doping and hydrogen intercalation To cite this version : HAL Id : hal-00569700 Structural and electronic properties of epitaxial g". In: 0001 (2011).

[159] V. Jain and B. Kandasubramanian. *Functionalized graphene materials for hydrogen storage.* 2020. DOI: 10.1007/s10853-019-04150-y.

[160] S. Gadipelli and Z. X. Guo. "Graphene-based materials: Synthesis and gas sorption, storage and separation". In: *Progress in Materials Science* 69 (2015), pp. 1–60. ISSN: 0079-6425. DOI: 10.1016/J.PMATSCI.2014.10.004.

[161] A. C. Ferrari et al. "Science and technology roadmap for graphene, related two-dimensional crystals, and hybrid systems". In: *Nanoscale* 7.11 (2015), pp. 4598–4810. ISSN: 20403372. DOI: 10.1039/c4nr01600a.

[162] S. Goler et al. "Influence of Graphene Curvature on Hydrogen Adsorption: Toward Hydrogen Storage Devices". In: *The Journal of Physical Chemistry C* 117.22 (2013), pp. 11506–11513. ISSN: 1932-7447. DOI: 10.1021/jp4017536.

[163] Y. Dan et al. "Intrinsic response of graphene vapor sensors". In: *Nano Letters* 9.4 (2009), pp. 1472–1475. ISSN: 15306984. DOI: 10.1021/nl8033637.

[164] J. D. Fowler et al. "Practical chemical sensors from chemically derived graphene". In: *ACS Nano* 3.2 (2009), pp. 301–306. ISSN: 19360851. DOI: 10.1021/nn800593m.

[165] K. R. Ratinac, W. Yang, S. P. Ringer, and F. Braet. *Toward ubiquitous environmental gas sensors - Capitalizing on the promise of graphene.* 2010. DOI: 10.1021/es902659d.

[166] J. Peña-Bahamonde, H. N. Nguyen, S. K. Fanourakis, and D. F. Rodrigues. *Recent advances in graphene-based biosensor technology with applications in life sciences.* 2018. DOI: 10.1186/s12951-018-0400-z.

[167] T. Hussain, P. Panigrahi, and R. Ahuja. "Sensing propensity of a defected graphane sheet towards CO, H2O and NO2". In: *Nanotechnology* 25.32 (2014), p. 325501. ISSN: 13616528. DOI: 10.1088/0957-4484/25/32/325501.

[168] D. Slawig, M. Gruschwitz, and C. Tegenkamp. "Strong localization in weakly disordered epitaxial graphene". In: *Surface Science* 707 (2021), p. 121801. ISSN: 00396028. DOI: 10.1016/j.susc.2021.121801.

[169] G. R. Schleder et al. "Tuning Hydrogen Adsorption and Electronic Properties from Graphene to Fluorographone". In: *Physical Review Materials* 4.7 (2020), p. 074005. ISSN: 2475-9953. DOI: 10.1103/PhysRevMaterials.4.074005. arXiv: 2005.03854.

[170] D. Haberer et al. "Tunable Band Gap in Hydrogenated Quasi-Free-Standing Graphene". In: *Nano Letters* 10.9 (2010), pp. 3360–3366. ISSN: 15306984. DOI: 10.1021/nl101066m.

[171] H. González-Herrero et al. "Atomic-scale control of graphene magnetism by using hydrogen atoms". In: *Science* 352.6284 (2016), pp. 437–441. ISSN: 10959203. DOI: 10.1126/science.aad8038.

[172] R. Balog et al. "Bandgap opening in graphene induced by patterned hydrogen adsorption". In: *Nature Materials* 9.4 (2010), pp. 315–319. ISSN: 14764660. DOI: 10.1038/nmat2710.

[173] D. W. Boukhvalov and M. I. Katsnelson. "Chemical functionalization of graphene". In: *Journal of Physics Condensed Matter* 21.34 (2009), p. 344205. ISSN: 09538984. DOI: 10.1088/0953-8984/21/34/344205.

[174] D. W. Boukhvalov, M. I. Katsnelson, and A. I. Lichtenstein. "Hydrogen on graphene: Electronic structure, total energy, structural distortions and magnetism from first-principles calculations". In: *Physical Review B - Condensed Matter and Materials Physics* 77.3 (2008), p. 035427. ISSN: 10980121. DOI: 10.1103/PhysRevB.77.035427. arXiv: 0710.1971.

[175] S. Lebègue, M. Klintenberg, O. Eriksson, and M. I. Katsnelson. "Accurate electronic band gap of pure and functionalized graphane from GW calculations". In: *Physical Review B* 79.24 (2009), p. 245117. ISSN: 1098-0121. DOI: 10.1103/PhysRevB.79.245117.

[176] J. O. Sofo, A. S. Chaudhari, and G. D. Barber. "Graphane: A two-dimensional hydrocarbon". In: *Physical Review B - Condensed Matter and Materials Physics* 75.15 (2007), p. 153401. ISSN: 10980121. DOI: 10.1103/PhysRevB.75.153401. arXiv: 0606704 [cond-mat].

[177] A. Rossi et al. "Nano-scale corrugations in graphene: A density functional theory study of structure, electronic properties and hydrogenation". In: *Journal of Physical Chemistry C* 119.14 (2015), pp. 7900–7910. ISSN: 19327455. DOI: 10.1021/jp511409b.

[178] L. Gao et al. "Current-Driven Hydrogen Desorption from Graphene: Experiment and Theory". In: *Journal of Physical Chemistry Letters* 7.3 (2016), pp. 486–494. ISSN: 19487185. DOI: 10.1021/acs.jpclett.5b02471.

[179] B. R. Matis et al. "Surface Doping and Band Gap Tunability in Hydrogenated Graphene". In: *ACS Nano* 6.1 (2012), pp. 17–22. ISSN: 1936-0851. DOI: 10.1021/nn2034555.

[180] G. A. Beitel. "Sticking Probability of Atomic Hydrogen on Graphite". In: *Journal of Vacuum Science and Technology* 6.1 (1969), pp. 224–228. ISSN: 0022-5355. DOI: 10.1116/1.1492666.

[181] T. Zecho et al. "Adsorption of hydrogen and deuterium atoms on the (0001) graphite surface". In: *Journal of Chemical Physics* 117.18 (2002), pp. 8486–8492. ISSN: 00219606. DOI: 10.1063/1.1511729.

[182] K. Bennaceur et al. "Measurement of topological Berry phase in highly disordered graphene". In: *Physical Review B - Condensed Matter and Materials Physics* 92.12 (2015), pp. 1–7. ISSN: 1550235X. DOI: 10.1103/PhysRevB.92.125410. arXiv: 1510.03506.

[183] Y. Murata et al. "Correlation between morphology and transport properties of quasi-free-standing monolayer graphene". In: *Applied Physics Letters* 105.22 (2014). ISSN: 00036951. DOI: 10.1063/1.4902988.

[184] S. Casolo, O. M. Løvvik, R. Martinazzo, and G. F. Tantardini. "Understanding adsorption of hydrogen atoms on graphene". In: *The Journal of Chemical Physics* 130.5 (2009), p. 054704. ISSN: 00219606. DOI: 10.1063/1.3072333. arXiv: 0808.1312.

[185] M. Z. Flores, P. A. Autreto, S. B. Legoas, and D. S. Galvao. "Graphene to graphane: A theoretical study". In: *Nanotechnology* 20.46 (2009), p. 465704. ISSN: 09574484. DOI: 10.1088/0957-4484/20/46/465704. arXiv: 0910.4304.

[186] K. G. Tschersich. "Intensity of a source of atomic hydrogen based on a hot capillary". In: *Journal of Applied Physics* 87.5 (2000), pp. 2565–2573. ISSN: 00218979. DOI: 10.1063/1.372220.

[187] K. G. Tschersich, J. P. Fleischhauer, and H. Schuler. "Design and characterization of a thermal hydrogen atom source". In: *Journal of Applied Physics* 104.3 (2008), p. 034908. ISSN: 00218979. DOI: 10.1063/1.2963956.

[188] K. G. Tschersich and V. Von Bonin. "Formation of an atomic hydrogen beam by a hot capillary". In: *Journal of Applied Physics* 84.8 (1998), pp. 4065–4070. ISSN: 00218979. DOI: 10.1063/1.368619.

[189] A. Bostwick et al. "Quasiparticle transformation during a metal-insulator transition in graphene". In: *Physical Review Letters* 103.5 (2009), pp. 1–4. ISSN: 00319007. DOI: 10.1103/PhysRevLett.103.056404. arXiv: 0904.2249.

[190] M. Henzler. "LEED studies of surface imperfections". In: *Applications of Surface Science* 11-12.C (1982), pp. 450–469. ISSN: 03785963. DOI: 10.1016/0378-5963(82)90092-7.

[191] D. C. Elias et al. "Control of graphene's properties by reversible hydrogenation: Evidence for graphane". In: *Science* 323.5914 (2009), pp. 610–613. ISSN: 00368075. DOI: 10.1126/science.1167130.

[192] J. Aprojanz et al. "High-Mobility Epitaxial Graphene on Ge/Si(100) Substrates". In: *ACS Applied Materials and Interfaces* 12.38 (2020), pp. 43065–43072. ISSN: 19448252. DOI: 10.1021/acsami.0c10725.

[193] Y. Murata, A. Calzolari, and S. Heun. "Tuning hydrogen adsorption on graphene by gate voltage". In: *Journal of Physical Chemistry C* 122.21 (2018), pp. 11591–11597. ISSN: 19327455. DOI: 10.1021/acs.jpcc.8b03627.

[194] J. Baringhaus et al. "Local transport measurements on epitaxial graphene". In: *Applied Physics Letters* 103.11 (2013), p. 111604. ISSN: 00036951. DOI: 10.1063/1.4821364.

[195] N. F. Mott, E. A. Davis, and K. Weiser. " Electronic Processes in Non-Crystalline Materials ". In: *Physics Today* 25.12 (1972), pp. 55–55. ISSN: 0031-9228. DOI: 10.1063/1.3071145.

[196] D. C. Tsui and S. J. Allen. "Mott-anderson localization in the two-dimensional band tail of si inversion layers". In: *Physical Review Letters* 32.21 (1974), pp. 1200–1203. ISSN: 00319007. DOI: 10.1103/PhysRevLett.32.1200.

[197] J. Ristein, S. Mammadov, and T. Seyller. "Origin of doping in quasi-free-standing graphene on silicon carbide". In: *Physical Review Letters* 108.24 (2012), p. 246104. ISSN: 00319007. DOI: 10.1103/PhysRevLett.108.246104. arXiv: 1109.6907.

[198] E. Bekyarova et al. "Advances in the chemical modification of epitaxial graphene". In: *Journal of Physics D: Applied Physics* 45.15 (2012), p. 154009. ISSN: 00223727. DOI: 10.1088/0022-3727/45/15/154009.

[199] J. M. MacLeod and F. Rosei. "Molecular self-assembly on graphene". In: *Small* 10.6 (2014), pp. 1038–1049. ISSN: 16136829. DOI: 10.1002/smll.201301982.

[200] A. Kumar, K. Banerjee, and P. Liljeroth. *Molecular assembly on two-dimensional materials.* 2017. DOI: 10.1088/1361-6528/aa564f. arXiv: 1611.02462.

[201] C. Brülke et al. "Quantitative analysis of the electronic decoupling of an organic semiconductor molecule at a metal interface by a monolayer of hexagonal boron nitride". In: *Physical Review B* 99.12 (2019), p. 121404. ISSN: 24699969. DOI: 10.1103/PhysRevB.99.121404.

[202] K. S. Mali et al. *Nanostructuring graphene for controlled and reproducible functionalization.* 2015. DOI: 10.1039/c4nr06470d.

[203] F. Schwarz et al. "Field-induced conductance switching by charge-state alternation in organometallic single-molecule junctions". In: *Nature Nanotechnology* 11.2 (2016), pp. 170–176. ISSN: 17483395. DOI: 10.1038/nnano.2015.255.

[204] Z. Zhang, H. Huang, X. Yang, and L. Zang. *Tailoring electronic properties of graphene by π-π Stacking with aromatic molecules.* 2011. DOI: 10.1021/jz201273r.

[205] J. Watson, K. Ihokura, J. Abadran, and M. C. Carrota. "Gas-sensing materials". In: *MRS Bulletin* 24.6 (1999), pp. 14–15. ISSN: 08837694. DOI: 10.1557/s0883769400052453.

[206] A. Ilnicka and J. P. Lukaszewicz. *Graphene-based hydrogen gas sensors: A review.* 2020. DOI: 10.3390/PR8050633.

[207] D. Shahdeo, A. Roberts, N. Abbineni, and S. Gandhi. "Graphene based sensors". In: *Comprehensive Analytical Chemistry.* Vol. 91. Elsevier B.V., 2020, pp. 175–199. ISBN: 9780323853712. DOI: 10.1016/bs.coac.2020.08.007.

[208] N. Taguchi. *Gas detecting element and method of making it.* 1972.

[209] K. Ihokura and J. Watson. *The stannic oxide gas sensor: Principles and applications.* CRC Press, 1994, pp. 1–187. ISBN: 9781351409018. DOI: `10.1201/9780203735893`.

[210] T. Kuila et al. *Chemical functionalization of graphene and its applications.* 2012. DOI: `10.1016/j.pmatsci.2012.03.002`.

[211] D. W. Boukhvalov. "Modeling of epitaxial grapheme functionalization". In: *Nanotechnology* 22.5 (2011), p. 055708. ISSN: 09574484. DOI: `10.1088/0957-4484/22/5/055708`.

[212] J. M. Gottfried. *Surface chemistry of porphyrins and phthalocyanines.* 2015. DOI: `10.1016/j.surfrep.2015.04.001`.

[213] K. Walzer and M. Hietschold. "STM and STS investigation of ultrathin tin phthalocyanine layers adsorbed on HOPG(0 0 0 1) and Au(1 1 1)". In: *Surface Science* 471.1-3 (2001), pp. 1–10. ISSN: 00396028. DOI: `10.1016/S0039-6028(00)00909-2`.

[214] J. D. Baran and J. A. Larsson. "Inversion of the shuttlecock shaped metal phthalocyanines MPc (M = Ge, Sn, Pb)-a density functional study". In: (2009). DOI: `10.1039/b924421b`.

[215] T. T. Nhung Nguyen et al. "Noninvasive coupling of PbPc monolayers to epitaxial graphene on SiC(0001)". In: *Surface Science* 686.April (2019), pp. 45–51. ISSN: 00396028. DOI: `10.1016/j.susc.2019.04.003`.

[216] J. E. Andersen, M. H. Jensen, P. Møller, and J. Ulstrup. "Perspectives for in situ scanning tunnel microscopic imaging of metalloproteins at HOPG surfaces". In: *Electrochimica Acta* 41.13 (1996), pp. 2005–2010. ISSN: 00134686. DOI: `10.1016/0013-4686(96)00005-9`.

[217] T. T. N. Nguyen et al. "Impact of screening and relaxation on weakly coupled two-dimensional heterostructures". In: *Physical Review B* 103.20 (2021), p. L201408. ISSN: 2469-9950. DOI: `10.1103/physrevb.103.l201408`.

[218] J. Ren et al. "Properties of copper (fluoro-)phthalocyanine layers deposited on epitaxial graphene". In: *Journal of Chemical Physics* 134.19 (2011), p. 194706. ISSN: 00219606. DOI: `10.1063/1.3590277`.

[219] A. J. Marsden et al. "Growth of Large Crystalline Grains of Vanadyl-Phthalocyanine without Epitaxy on Graphene". In: *Advanced Functional Materials* 26.8 (2016), pp. 1188–1196. ISSN: 1616301X. DOI: `10.1002/adfm.201503594`.

[220] R. F. Egerton, P. Li, and M. Malac. "Radiation damage in the TEM and SEM". In: *Micron.* Vol. 35. 6. Pergamon, 2004, pp. 399–409. DOI: `10.1016/j.micron.2004.02.003`.

[221] K. Seshadri et al. "Electron-beam-induced damage in self-assembled monolayers". In: *Journal of Physical Chemistry* 100.39 (1996), pp. 15900–15909. ISSN: 00223654. DOI: `10.1021/jp960705g`.

[222] M. Eichberger et al. "Dimerization boosts one-dimensional mobility of conformationally adapted porphyrins on a hexagonal surface atomic lattice". In: *Nano Letters* 8.12 (2008), pp. 4608–4613. ISSN: 15306984. DOI: `10.1021/nl802995u`.

[223] G. Antczak et al. "Complex Surface Diffusion Mechanisms of Cobalt Phthalocyanine Molecules on Ag(100)". In: *Journal of the American Chemical Society* 137.47 (2015), pp. 14920–14929. ISSN: 15205126. DOI: 10.1021/jacs.5b08001.

[224] L. Tsetseris. "Hydrogen- and oxygen-related effects in phthalocyanine crystals: Formation of carrier traps and a change in the magnetic state". In: *Physical Chemistry Chemical Physics* 16.7 (2014), pp. 3317–3322. ISSN: 14639076. DOI: 10.1039/c3cp54755h.

[225] M. Inagaki, Y. Yang, and F. Kang. "Carbon Nanofibers Prepared via Electrospinning". In: *Advanced Materials* 24.19 (2012), pp. 2547–2566. ISSN: 09359648. DOI: 10.1002/adma.201104940.

[226] J. C. Ruiz-Cornejo, D. Sebastián, and M. J. Lázaro. *Synthesis and applications of carbon nanofibers: A review*. 2020. DOI: 10.1515/revce-2018-0021.

[227] K. L. Klein et al. "Surface characterization and functionalization of carbon nanofibers". In: *Journal of Applied Physics* 103.6 (2008), p. 061301. ISSN: 00218979. DOI: 10.1063/1.2840049.

[228] F. Ko et al. "Electrospinning of Continuous Carbon Nanotube-Filled Nanofiber Yarns". In: *Advanced Materials* 15.14 (2003), pp. 1161–1165. ISSN: 09359648. DOI: 10.1002/adma.200304955.

[229] A. Ramos, I. Cameán, and A. B. García. *Graphitization thermal treatment of carbon nanofibers*. 2013. DOI: 10.1016/j.carbon.2013.03.031.

[230] J. Cai and M. Naraghi. "The formation of highly ordered graphitic interphase around embedded CNTs controls the mechanics of ultra-strong carbonized nanofibers". In: *Acta Materialia* 162 (2019), pp. 46–54. ISSN: 13596454. DOI: 10.1016/j.actamat.2018.09.047.

[231] H. Matsumoto et al. "Electrospun composite nanofiber yarns containing oriented graphene nanoribbons". In: *ACS Applied Materials and Interfaces* 5.13 (2013), pp. 6225–6231. ISSN: 19448244. DOI: 10.1021/am401161b.

[232] A. B. Ali et al. "Polyacrylonitrile (PAN) based electrospun carbon nanofibers (EC-NFs): Probing the synergistic effects of creep assisted stabilization and CNTs addition on graphitization and low dimensional electrical transport". In: *Carbon* 172 (2021), pp. 283–295. ISSN: 00086223. DOI: 10.1016/j.carbon.2020.10.033.

[233] A. C. Ferrari and D. M. Basko. *Raman spectroscopy as a versatile tool for studying the properties of graphene*. 2013. DOI: 10.1038/nnano.2013.46. arXiv: 1306.5856.

[234] S. Prilutsky, E. Zussman, and Y. Cohen. "The effect of embedded carbon nanotubes on the morphological evolution during the carbonization of poly(acrylonitrile) nanofibers". In: *Nanotechnology* 19.16 (2008), p. 165603. ISSN: 09574484. DOI: 10.1088/0957-4484/19/16/165603.

[235] A. Bin Ali et al. "Electrospun Polyacrylonitrile Based Carbon Nanofibers: The Role of Creep Stress towards Cyclization and Graphitization". In: *Journal of Material Science & Engineering* 07.05 (2018). DOI: 10.4172/2169-0022.1000493.

[236] J Aprojanz et al. "Highly anisotropic electric conductivity in PAN-based carbon nanofibers". In: *Journal of Physics: Condensed Matter* 29.49 (2017), p. 494002. ISSN: 0953-8984. DOI: 10.1088/1361-648X/aa9494.

[237] S. Chawla, J. Cai, and M. Naraghi. "Mechanical tests on individual carbon nanofibers reveals the strong effect of graphitic alignment achieved via precursor hot-drawing". In: *Carbon* 117 (2017), pp. 208–219. ISSN: 00086223. DOI: 10.1016/j.carbon.2017.02.095.

[238] T. Maitra et al. "Improved graphitization and electrical conductivity of suspended carbon nanofibers derived from carbon nanotube/polyacrylonitrile composites by directed electrospinning". In: *Carbon* 50.5 (2012), pp. 1753–1761. ISSN: 00086223. DOI: 10.1016/j.carbon.2011.12.021.

[239] J. Cai and M. Naraghi. "Effect of Templating Graphitization on Electrical Conductivity of Electrospun CNTs Reinforced Carbon Nanofiber". In: (2017). DOI: 10.2514/6.2017-0796.

[240] D. A. Dikin et al. "Preparation and characterization of graphene oxide paper". In: *Nature* 448.7152 (2007), pp. 457–460. ISSN: 00280836. DOI: 10.1038/nature06016.

[241] D. Li et al. "Processable aqueous dispersions of graphene nanosheets". In: *Nature Nanotechnology* 3.2 (2008), pp. 101–105. ISSN: 17483387. DOI: 10.1038/nnano.2007.451.

[242] S. Gilje et al. "A chemical route to graphene for device applications". In: *Nano Letters* 7.11 (2007), pp. 3394–3398. ISSN: 15306984. DOI: 10.1021/nl0717715.

[243] C. Gómez-Navarro et al. "Electronic transport properties of individual chemically reduced graphene oxide sheets". In: *Nano Letters* 7.11 (2007), pp. 3499–3503. ISSN: 15306984. DOI: 10.1021/nl072090c.

[244] D. Slawig et al. "Anisotropic transport properties of graphene-based conductor materials". In: *Journal of Materials Science* (2021), pp. 1–8. ISSN: 0022-2461. DOI: 10.1007/s10853-021-06231-3.

[245] I. Khrapach et al. "Novel Highly Conductive and Transparent Graphene-Based Conductors". In: *Advanced Materials* 24.21 (2012), pp. 2844–2849. ISSN: 09359648. DOI: 10.1002/adma.201200489.

[246] S. Stankovich et al. "Graphene-based composite materials". In: *Nature* 442.7100 (2006), pp. 282–286. ISSN: 0028-0836. DOI: 10.1038/nature04969.

[247] Y. Ma and L. Zhi. "Graphene-Based Transparent Conductive Films: Material Systems, Preparation and Applications". In: *Small Methods* 3.1 (2019), p. 1800199. ISSN: 23669608. DOI: 10.1002/smtd.201800199.

[248] D. Momeni Pakdehi et al. "Silicon Carbide Stacking-Order-Induced Doping Variation in Epitaxial Graphene". In: *Advanced Functional Materials* 30.45 (2020), p. 2004695. ISSN: 1616-301X. DOI: 10.1002/adfm.202004695.

[249] A. R. J. P. Ubbelohde. "Electrical anisotropy of synthetic metals based on graphite". In: *Proceedings of the Royal Society of London. A. Mathematical and Physical Sciences* 327.1570 (1972), pp. 289–303. ISSN: 2053-9169. DOI: 10.1098/rspa.1972.0046.

[250] S. Banerjee et al. "Conductivity landscape of highly oriented pyrolytic graphite surfaces containing ribbons and edges". In: *Physical Review B* 72.7 (2005), p. 075418. ISSN: 1098-0121. DOI: 10.1103/PhysRevB.72.075418.

[251] M. Cermak, N. Perez, M. Collins, and M. Bahrami. "Material properties and structure of natural graphite sheet". In: *Scientific Reports* 10.1 (2020), pp. 1–12. ISSN: 20452322. DOI: 10.1038/s41598-020-75393-y.

[252] J. M. Abendroth et al. "Analyzing Spin Selectivity in DNA-Mediated Charge Transfer via Fluorescence Microscopy". In: *ACS Nano* 11.7 (2017), pp. 7516–7526. ISSN: 1936086X. DOI: 10.1021/acsnano.7b04165.

[253] T. J. Zwang, S. Hürlimann, M. G. Hill, and J. K. Barton. "Helix-Dependent Spin Filtering through the DNA Duplex". In: *Journal of the American Chemical Society* (2016), jacs.6b10538. ISSN: 0002-7863. DOI: 10.1021/jacs.6b10538.

[254] S. Mishra et al. "Spin Filtering Along Chiral Polymers". In: *Angewandte Chemie International Edition* 59.34 (2020), pp. 14671–14676. ISSN: 1433-7851. DOI: 10.1002/anie.202006570.

[255] A. A. Eremko and V. M. Loktev. "Spin sensitive electron transmission through helical potentials". In: *Physical Review B - Condensed Matter and Materials Physics* 88.16 (2013), pp. 1–5. ISSN: 10980121. DOI: 10.1103/PhysRevB.88.165409. arXiv: arXiv:1306.3758v1.

[256] S. Yeganeh, M. A. Ratner, E. Medina, and V. Mujica. "Chiral electron transport: Scattering through helical potentials". In: *Journal of Chemical Physics* 131.1 (2009). ISSN: 00219606. DOI: 10.1063/1.3167404.

[257] R. Gutierrez, E. Díaz, R. Naaman, and G. Cuniberti. "Spin-selective transport through helical molecular systems". In: *Physical Review B - Condensed Matter and Materials Physics* 85.8 (2012), pp. 2–5. ISSN: 10980121. DOI: 10.1103/PhysRevB.85.081404. arXiv: arXiv:1110.0354v2.

[258] R. Gutierrez et al. "Modeling spin transport in helical fields: Derivation of an effective low-dimensional hamiltonian". In: *Journal of Physical Chemistry C* 117.43 (2013), pp. 22276–22284. ISSN: 19327447. DOI: 10.1021/jp401705x.

[259] A. M. Guo and Q. F. Sun. "Enhanced spin-polarized transport through DNA double helix by gate voltage". In: *Physical Review B - Condensed Matter and Materials Physics* 86.3 (2012), pp. 1–5. ISSN: 10980121. DOI: 10.1103/PhysRevB.86.035424. arXiv: arXiv:1409.1050v1.

[260] A.-M. Guo, Q.-F. Q.-F. Sun, and J. R. Winkler. "Spin-dependent electron transport in protein-like single-helical molecules". In: *Proceedings of the National Academy of Sciences* 111.32 (2014), pp. 11658–11662. ISSN: 0027-8424. DOI: 10.1073/pnas.1407716111.

[261] J. Gersten, K. Kaasbjerg, and A. Nitzan. "Induced spin filtering in electron transmission through chiral molecular layers adsorbed on metals with strong spin-orbit coupling". In: *Journal of Chemical Physics* 139.11 (2013), p. 114111. ISSN: 00219606. DOI: 10.1063/1.4820907.

[262] R. A. Caetano. "Spin-Current and Spin-Splitting in Helicoidal Molecules Due to Spin-Orbit Coupling". In: *Nature Publishing Group* March (2016), pp. 1–11. ISSN: 2045-2322. DOI: 10.1038/srep23452.

[263] V. V. Maslyuk et al. "Enhanced Magnetoresistance in Chiral Molecular Junctions". In: *Journal of Physical Chemistry Letters* 9.18 (2018), pp. 5453–5459. ISSN: 19487185. DOI: 10.1021/acs.jpclett.8b02360.

[264] R. Naaman and Z. Vager. "Cooperative electronic and magnetic properties of self-assembled monolayers". In: *MRS Bulletin* 35.6 (2010), pp. 429–434. ISSN: 08837694. DOI: 10.1557/mrs2010.580.

[265] K. Ray, S. P. Ananthavel, D. H. Waldeck, and R. Naaman. "Asymmetric scattering of polarized electrons by organized organic films of chiral molecules". In: *Science* 283.5403 (1999), pp. 814–816. ISSN: 00368075. DOI: 10.1126/science.283.5403.814.

[266] D. Mishra et al. "Spin-dependent electron transmission through bacteriorhodopsin embedded in purple membrane". In: *Proceedings of the National Academy of Sciences of the United States of America* 110.37 (2013), pp. 14872–14876. ISSN: 1091-6490. DOI: 10.1073/pnas.1311493110.

[267] S. Ravi, P. Sowmiya, and A. Karthikeyan. "Magnetoresistance and spin-filtering efficiency of dna-sandwiched ferromagnetic nanostructures". In: *SPIN* 3.1 (2013). ISSN: 20103255. DOI: 10.1142/S2010324713500033.

[268] J. J. Wei et al. "Molecular chirality and charge transfer through self-assembled scaffold monolayers". In: *Journal of Physical Chemistry B* 110.3 (2006), pp. 1301–1308. ISSN: 15206106. DOI: 10.1021/jp055145c.

[269] C. Nogues, S. R. Cohen, S. S. Daube, and R. Naaman. "Electrical properties of short DNA oligomers characterized by conducting atomic force microscopy". In: *Physical Chemistry Chemical Physics* 6.18 (2004), pp. 4459–4466. ISSN: 14639076. DOI: 10.1039/b410862k.

[270] A. C. Aragonés et al. "Measuring the Spin-Polarization Power of a Single Chiral Molecule". In: *Small* 1602519 (2016), pp. 1–6. ISSN: 16136829. DOI: 10.1002/smll.201602519.

[271] K. Senthil Kumar et al. "A device for measuring spin selectivity in electron transfer". In: *Phys. Chem. Chem. Phys. Phys. Chem. Chem. Phys* 15.42 (2013), pp. 18357–18362. ISSN: 14639076. DOI: 10.1039/c3cp53089b.

[272] A. Hirohata et al. "A new approach towards spintronics–spintronics with no magnets". In: *J. Phys.: Condens. Matter* 29 (2017).

[273] R. A. Rosenberg, D. Mishra, and R. Naaman. "Chiral Selective Chemistry Induced by Natural Selection of Spin-Polarized Electrons". In: *Angewandte Chemie - International Edition* 54.25 (2015), pp. 7295–7298. ISSN: 15213773. DOI: 10.1002/anie.201501678.

[274] I. Meirzada et al. "Long-Time-Scale Magnetization Ordering Induced by an Adsorbed Chiral Monolayer on Ferromagnets". In: *ACS Nano* 15 (2021), p. 26. ISSN: 1936086X. DOI: 10.1021/acsnano.1c00455.

[275] A. Dianat et al. "Role of Exchange Interactions in the Magnetic Response and Intermolecular Recognition of Chiral Molecules". In: *Nano Letters* 20.10 (2020), pp. 7077–7086. ISSN: 15306992. DOI: 10.1021/acs.nanolett.0c02216.

[276] T. N. H. Nguyen et al. "Helical Ordering of α- l- Polyalanine Molecular Layers by Interdigitation". In: *The Journal of Physical Chemistry C* 123.1 (2019), pp. 612–617. ISSN: 1932-7447. DOI: 10.1021/acs.jpcc.8b10620.

[277] N. T. Ha et al. "Charge-Ordered α-Helical Polypeptide Monolayers on Au(111)". In: *Journal of Physical Chemistry C* 124.10 (2020), pp. 5734–5739. ISSN: 19327455. DOI: 10.1021/acs.jpcc.0c00246.

[278] T. N. Nguyen et al. "Helical Ordering of α-L-Polyalanine Molecular Layers by Interdigitation". In: *Journal of Physical Chemistry C* 123.1 (2019), pp. 612–617. ISSN: 19327455. DOI: 10.1021/acs.jpcc.8b10620.

[279] R. Di Felice, A. Selloni, and E. Molinari. "DFT study of cysteine adsorption on Au(111)". In: *Journal of Physical Chemistry B* 107.5 (2003), pp. 1151–1156. ISSN: 10895647. DOI: 10.1021/jp0272421.

[280] Y. Miura, S. Kimura, Y. Imanishi, and J. Umemura. "Formation of oriented helical peptide layers on a gold surface due to the self-assembling properties of peptides". In: *Langmuir* 14.24 (1998), pp. 6935–6940. ISSN: 07437463. DOI: 10.1021/la981296d.

[281] B. J. Van Wees et al. "Quantized conductance of point contacts in a two-dimensional electron gas". In: *Physical Review Letters* 60.9 (1988), pp. 848–850. ISSN: 00319007. DOI: 10.1103/PhysRevLett.60.848.

[282] Z. Gai, Y. He, H. Yu, and W. Yang. "Observation of conductance quantization of ballistic metallic point contacts at room temperature". In: *Physical Review B - Condensed Matter and Materials Physics* 53.3 (1996), pp. 1042–1045. ISSN: 1550235X. DOI: 10.1103/PhysRevB.53.1042.

[283] H. Yasuda and A. Sakai. "Conductance of atomic-scale gold contacts under high-bias voltages". In: *Physical Review B - Condensed Matter and Materials Physics* 56.3 (1997), pp. 1069–1072. ISSN: 1550235X. DOI: 10.1103/PhysRevB.56.1069.

[284] J. Costa-Krämer. "Conductance quantization at room temperature in magnetic and nonmagnetic metallic nanowires". In: *Physical Review B - Condensed Matter and Materials Physics* 55.8 (1997), R4875–R4878. ISSN: 1550235X. DOI: 10.1103/PhysRevB.55.R4875.

[285] K. Itakura et al. "Bias dependence of the conductance of au nanocontacts". In: *Physical Review B - Condensed Matter and Materials Physics* 60.15 (1999), pp. 11163–11170. ISSN: 1550235X. DOI: 10.1103/PhysRevB.60.11163.

[286] N. Amdursky. "Electron Transfer across Helical Peptides". In: *ChemPlusChem* 80.7 (2015), pp. 1075–1095. ISSN: 21926506. DOI: 10.1002/cplu.201500121.

[287] K. Kanthasamy et al. "Charge Transport through Ferrocene 1,1'-Diamine Single-Molecule Junctions". In: *Small* 12.35 (2016), pp. 4849–4856. ISSN: 16136810. DOI: 10.1002/smll.201601051.

[288] R. H. M. Smit et al. "Measurement of the conductance of a hydrogen molecule". In: *Nature* 419.6910 (2002), pp. 906–909. ISSN: 00280836. DOI: 10.1038/nature01103.

[289] V. B. Engelkes, J. M. Beebe, and C. D. Frisbie. "Length-dependent transport in molecular junctions based on SAMs of alkanethiols and alkanedithiols: Effect of metal work function and applied bias on tunneling efficiency and contact resistance". In: *Journal of the American Chemical Society* 126.43 (2004), pp. 14287–14296. ISSN: 00027863. DOI: `10.1021/ja046274u`.

[290] L. A. Zotti and J. C. Cuevas. "Electron Transport Through Homopeptides: Are They Really Good Conductors?" In: *ACS Omega* 3.4 (2018), pp. 3778–3785. ISSN: 24701343. DOI: `10.1021/acsomega.7b01917`.

[291] M. P. Ruiz et al. *Bioengineering a Single-Protein Junction.* 2017. DOI: `10.1021/jacs.7b06130`.

[292] Zotti et al. "Can One Define the Conductance of Amino Acids?" In: *Biomolecules* 9.10 (2019), p. 580. ISSN: 2218-273X. DOI: `10.3390/biom9100580`.

[293] K. Michaeli, D. N. Beratan, D. H. Waldeck, and R. Naaman. "Voltage-induced long-range coherent electron transfer through organic molecules". In: *Proceedings of the National Academy of Sciences of the United States of America* 116.13 (2019), pp. 5931–5936. ISSN: 10916490. DOI: `10.1073/pnas.1816956116`.

[294] D. J. Lockhart and P. S. Kim. "Internal stark effect measurement of the electric field at the amino terminus of an α helix". In: *Science* 257.5072 (1992), pp. 947–951. ISSN: 00368075. DOI: `10.1126/science.1502559`.

[295] D. W. Pierce and S. G. Boxer. "Stark effect spectroscopy of tryptophan". In: *Biophysical Journal* 68.4 (1995), pp. 1583–1591. ISSN: 00063495. DOI: `10.1016/S0006-3495(95)80331-0`.

Appendix B

Publication list

Printed

[1]   D. Slawig et al. "Electronic transport through single polyalanine molecules". In: *Physical Review B* 102.11 (2020), p. 115425. ISSN: 2469-9950. DOI: 10.1103/physrevb.102.115425.

[2]   N. T. N. Ha et al. "Charge-Ordered α-Helical Polypeptide Monolayers on Au(111)". In: *The Journal of Physical Chemistry C* 124.10 (2020), pp. 5734–5739. ISSN: 1932-7447. DOI: 10.1021/acs.jpcc.0c00246.

[3]   D. Slawig, M. Gruschwitz, and C. Tegenkamp. "Strong localization in weakly disordered epitaxial graphene". In: *Surface Science* 707 (2021), p. 121801. ISSN: 00396028. DOI: 10.1016/j.susc.2021.121801.

[4]   A. B. Ali et al. "Polyacrylonitrile (PAN) based electrospun carbon nanofibers (EC-NFs): Probing the synergistic effects of creep assisted stabilization and CNTs addition on graphitization and low dimensional electrical transport". In: *Carbon* 172 (2021), pp. 283–295. ISSN: 00086223. DOI: 10.1016/j.carbon.2020.10.033.

[5]   D. Slawig et al. "Anisotropic transport properties of graphene-based conductor materials". In: *Journal of Materials Science* (2021), pp. 1–8. ISSN: 0022-2461. DOI: 10.1007/s10853-021-06231-3.

Appendix C

Curriculum Vitae

PERSONAL INFORMATION:

NAME	Diana Slawig
DATE OF BIRTH	28.02.1991 in Leipzig

EDUCATION:

Since Sep. 2016	Doctoral Studies, Gottfried Wilhelm Leibniz Universität Hannover
2014 – 2016	Master of Science, Nanotechnology, Gottfried Wilhelm Leibniz Universität Hannover Thesis: *Impact of Substrate orientation on the carbon mediated epitaxy of Germanium on Silicon*
2010 – 2014	Bachelor of Science, Nanotechnology, Gottfried Wilhelm Leibniz Universität Hannover Thesis: *Electric transport measurements with atomic break junctions*
2001 – 2009	Abitur, F.A.-Brockhaus Gymnasium Leipzig

Declaration of originality

I hereby declare that this work reported here in the form of a doctoral thesis was entirely performed by me. Information reported from the published and unpublished work of other research items have been cited properly in the text and their references are given in the list of references. This work in any form has not been submitted for any other degree at any other university.

Hannover, September 30, 2021

Diana Slawig

Danksagung

An dieser Stelle möchte ich mich bei alle denjenigen bedankendie zum Gelingen dieser Arbeit beigetragen haben.

An erster Stelle danke ich Prof. Dr. Christoph Tegenkamp für die tolle Betreuung meiner Promotion auch unter widrigen Umständen. Die gute Kommunikation und die vielen Diskussionen über meine Ergebnisse haben diese Arbeit erst möglich gemacht.

Weiterhin möchte ich mich bei Prof. Dr. Herbert Pfnür für das ungebrochene Interesse am Fortgang meiner Arbeit bedanken, sowie für die immer offene Tür und die stetige Diskussionsbereitschaft. Ihm und Prof. Dr. Franz Renz danke ich auch für die Übernahme des Koreferats dieser Arbeit.

Ein sehr großer Dank gilt allen meinen Arbeitskollegen, so wohl in Hannover als auch in Chemnitz, für tolle Zusammenarbeit, die stets gute Stimmung und die vielen Kaffeepausen. Insbesondere möchte ich dabei erwähnen Dr. Monika Quentin, Dr. Eddy Rugerimegabo, Dr. Johannes Aprojanz und Markus Gruschwitz.

Außerdem danke ich Annas bin Ali und Leo Rizzi für die tolle Zusammenarbeit und die vielen Telefonate.

Danke, an alle die sich über die Jahre mit viel Geduld alles über meine Arbeit angehört haben, das ich erzählen wollte.

Ein großer Dank gilt auch meiner Schwester, Dr. Anne Slawig, die nicht nur immer da war, sondern auch das beste Vorbild war, dass ich mir hätte wünschen können.

Vielen Dank auch an meine Eltern, für ihre unermüdliche Unterstützung, den unerschütterlichen Glauben daran, dass ich alles werden kann was ich nur will und dafür, dass sie immer interessiert an meiner Arbeit waren – selbst wenn sie sie nicht immer verstanden haben. Und für die Rutsche mit der alles angefangen hat

Zuletzt möchte ich mich bei Björn bedanken, dafür dass er mich die gesamte Zeit vollkommen unterstützt hat, für seine Geduld und für seinen unglaublichen Optimismus.

Vielen Dank!